

**In-situ MnO₂ Electrodeposition and its Negative Impact
to Rechargeable Zinc Manganese Dioxide Batteries**

by

Rui Lin Liang

A thesis

presented to the University Of Waterloo

in fulfilment of the

thesis requirements for the degree of

Master of Applied Science

in

Chemical Engineering (Nanotechnology)

Waterloo, Ontario, Canada 2018

© Rui Lin Liang 2018

Author's Declaration

I hereby declare that I am the sole author of this thesis. This is a true copy of the thesis, including any required final revisions, as accepted by my examiners.

I understand that my thesis may be made electronically available to the public.

Abstract

Achieving high rechargeability with the economically feasible and environmentally friendly Zn-MnO₂ batteries has been the goal of many scientists in the past half century. Recently, the stability of the system saw a significant improvement through adaptation of mildly acidic electrolyte with Mn²⁺ additives that prevent dissolution of the active cathode materials, MnO₂. With the new design strategy, breakthroughs were made with the battery life span, as the lab scale batteries operated with minimal degradation for over a thousand cycles of charge and discharge at high C-rate (>5C) cycling. However, low C-rate operation of these batteries is still limited to 100 cycles, but has not been a focal point of the research efforts. Furthermore, the electrochemical reactions within the battery system are still under debate and many questions remain to be answered.

An interesting phenomenon investigated in this thesis about the mildly acidic Zn-MnO₂ battery systems is their tendency to experience capacity growth caused by formation of new active material through Mn²⁺ electrodeposition. The deposition reaction is thermodynamic favored within the battery operating voltage window and is considered by some as beneficial for battery performance. This general belief is challenged by the investigations and experimentations in this thesis, as results indicate the MnO₂ polymorph generated are not ideal for long term cycling and would eventually lead to formation of electrochemically inactive Mn species. Uncontrolled, continuous occurrence of the reaction would also lead to Mn²⁺ ion depletion and uplifting of the protection they provide. The electrodeposition is therefore relabelled as a gateway that allows undesired reaction to occur within Zn-MnO₂ batteries; a long term crystal transition mechanism of the active cathode material was also formulated based on the post cycling characterizations of the electrodes.

With the newly developed recognition of the battery stability issues, a design strategy focused on suppressing MnO₂ electrodeposition through manipulating the reaction kinetic is proposed. The effectiveness of the strategy was showcased by cathode electrodes incorporated with expanded graphite, a hydrophobic substrate material discovered to be non-ideal for MnO₂ electrodeposition. The resulting polymer-free

electrode exhibit much improved low C-rate cycling stability of over 300 cycles with minimal capacity decay and rate performances that are comparable to state-of-the-art Zn-MnO₂ battery cathode electrodes. These significant electrochemical performance improvements validate the effectiveness of the strategy, and it is intended to be a key concept that would serve as an important stepping stone for further optimization of the Zn-MnO₂ battery system.

Acknowledgement

I would like to take the opportunity to send my most sincere appreciation to Professor Zhongwei Chen for providing me with the chances and resources to conduct my experiments. I would also like to sincerely thank Dr. Jing Fu, Dr. Gregory Lui, Post-Doctoral Fellow Dr. Yuanli Ding and Dr. Gaopeng Jiang for their generous guidance on my research project and safety management work. Furthermore, I would like to send my gratitude and best wishes to my groupmates Maiwen Zhang, Yaping Deng, Dan Luo, Dr. Wen Lei, Dr. Yi Jiang, Dr. Jie Ying, Dr. Yang Wang, Justin Raimbault, Abel Sy, Jing Zhang and Pan Xu. Last but not least, I would like to thank my parents, family members and friends for their continuous support to my pursue in the field of scientific and engineering research.

Table of Content

Author's Declaration.....	ii
Abstract.....	iii
Acknowledgement	v
Table of Content	vi
List of Figure.....	ix
List of Tables	xii
List of Abbreviations	xiii
1 Introduction.....	1
1.1 Batteries and Renewable Energy.....	1
1.2 Rechargeable Batteries and Zinc Batteries.....	2
1.3 Manganese Dioxide Cathode	5
1.4 Alkaline Zn-MnO ₂ Batteries	8
1.4.1 Primary Alkaline Zn-MnO ₂ Batteries	8
1.4.2 Rechargeable Alkaline Zn-MnO ₂ Batteries	11
1.5 Rechargeable Mildly Acidic Zn-MnO ₂ Batteries.....	13
1.6 Research Objective.....	16
1.7 Organization of Thesis	16
2 Chemicals and Characterization Techniques	18
2.1 Materials.....	18
2.2 Physical Characterization.....	19
2.2.1 Scanning Electron Microscopy	19
2.2.2 Transmission Electron Microscopy	20
2.2.3 Energy-Dispersive X-ray Spectroscopy.....	20
2.2.4 X-Ray Diffraction Analysis	21

2.2.5	X-Ray Photoelectron Spectroscopy	22
2.2.6	Raman Spectroscopy.....	22
2.2.7	Inductively Coupled Plasma Atomic Emission Spectroscopy	23
2.3	Electrochemical Characterization	24
2.3.1	Galvanostatic Discharge/Cycling.....	24
2.3.2	Cyclic Voltammetry.....	25
3	Investigation of Manganese Dioxide Electrodeposition in Rechargeable Mildly Acidic Zn-MnO ₂ Batteries	26
3.1	Introduction	26
3.2	Experimental Methods	27
3.2.1	Synthesis of α -Manganese Dioxide	27
3.2.2	Preparation of Manganese Dioxide Electrode	27
3.2.3	Preparation of Polymer-free/Self-standing Manganese Dioxide electrode	28
3.3	Results and Discussions	28
3.3.1	Characterization and Electrochemical Analysis of α -MnO ₂	28
3.3.2	Investigation of In-situ Manganese Oxide Electrodeposition.....	35
3.3.3	Transformation Mechanism of Pristine and Electrodeposited MnO ₂	42
4	Suppressing Manganese Dioxide Deposition with Expanded Graphite for High Performance Zn-MnO ₂ Batteries	52
4.1	Introduction	52
4.2	Experiment Procedures	53
4.2.1	Preparation of Expanded Graphite.....	53
4.2.2	Preparation of Polymer-free Manganese Dioxide/Expanded Graphite/Carbon Nanotube Electrode	54
4.3	Results and Discussions	54

4.3.1	Adaptation of Expanded Graphite and Optimization of Cathode Electrode for High Performance Zn-MnO ₂ Batteries.....	54
5	Conclusions and Suggestions.....	63
6	Reference	64
7	Appendix.....	70
7.1	Appendix A: Calculation of Manganese Ion Oxidation Potential.....	70

List of Figure

Figure 1.1 World energy contribution of different energy sources in 2005, 2010 and 2015	1
Figure 1.2 Market prices of a) cobalt, b) lithium carbonate and c) lithium hydroxide.....	3
Figure 1.3 Ball and stick representation of MnO ₂ octahedron unit cell.....	5
Figure 1.4 Diagram representations of different MnO ₂ crystal structures.....	6
Figure 1.5 Compositional diagrams of a) cylindrical and b) button alkaline Zn-MnO ₂ batteries	10
Figure 1.6 The Pourbaix diagram of a) manganese and b) zinc at 25 °C.....	13
Figure 2.1 Sample illustration of the general coin cell assembly	24
Figure 3.1 a) XRD analysis b) Raman spectrum, c) SEM image and d) TEM image of α-MnO ₂ nanotubes.....	29
Figure 3.2 a) Galvanostatic charge and discharge curves in the first two cycles and b) specific capacity profile at 1C of the Zn/α-MnO ₂ batteries with and without 0.1 M MnSO ₄	30
Figure 3.3 a) SEM images of standard α-MnO ₂ electrode before and b) after cycling. ...	31
Figure 3.4 a) SEM cross section image of the cycled α-MnO ₂ electrode and b, c) corresponding SEM and EDX analysis of an area in the cross section of the cycled α-MnO ₂ electrode.	31
Figure 3.5 a) Specific capacity profiles of the RMAZM batteries with different cycling protocols, b) different amount of electrolyte and c) different MnSO ₄ concentration. d) Galvanostatic discharge curves of RMAZM batteries using 0.5M MnSO ₄ additives at different cycles.....	32
Figure 3.6 a) Diagram illustration of the graphite/Zn wet cell b) capacity and Mn concentration vs. cycle number graph of the graphite/Zn wet cell	34
Figure 3.7 a) Photo of the CNT and b) MC thin film separator-assembly. c) d) Photos of the self-standing MC electrode.....	35
Figure 3.8 a) Discharge capacity profiles and b) Galvanostatic charge/discharge curves at 1 st , 2 nd and 50 th cycles of MC and CNT electrodes.....	36

Figure 3.9 a) SEM image of the surface of the MC electrode before and b) after cycling, c) SEM image of the surface of the MC electrode before and d) after cycling, e) TEM images of MnO _x nanosheets from MC and f) CNT electrodes.	37
Figure 3.10 a) XRD spectra of CNT electrode and b) MC electrode at their initial, peak capacity and degraded states.	38
Figure 3.11 a) XPS scan survey of the cycled CNT electrode b) Mn 2p c) Mn 3s and d) O1s spectra of the cycled CNT and pristine MC electrode.	40
Figure 3.12 a) SEM image and b) XRD spectrum of MnO ₂ electrodeposited onto the CNT electrode surface by 48 hrs of 1.8V constant voltage hold	42
Figure 3.13 a) Galvanostatic charge/discharge voltage vs time curves and b, c) corresponding XRD patterns of the CNT electrode with electrodeposited ε-MnO ₂ at different state of charge and discharge.	43
Figure 3.14 a) Galvanostatic charge/discharge voltage vs time curves and b, c) corresponding XRD patterns of the α-MnO ₂ MC electrode at different state of charge and discharge.	45
Figure 3.15 The HRTEM images of a) α-MnO ₂ nanorod, b) electrodeposited MnO ₂ nanosheets and c) intersection of a nanorod and nearby nanosheets. The inset images are the FFT and Inverse FFT of the selected areas.	48
Figure 3.16 a) 1 st , 2 nd and 3 rd Galnostatic discharge curves of RMAZM batteries using 2M MnSO ₄ or 2M ZnSO ₄ + 0.1M MnSO ₄ electrolyte. b) XRD diffraction patterns of MC electrode in RMAZM batteries discharged to 1.0V with 2M MnSO ₄	49
Figure 3.17 Schematic illustration of the long term crystal transformation of α-MnO ₂ within RMAZM batteries that adapted Mn ion additives.	50
Figure 4.1 SEM images of the a) as-prepared and b) sonicated thermal shock expanded graphite	55
Figure 4.2 a) Standard Galvanostatic charge and discharge curves and b) specific capacity profile of ME electrode. c) Discharge capacity profiles of pure CNT and EG electrodes	57
Figure 4.3 a) Surface and b) cross section SEM images of the MEC electrode	57
Figure 4.4 a) CV scans, b) 1C Galvanostatic cycling performance, c & d) rate performance, and e) 5C Galvanostatic cycling performance of RMAZM batteries prepared with MEC electrode.	59

Figure 4.5 a, b) SEM surface image of the MEC electrode after Galvanostatic cycling, c, d) SEM surface image of the MEC electrode after 48hrs of 1.8V constant voltage hold. 61
Figure 4.6 a) XRD spectra of the MEC electrodes and b) HRTEM image of the MEC electrode after 500 cycles of Galvanostatic charge and discharge..... 61

List of Tables

Table 1 Performance of zinc batteries in recent publications	4
Table 2 Low current cycling of RMAZM batteries in recent publications.....	15
Table 3 List of Chemicals	18

List of Abbreviations

Abbreviations	Intended Word/Phrases
CNT	Carbon Nanotube
CV	Cyclic Voltammetry
DOD	Depth of Discharge
DDI	Distilled Deionized
EDX	Energy Dispersive X-ray Spectroscopy
EG	Expanded Graphite
EIS	Electrochemical Impedance Spectroscopy
EMD	Electrolytic Manganese Dioxide
EtOH	Ethanol
ICP-OES	Inductively Coupled Plasma Optical Emission Spectrometry
H ₂ O	Water
KMnO ₄	Potassium Permanganate
KOH	Potassium Hydroxide
MC	MnO ₂ + CNT
MEC	MnO ₂ + EG + CNT
MnO ₂	Manganese Dioxide
MnSO ₄	Manganese Sulfate
NiMH	Nickel Metal Hydride
OCV	Open Circuit Voltage
RAM	Rechargeable Alkaline Manganese
SEM	Scanning Electron Microscopy
TEM	Transmission Electron Microscopy
XPS	X-Ray Photoelectron Spectroscopy
XRD	X-Ray Diffraction
Zn	Zinc
ZnSO ₄	Zinc Sulfate

1 Introduction

1.1 Batteries and Renewable Energy

Batteries are a type of electrochemical energy storage system that convert chemical energy to electrical energy.¹ They are portable, reliable and convenient to use; they are also essential to many electronic devices that many rely upon in their daily life. In recent years, the demands for batteries with higher energy density and longer cycle life have been rising.¹ Some of these pressures are from the increasing performance requirement of newly developed technologies, and others are from the urgency of accelerating the adaptation of renewable energies into the current energy system to combat climate change and reduce fossil fuel reliance.

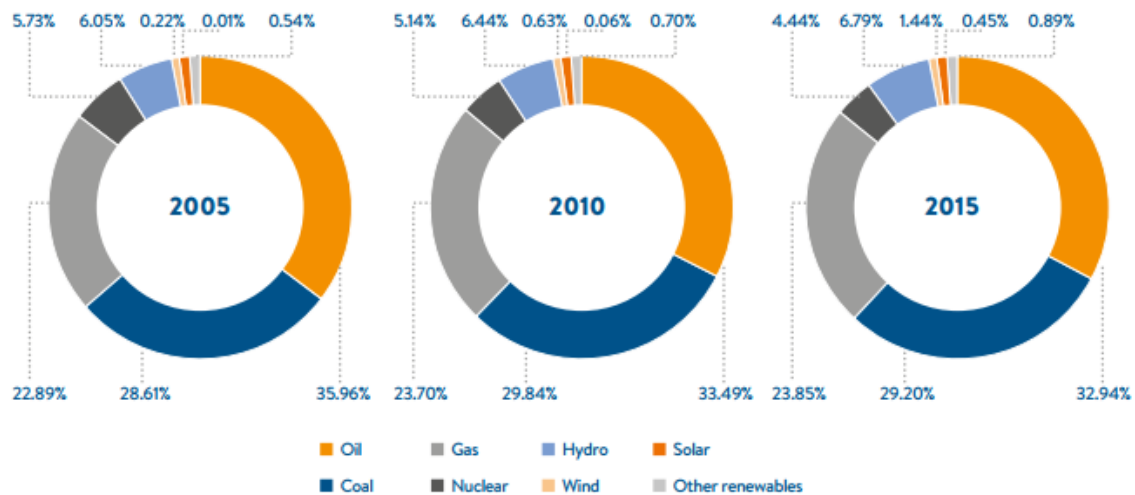


Figure 1.1 World energy contribution of different energy sources in 2005, 2010 and 2015. Reproduced with permission of World Energy Council².

As reported by the Word Energy Council, in 2015, all renewable energies sources (hydro, wind, solar and other) contribute only 9.57% of total world energy consumption (Figure 1.1).² While solar and wind energy sources have achieved significant output growths, their overall production is still limited and their low cost effectiveness and environmental impact have also been criticized.³⁻⁵ Moreover, fundamental infrastructures including grid energy storage and electric transmission network are not fully developed and constructed, which further limits the effectiveness of these systems.^{6,7}

Rechargeable batteries play an important role in continuing the advancement and electric grid integration of renewable energies. A well-known disadvantage of renewable energies is their output fluctuation, which brings difficulties in balancing the supply and demand of electricity, and often leads to wasted energy.⁴ Their tendency of generating large portion of their overall production during low demand hours also adds complexity to the process. Currently, these issues are addressed by large, centralized energy storage systems such as hydroelectric pump and compressed air storage.⁸ However, these systems would struggle to support the infiltration of renewable energy sectors, and the flexibility and compactness offered by rechargeable batteries will become more and more valuable.⁸ Hence, the development of long lasting, cheap, safe, and environmentally benign rechargeable batteries are necessary for maintaining the prosperity of the human society.

1.2 Rechargeable Batteries and Zinc Batteries

Lithium-ion batteries are one of if not the most successful rechargeable batteries in the twentieth century. Their high energy density and decent life cycles are ideal for energy storage system.¹ However, lithium-ion batteries are prone to thermal runaway and have caused numerous fire/explosion incidents.⁹ Accidental releases of volatile, toxic or corrosive chemicals within the batteries, such as 1,2-dimethoxyethane (DME), diethyl carbonate (DEC), lithium hexafluorophosphate (LiPF₆) salt, cobalt and nickel containing oxides are also possible health hazards that can cause great harm.^{10,11}

Apart from their safety issues, another major concerns about lithium ion batteries are the growing prices of their core materials.^{12,13} Between the years of 2015 to 2018, the price of cobalt, an essential component of lithium ion batteries cathode, has raised by more than 200 % (**Figure 1.2 a**).¹⁴ Similarly, the prices of lithium carbonate and lithium hydroxide have seen increase of over 100 % from 2015 to 2018 (**Figure 1.2 b and c**).¹⁵ Future availability of these raw materials has also been studied by various research and forecast groups. While many of which have predicted that current cobalt and lithium reserves can at least satisfy the increasing battery demands until 2050 with adequate recycling, there are negative speculations on the quality of the unexploited resources and the stability of the supply.^{13,16,17} Driven by the limitations and uncertainties surrounding

lithium based batteries, there has been an increasing interest in exploring possible alternate battery systems that is based on other chemistries.

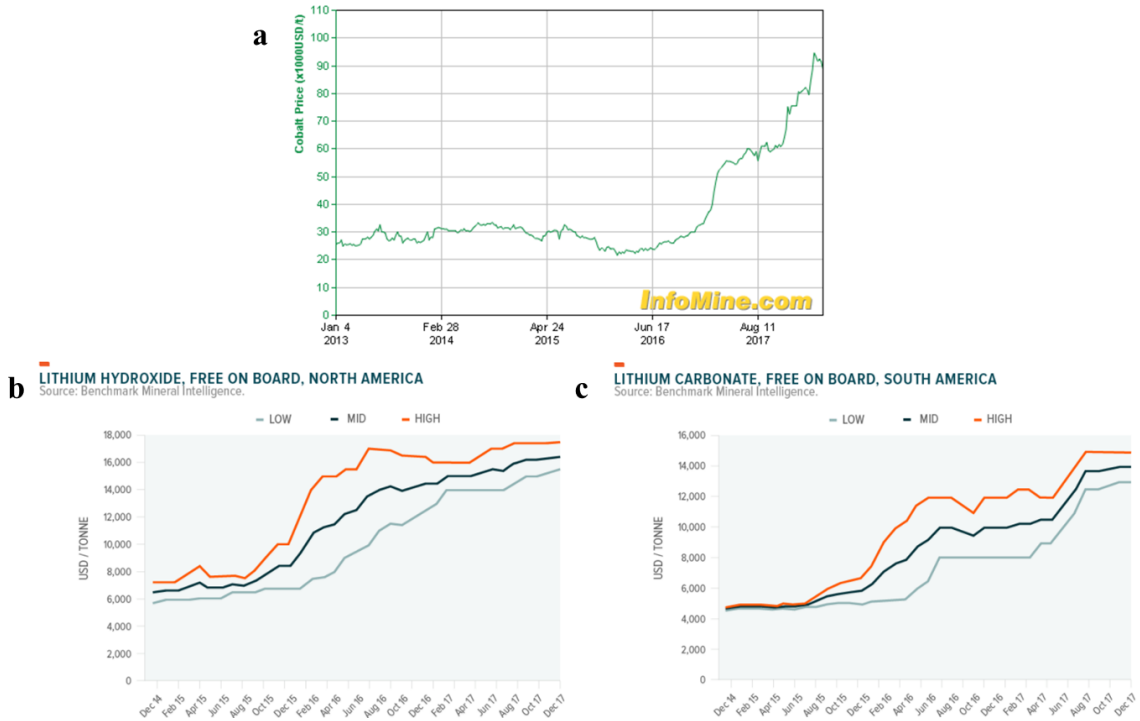


Figure 1.2 Market prices of a) cobalt, b) lithium carbonate and c) lithium hydroxide. Figure a was obtained from Infomine,¹⁴ and diagram b and c were obtained from Global X Funds.¹⁵

Numerous non-lithium based batteries are actively being investigated and some have already demonstrated promising properties that would be of great use in the future. For example, sodium ion batteries are considered by many as a promising alternative of lithium ion batteries that have slightly weaker performance but much better material availability;¹⁸ metal air batteries such as zinc air batteries that have higher energy density ceilings and lower cost;^{19,20} and aqueous zinc batteries which recently regained considerable amount of research attentions due to breakthroughs that significantly improve their rechargeability.^{21,22}

Historically, zinc is one of the most common battery anode materials. Over the years, it has been used in the Leclanché cell, zinc-carbon batteries, alkaline batteries, zinc mercury oxide batteries, zinc silver batteries, zinc air batteries and rechargeable zinc nickel batteries.²³ While some of these batteries are manufacture-discontinued due to cost or health issues, others such as alkaline, zinc air and zinc nickel batteries still own

significant shares of the current battery market.²³ As an anode material, zinc has a relatively low standard potential of -0.76 V and a medium-high theoretical specific capacity of 818 mAh g⁻¹. It offers advantages such as low toxicity, high abundance, low cost, compatibility with aqueous system and ease of handling.²⁴ Worldwide, the estimated land based resources and reserves of zinc are 1.9 billion tonnes and 220 million tonnes,²⁵ respectively, which are at least 10 times more than that of lithium.¹³ Global annual productions of refined zinc are around 13 million tonnes, with near 25% contributed by the recycling industries.²⁵ The zinc recycling process is well-developed and there are still consistent effort to further improve the process by reducing their energy consumption and environmental impact.²⁶⁻²⁸ Given the maturity of the industrial processes and the natural abundance of the metal, zinc would make a sustainable and affordable battery core material that can meet high demand with ease.

Table 1 Performance of zinc batteries in recent publications

Types of Batteries	Voltage	Energy Density (Active Materials)	Cyclability
3DZn–NiO ₂ ^[22]	1.4 – 1.9 V	135.0 Whkg ⁻¹	80 % (> 80 cycles)
Zn–Zn _{0.25} V ₂ O ₅ •nH ₂ O ^[29]	0.5 – 1.4 V	175.0 Whkg ⁻¹	80 % (1000 cycles)
Zn–Quinone ^[30]	0.4 – 1.0 V	220.0 Whkg ⁻¹	87 % (1000 cycles)
Zn–α-MnO ₂ ^[21]	1.0 – 1.8 V	~170 Whkg ⁻¹	92 % (5000 cycles)
Zn–β-MnO ₂ ^[31]	1.0 – 1.8 V	158.5 Whkg ⁻¹	94 % (2000 cycles)

Traditionally, the oxidation and reduction reaction of zinc in batteries are not known to have high reversibility and often suffer from issue like dendrite formation. However, recent studies have demonstrated that with adequate electrode design (3D porous zinc electrode)²² and proper electrolyte selection (mildly acidic/neutral electrolyte^{21,29,31}),^{21,29,31} the impact of these issue can be reduced. There are also a large number of studies about cathode materials for Zn batteries, which mainly focuses on improving the reversibility, rate capability and energy density. Some families of materials which have been considered and investigated include transition metal oxide,³²⁻³⁵ sulfide,^{34,36,37} and hexacyanoferrate.³⁸⁻⁴⁰ Among them, the best performing ones are the layered structured V₂O₅ •nH₂O demonstrated by Kundu *et al.*,²⁹ the organic and sustainable quinone-based cathodes showcased by Zhao *et al.*,³⁰ and manganese dioxide

(MnO₂) of different crystal structures(**Table 1**).^{21,31} In this project, the focus will be on the latter of the three; the history, properties, reaction mechanism and recent progress of the corresponding Zn-MnO₂ batteries will be discussed in the following section.

1.3 Manganese Dioxide Cathode

Manganese is a relatively abundant, non-toxic and environmentally friendly transition metal. It is commonly found in ores as oxide compounds with other elements such as iron, sodium, and barium.⁴¹ The current global reserve of manganese ore is around 690 million tonnes,⁴² and their recent price point have been fluctuating between 1500-2500 \$US/tonne,⁴³ which are less than one twentieth to the price of cobalt. Manganese exhibits a rich variety of oxidation states and participates in various electrochemical reactions, of which, the oxidation and reduction of oxides with manganese at the state of 2+, 3+ and 4+ are core reactions to many batteries. As an example, manganese containing oxides such as LiMn₂O₄, LiNi_{0.33}Mn_{0.33}Co_{0.33}O₂ (NMC), and MnO₂ are all well-known cathode materials which play significant roles in the current battery industry.

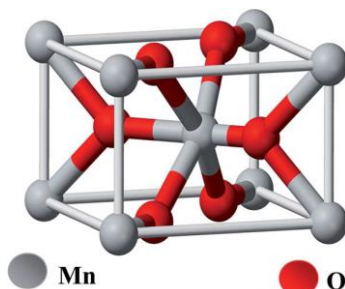


Figure 1.3 Ball and stick representation of MnO₂ octahedron unit cell. Diagram adapted from publication of Biswal *et al.*⁴¹.

As a cathode material, MnO₂ has a theoretical specific capacity (2 electrons) of 616 mAh g⁻¹ and a standard potential around 1.0 V to 1.5 V depending on the specific reaction. Their crystal structures are built on the basis of [MnO₆] octahedron unit cells (**Figure 1.3**) that connect to each other by sharing common corners or edges. Some common MnO₂ crystals include the 1D tunnel structured Hollandite/Cryptomelane (α -MnO₂), Pyrolusite (β -MnO₂), Ramsdellite (R-MnO₂), Nsutite (γ -MnO₂) and Akhtenskite (ϵ -MnO₂) (**Figure 1.4**); the layer structured Birnessite (δ -MnO₂), and the spinel structured λ -MnO₂.⁴⁴

β -MnO₂ is the simplest and thermodynamically the most stable form of MnO₂. The [MnO₆] subunits in this crystal phase connect on their corner to form tunnels with channel size of [1×1] along the c-axis. The R-MnO₂ adapts a very similar crystal arrangement, but with tunnels that have [1×2] channel instead.^{44,45} The intergrowth of these two phases during crystallization are common, which often leads to formation of irregular products such as γ -MnO₂ and ϵ -MnO₂ that have tunnels of both sizes and demonstrate different type and amount of defects within the crystal structure.⁴⁶⁻⁴⁸ Both of the [1×1] and [1×2] tunnels are narrow and have limited capability of proton transportation.⁴⁹ As a result, instead of pure crystalline β -MnO₂ or R-MnO₂, γ -MnO₂ is often the cathode active material of choice in commercial Alkaline Zn-MnO₂ batteries.⁵⁰ It has been confirmed by experimental results that the structural defects and grain boundary found in γ -MnO₂ are the key features that lead to its superior electrochemical performance.⁴⁹⁻⁵²

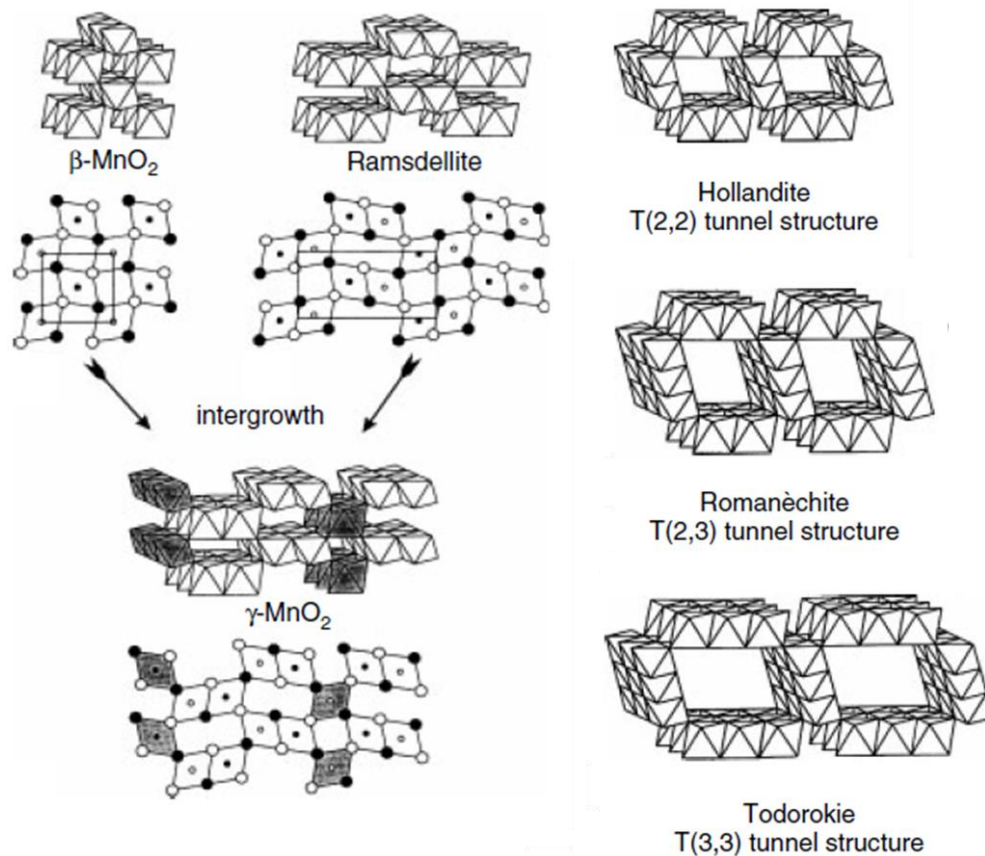


Figure 1.4 Diagram representations of different MnO₂ crystal structures. Diagram adapted from the Handbook of Battery Materials.⁴⁴

In contrast to the family of β - MnO_2 and R- MnO_2 , α -phase MnO_2 contains both $[1 \times 1]$ and $[2 \times 2]$ tunnels, with the latter being large enough to incorporate large cations such as barium, silver and potassium.⁵¹ These cations in the $[2 \times 2]$ tunnels have mix effect on the properties and electrochemical performance of the material. In one end, they contribute to stabilizing the large tunnels and are beneficial for charge transfer,^{53,54} in the other, their large sizes hinder transportation of the intercalation ions.⁵¹ Due to the capability of the $[2 \times 2]$ tunnel to host insertion and desertion of various cations, α - MnO_2 had been investigated as active cathode material in lithium, sodium, magnesium and zinc batteries.^{32,55-61} Furthermore, it is also a candidate material for applications in supercapacitor and catalysis.⁶²⁻⁶⁶ MnO_2 with larger tunnel sizes such as Romanèchite ($[2 \times 3]$) and Todorokite ($[3 \times 3]$) have also been reported(**Figure 1.4**).⁴⁴ These types of MnO_2 generally have better structural stability, but lacks capacity and energy density due to their less portion of active components.⁶⁷

Layer structured MnO_2 , whose crystal structure consist of stacking layers of edge-sharing MnO_6 subunit, has also been studied extensively for possible electrochemical applications. Similar to α - MnO_2 , the void space between the stacking layers can accommodate different types of cation, which in return serves to stabilize the crystal structures. δ - MnO_2 is a subgroup of the layer structured MnO_2 family which contains varying amount of H_2O molecule and foreign cations in the interlayer spacing with H_2O being the predominate species.⁴⁴ The structural framework of δ - MnO_2 is relatively flexible and the H_2O molecules can easily move around to accommodate different types of intercalation ions.⁶⁸ Consequently, X-Ray Diffraction (XRD) analysis of these materials has proven to be very difficult as results vary significantly due to the distribution of the interlayer species.⁴⁴ Despite so, their flexibility and large interlayer distance have attracted attention for applications as intercalation cathode materials.⁶⁹⁻⁷¹

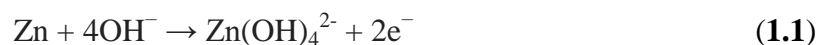
Manganese ores found naturally often need to be processed to achieve battery grade purity and desired crystal phases. Depending on the method of processing, MnO_2 is divided into two categories, the electrolytic manganese dioxide (EMD) and the chemical manganese dioxide (CMD).²³ EMD is generally prepared by first dissolving manganese ores in sulphuric acid solution, followed by multiple steps of purification processes ($\text{Ca}(\text{OH})_2$ and NaS treatment) to remove undesired heavy metal impurities.⁴¹ Then, the

battery grade EMD would be collected from the manganese solution through electroplating.²³ As-prepared EMD generally have crystal structure that resembles to β - MnO_2 , ε - MnO_2 or γ - MnO_2 , and very often is a polymorph of the three phases.⁴¹ As for CMD, they are MnO_2 prepared by methods such as thermal decomposition, direct oxidation and reduction of high-valence manganese salts. They can be prepared into different crystal structure easily and precisely with different reaction methods and conditions.⁷²⁻⁷⁴ Historically, CMD is considered to be less pure and have lower volumetric density, thus are not use in the commercial Alkaline Zn- MnO_2 batteries, but with new inspiration of its application potential and improvement of the synthesis procedures, it is becoming more appreciated by the research and industrial community.⁴⁴ More details regarding CMD will be provided in the later section as it will be a main focus of this thesis project.

1.4 Alkaline Zn- MnO_2 Batteries

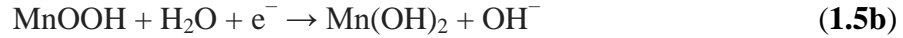
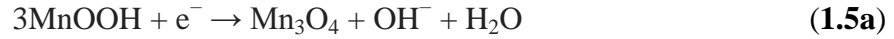
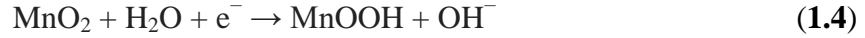
1.4.1 Primary Alkaline Zn- MnO_2 Batteries

Primary Zn- MnO_2 alkaline batteries are one of the iconic primary batteries developed in the twentieth century. They were first discovered in 1960 by Lewis Urry who modified the previously existing zinc-carbon dry cell batteries by changing the ammonium chloride/zinc chloride gel electrolyte to one that is based on potassium hydroxide (KOH).⁷⁵ In comparison to zinc-carbon batteries, the modification significantly improved their energy density, service performances, shelf life and stability.²³ These properties along with the environmental factors were further optimized in years following their commercialization by company such as Duracell and Energizer, which consolidated their status as the primary battery market leader. It was estimated that, in the year of 2003, alkaline Zn- MnO_2 batteries account for near 80% of the total primary battery sales in the United State.¹ This dominance may have been weakened in recent years as availability of higher performing batteries such as primary lithium ion batteries are growing, but the affordable, safe and reliable alkaline Zn- MnO_2 batteries are still competitive for low drain applications.





The electrochemistry of primary Zn–MnO₂ alkaline batteries is complex and has been studied for years. The batteries have MnO₂ as cathode, Zn as anode and KOH in the form of gel electrolyte. During discharge, the three consecutive steps of the anodic reactions are described in **Equations (1.1), (1.2) and (1.3)**.^{23,76} In the very beginning, zinc metal would oxidize into zincate ion (Zn(OH)₄²⁻) and dissolve into the water inside the system, where it will exist in the form of potassium zincate (K₂Zn(OH)₄).⁷⁶ As the limited water becomes saturated with zinc ions, the water-starved environment changes the reaction. In this stage, the zinc would oxidize into zinc hydroxide (Zn(OH)₂) instead, which would further dehydrate to form zinc oxide (ZnO) that precipitate as white solid onto the zinc electrode.²³



On the cathode side, the MnO₂ reduction process in alkaline Zn-MnO₂ batteries are often represented by the reactions described in **Equations (1.4), (1.5a) and (1.5b)**.²³ In this cathodic reduction reaction, the MnO₂ will first reduce to MnOOH, then to Mn₃O₄ or Mn(OH)₂ depending on the depth of discharge (DOD) or the cut-off voltage. If only 1.33 electrons per MnO₂ were drawn out, the end product would be Mn₃O₄,²³ and if all capacity (2 electrons) are completely drawn out from the MnO₂, the final product would be Mn(OH)₂.¹ Combining the anodic and cathodic reactions, the overall reaction in alkaline Zn-MnO₂ batteries under intermediate or complete drain is then either **Equations (1.6a) or (1.6b)**.



The above discussions are a very simplified description of the events which occur within alkaline Zn-MnO₂ batteries. The actual reaction mechanism involves various

manganese oxide polymorphs and their corresponding stages of transition; these reduction reactions can be homogeneous or heterogeneous, which are reflected by a decreasing or a relatively constant potential, respectively.⁷⁷ Formation and participation of manganese oxide/hydroxide with different oxidation states such as Mn_4O_7 , $MnOOH$, Mn_2O_3 , Mn_3O_4 , $Mn(OH)_2$, MnO have all been reported in previous publications, but their result do not fully agree.⁷⁷⁻⁸⁰ The tendency of the mechanism being influenced by factors such as crystal phases, synthesis condition and purity of MnO_2 , KOH concentration, and rate of discharge also adds onto the complexity and unpredictability of the system.^{77,78} As such, the MnO_2 reduction mechanisms remain to be a topic that is still controversial.

The alkaline Zn- MnO_2 batteries are available in two design configurations, the cylindrical batteries and the button cells.²³ The general compositional diagrams of them are provided in **Figure 1.5a** and **1.5b**. In both design, they are assemble with an inert stainless steel shell, MnO_2 gel slurries, nonwoven separator (vinyl polymers, regenerated cellulose, etc.), zinc gel slurries, metal anode current collector and small accessories that prevent leakage, corrosion and short circuiting.²³ The components are simply filled into the shell one by one, and the assembly is complete in an atmospheric environment. The simplicity of the assembling processes is a big economic advantage of alkaline Zn- MnO_2 batteries that allows them to remain competitive in the current battery market.

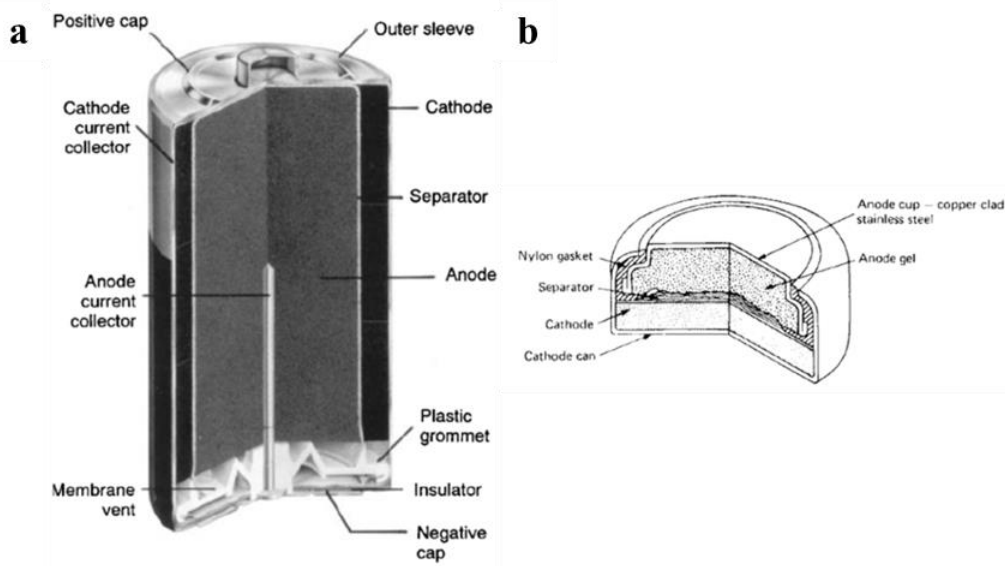


Figure 1.5 Compositional diagrams of a) cylindrical and b) button alkaline Zn- MnO_2 batteries. Diagram A obtained from Duracell Technical Bulletin⁸¹, and diagram B obtained from Eveready Battery Engineering Data⁸².

The slurries are of great importance to the battery performance, thus, its composition is worth to be further discussed. First, the MnO₂ gel slurries are a mixture of MnO₂, graphite, KOH electrolyte and small amount of binding agent. The MnO₂ are often EMD due to their high purities and compatibility. The graphite is added to compensate for the low electric conductivity (10^{-5} - 10^{-7} S cm⁻¹) of the manganese oxides.⁸³ As for the anode slurries, they are prepared by mixing zinc powder, KOH gel electrolyte and small amount of inhibitor. Industrially, the purity of the zinc powder was ensured by refinement through thermal distillation or electroplating. The addition of the inhibitor is to prevent the highly active zinc metal from reducing water to hydrogen gas, which would cause battery leakage and exhaust the limited amount of water in the dry cell; it was initially resolved with the addition of mercury as the inhibitor,^{23,84} but it is no longer the case because the usage of mercury in batteries was officially prohibited by the U.S. government in 1996 due to its toxicity and possible threats to environmental.⁸⁵ Since then the inhabitation task is achieved by alloying zinc with metal such as indium or lead,⁸⁶ or by addition of inhibitors like anionic surfactant and quaternary ammonium salt.⁸⁷

1.4.2 Rechargeable Alkaline Zn-MnO₂ Batteries

With the success of Zn-MnO₂ batteries in the primary battery market, attempts were made to develop and commercialize rechargeable alkaline Zn-MnO₂ batteries. The first attempt was made by Union Carbide Corp. (Eveready) and Mallory Corp. in 1977, but the product was withdrawn shortly after due to leakage issue.⁴⁴ The second generation of the rechargeable alkaline manganese (RAM) batteries returned a decade later when Battery Technology Inc. modified and improved the design of the batteries.⁸⁸ Following which, the RAM batteries were promoted and commercialized in the United State, Germany, South Korea, etc.^{44,89} In comparison to other rechargeable batteries in the 1990s such as nickel cadmium (NiCd) and nickel metal hydride(NiMH) batteries, RAM batteries have higher operating voltage, lower self-discharge, lower initial cost and are more environmental friendly.²³ However, the RAM batteries suffer greatly from low rechargeability and often lose near half of its initial capacity after only 20 cycles of deep discharge (1 electron capacity).²³ This disadvantage has limited their widespread

applications and the products have been slowly fading out of the market as the better performing lithium-ion and NiMH batteries became cheaper and more accessible.

The rechargeability of RAM batteries is very dependent on the depth of discharge (DOD). It has been reported that when cycled with a shallow DOD of 10%, the RAM batteries can maintain more than 80% of its capacity after 3000 cycles of operation.⁹⁰ In this specific circumstance, the MnO_2 are only partially reduced to MnOOH , and the reversibility of this process is high. However such cycling protocols would greatly reduce the practical energy density of the batteries and render its usefulness in actual applications. In the case when the battery is fully discharged, various issues will arise in both ends of the batteries.

In the cathode side, destruction of crystal structure, active material dissolution and most importantly, the formation of electrochemically inactive species such as Mn_3O_4 and ZnMn_2O_4 are the leading causes of capacity lost in RAM batteries.⁹⁰⁻⁹² Previous studies have identified that $\alpha\text{-MnOOH}$, a reaction intermediate in the recharging process, is a necessary precursor for the inactive MnO_x species.^{93,94} Therefore, a common theme in resolving the issue is to promote specific oxidation reaction paths by modifying the crystal structure of MnO_2 with foreign cations. In one example, Kannan *et al.* demonstrated that the addition of 10 wt% Bi_2O_3 to the MnO_2 can lead to formation of Bi-doped birnessite type MnO_2 instead of the inactive products and drastically improved the cyclability of the cathode material.⁹² The effects of barium, titanium, or nickel doping, as well as electrolyte modification ($\text{LiOH} + \text{KOH}$) have also been investigated.⁹⁴⁻⁹⁷ More recently, Yadav *et al.* demonstrated a copper and bismuth co-doped birnessite type MnO_2 cathode which maintained over 80% of the MnO_2 two electron capacity (617 mAh g^{-1}) after 1,000 cycles of 1C cycling versus a standard reference.⁹⁸ Though, when paired with a zinc anode, the rechargeability of the system would drastically reduce to one that loses 25% of its energy density in 100 cycles.

In the anode side, formation of ZnO , zinc dendrite and undesired hydrogen evolution are the predominant reasons for failures or low rechargeability. Common strategies of suppressing zinc dendrite formation include adding small amount of organic surfactants such as sodium dodecyl sulfate (SDS), polyethylene glycol (PEG) or thiourea

to the electrolyte.⁹⁹ Preparation of Zn electrode with 3D porous structure to direct the location of zinc deposition is also proven to be an extremely effective strategy.²² Lastly, recent studies have demonstrated that hydrogen evolution by zinc in alkaline condition can be suppressed with application of metal oxide or polymer composite additive.^{100,101}

1.5 Rechargeable Mildly Acidic Zn-MnO₂ Batteries

Another route of avoiding the issues found in traditional RAM batteries is by changing the system into one that is mildly acid or neutral. This idea was inspired by studies in the late 20th century, when researchers began to explore possibility of adapting other electrolytes into Zn-MnO₂ batteries and discovered that batteries prepared with mildly acidic zinc sulphate (ZnSO₄) electrolyte exhibit some degree of rechargeability.¹⁰²⁻¹⁰⁴ As demonstrated in their Pourbaix diagram (**Figure 1.6**), the phase transitions of both zinc and MnO₂ shifts significantly when the electrolyte pH is change from alkaline to slightly acidic (pH < 6). Significantly, the electrochemically inactive Mn₃O₄ and the chemically passive ZnO would simply not form in this system, while zinc hydrogen evolution is also believed to be limited by high overpotential.¹⁰⁵ As such, theoretically, this system has great potential of achieving high rechargeability.

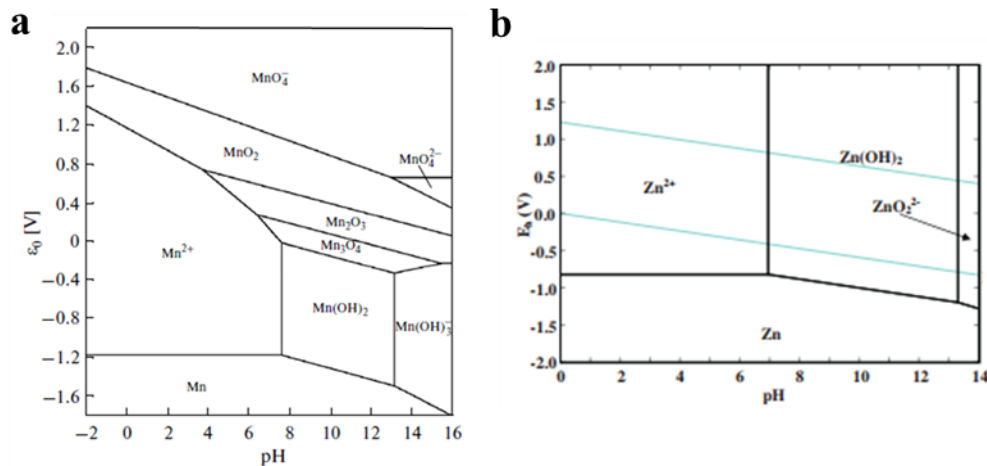


Figure 1.6 The Pourbaix diagram of a) manganese and b) zinc at 25 °C. Diagram A obtained from work of Boytsoda *et al.*,¹⁰⁶ and diagram B adapted from work of Al-Hinai *et al.*¹⁰⁷

Of all the different types of MnO₂, α -MnO₂ is the most studied for this system; mainly due to their relatively stable [2×2] tunnels that can accommodate the intercalation/deintercalation of Zn²⁺ ions.³² Other crystal types such as β -, δ - and spinel

MnO₂ have also been investigated.^{31,108-110} Various reaction mechanisms of these rechargeable mildly acidic Zn-MnO₂ (RMAZM) batteries have been proposed as well, but there has yet to be one which is fully agreed upon by the research community. The discussions have mostly been revolving around two reactions, the MnO₂ conversion reaction and zinc intercalation reaction.^{21,31,109-112} Though, they are not completely incompatible and it is possible for both reactions to occur during the discharge.¹¹² The different results are likely due to the variation in the initial MnO₂ crystal structure of each study, which can influence the reaction paths. The likelihood of MnO₂ polymorph being present in the system also adds onto the difficulties of the investigation.

Despite some contracting results in the mechanism investigations, a common consensus in previous studies is the occurrence of Mn²⁺/Mn³⁺ dissolution, which leads to capacity fade through loss of active materials. The undesired dissolution originates from the crystal lattice mechanism of Jahn-Teller distortion. In which, the Mn³⁺ ions, in the discharge products, with an unstable high-spin d⁴ electronic configuration experience an elongation of their $d_{x^2-y^2}$ and d_{z^2} orbitals; this electron cloud movement facilitates the Mn³⁺ species to undergo structural transformation in the form of disproportionation reaction that eventually give Mn⁴⁺ and water soluble Mn²⁺ (**Equation 1.7**).^{113,114} The dissolution phenomenon is not a standalone case for aqueous batteries, but an intrinsic property of Mn³⁺ that has also been reported in lithium batteries with organic solvent.¹¹⁴⁻¹¹⁶



In 1988, an idea to resolve the dissolution issue was first proposed by Kim *et al.*¹¹⁷ The strategy aims to reduce the manganese dissolution by pre-addition of Mn²⁺ ions (0.1 - 0.5 M MnSO₄) into the electrolyte; it significantly raised the life span of the system to 120 cycles. This strategy was further optimized by Pan *et al.* recently,²¹ who demonstrated a Zn- α -MnO₂ battery, using 2M ZnSO₄ electrolyte and 0.1M MnSO₄ additive, that maintained 92 % of its capacity after being cycled at 5C (1C =308mAh g⁻¹) for 5000 cycles. Following this study, Zhang *et al.* also successful prepared a Zn- β -MnO₂ battery using the same strategy but with 3M Zn(CF₃SO₃)₂ and 0.1M Mn(CF₃SO₃)₂ in the electrolyte; the battery maintained 94% of its initial capacity after being cycled at 6.5C for 2000 cycles.³¹ Later studies built on these foundations and optimize the system

even further for future applications. For example, Li *et al.* fabricated “extremely safe” and flexible Zn/ α -MnO₂ batteries using a gelatin and polymer composite separator that withstand different destructive tests while maintaining majority of its capacity (> 80%).¹¹⁸ In another approach, Wu *et al.* combined α -MnO₂ with graphene to further improve the rate capability of the system.¹¹⁹

Table 2 Low current cycling of RMAZM batteries in recent publications

MnO₂ phase	Electrolyte	Low current examination	Ref
α -MnO ₂	2M ZnSO ₄ 0.1M MnSO ₄	1C, 60 cycles	21
β -MnO ₂	3M Zn(CF ₃ SO ₃) ₂ 0.1M Mn(CF ₃ SO ₃) ₂	0.32C, 100 cycles	31
ε -MnO ₂	2M ZnSO ₄ 0.2M MnSO ₄	1.3C, 300 cycles (lost 43% capacity in 20 cycles)	112
Graphene and α -MnO ₂	2M ZnSO ₄ 0.2M MnSO ₄	1C, 100 cycles	119

While the cyclability results of these RMAZM batteries are very promising, they were always achieved at high current with compromised capacity. Meanwhile, the low current cyclability performance of these batteries has not received much less attention. As listed in **Table 2**, the low current (< 2C) examination of the batteries in previous studies have mostly been limited to 100 cycles. The lack of experiments under such testing condition may lead to misjudgement of an important phenomenon. Precisely, during charging, Mn²⁺ ions added to prevent the dissolution of Mn³⁺ species can be oxidized to MnO₂, which was reported to contribute extra capacity, improve ionic conductivity and improve electrode structural integrity.^{31,108} However, this in-situ electrodeposited MnO₂ should have crystal structure similar to EMD, which is not optimal for zinc intercalation and therefore less valuable to battery performance compare to the pristine MnO₂. More importantly, the non-stop occurrence of this phenomenon will deplete the Mn²⁺ ions added to prevent Mn³⁺ dissolution and capacity lost. Investigations of how the system react and change throughout the process will provide useful insights and information that are necessary to achieve high life span in low current cycling condition with RMAZM batteries.

1.6 Research Objective

This thesis can be divided into two main objectives, with both being a part of the goal to achieve long lasting and high performing RMAZM batteries.

1. The first part of the thesis aims to investigate and develop understanding on the fundamentals of the RMAZM batteries and the phenomenon of in-situ Mn^{2+} electrodeposition within the system. The target is to explore the $\alpha\text{-MnO}_2$ reaction mechanism as well as to determine the capacity fading mechanism with the presence of Mn^{2+} additive. Various factors and cycling condition will be explored to gain better insight about the MnO_2 electrodeposition process. Also, the identity and transformation mechanism of the deposited MnO_x species will be examined with various characterization techniques. In the end, every pieces of the puzzle will be linked together to form a complete description of the system to allow the identification of key points that can be modified to extend battery life cycle.
2. In the second part of the thesis, the goal is to incorporate the developed understanding of the system into designing MnO_2 electrodes that have improved cyclability at low current and deep cycling, as well as the already demonstrated excellent rate performance and good cyclability at high current. Specifically, the MnO_2 electrodeposition reaction is explicitly targeted as an undesired reaction and is suppressed through manipulation of its reaction kinetic. The effectiveness of the strategy is demonstrated by a MnO_2 electrode that hinders the Mn adsorption and post cycling characterization is also presented to confirm the connection between the improved stability and the strategy.

1.7 Organization of Thesis

This thesis is organized into five chapters. **Chapter 1** introduces general background, history, recent research progress of Zn- MnO_2 batteries, and motivation of the thesis work. **Chapter 2** presents various characterization and performance measurement techniques adapted throughout the thesis. In **Chapter 3**, the reaction mechanism of rechargeable aqueous mildly acidic Zn- MnO_2 batteries is discussed. The mechanism, benefits and issues of Mn electrodeposition within these Zn- MnO_2 batteries

are also presented in this chapter. **Chapter 4** focuses on the strategy proposed to reduce the frequency of Mn electrodeposition and in such increase the low current cyclability of the batteries. The strategy has also brought rate performance improvement to the batteries, which will also be discussed in the chapter. Lastly, in **Chapter 5**, a summary and suggestions for future direction of the thesis work are provided.

2 Chemicals and Characterization Techniques

2.1 Materials

All materials were used as received without further purification. The list of chemicals and their supplier and specification is provided in Table 2.

Table 3 List of Chemicals

Chemical	Supplier
Manganese Dioxide (MnO ₂)	Sigma Aldrich
Manganese sulfate monohydrate (MnSO ₄ •H ₂ O)	Sigma Aldrich
Potassium Permanganate (KMnO ₄)	Sigma Aldrich
Sulphuric Acid (H ₂ SO ₄)	Sigma Aldrich
Expandable Graphite / Sulphuric Acid intercalate Graphite (C ₂₄ H ₂ SO ₄ (H ₂ SO ₄) ₂)	Sigma Aldrich
Zinc Sulfate Heptahydrate (ZnSO ₄ •7H ₂ O)	Sigma Aldrich
Ethanol (EtOH)	Sigma Aldrich
Super P Carbon Black (SP CB)	Imerys Graphite & Carbon
Polyvinylidene fluoride (PVDF)	Sigma Aldrich
N-Methyl-2-pyrrolidone (NMP)	Sigma Aldrich

2.2 Physical Characterization

2.2.1 Scanning Electron Microscopy

Scanning Electron Microscopy (SEM) is a physical characterisation technique mainly used to image surface morphology and structure of samples. As suggested by its name, the technology utilizes electrons as the information carriers instead of photons used in optical microscopy. The main advantage of adapting electrons in the imaging tool is their drastically smaller wavelengths in comparison to visible light, which provide SEM with the high resolution (~10 nm) necessary to obtain details image nanomaterials.

In general, SEMs consist of an electron gun, one or two condenser/objectives lens and different electron detectors within an ultrahigh vacuum system. The electron gun contains a filament (tungsten or lanthanum hexaboride) which can be thermally activated to emit electrons. Once released, the electrons are accelerated by an electric field (5-20kV), and then directed onto the samples by the condensers and objective lenses. The electrons are highly energetic, and therefore needs the ultrahigh vacuum to avoid any undesired interaction with gas molecules. Upon striking the samples, the electrons can be adsorbed or scattered, which generate signals such as secondary electrons, back scattering electron, characteristic X-ray, cathodoluminescence, etc. In SEM, the signals of interest are the secondary electrons and the back scattering electrons; these electrons will turn into current when measured, and the intensity of the current will be reflected on the brightness of the image.

The SEM images in this thesis were collected with a Zeiss ULTRA plus Field Emission Scanning Electron Microscope (FESEMs). The samples were glued onto an aluminum sample holder using a double sided carbon adhesive. The electron beam was accelerated with a voltage of 20kV. In this thesis, SEM was used to observe the morphology of the pristine α -MnO₂ nanorods and the MnO_x species that were grown onto the cathode electrode after they were charged and discharged. It was also use to examine the quality of various carbon-based substrate materials as well as their capability of reducing the rate of MnO₂ electrodeposition.

2.2.2 Transmission Electron Microscopy

Similar to SEM, Transmission Electron Microscopy (TEM) also uses high energy electron beam to probe the structure of samples. In contrast to SEM though, TEM provide information about interior compositions rather than surface of the sample; they generally have higher resolution as well. In TEM, the electron beams are often much higher in energy (60-300 keV), and it is the electrons that transmit through the samples which are being measured. When passing through the samples, the interactions between the electrons and the matters will change the number of measured electrons, which then lead to a variation of brightness in the final images. Typically, TEM samples are limited to have thickness under 1 μm ; the exact values vary depending on power of the electron beam.

The TEM images in this thesis were collected with a Philips CM 10 TEM and the HRTEM (High resolution Transmission Electron Microscopy) images were obtained from a FEI TITAN 80-300 LB TEM/STEM. The samples were first sonicated in ethanol and then drop casted onto an amorphous carbon coated copper mesh. The electrons beam of the TEM has energy of 60 keV and the HRTEM used one with 200 keV. TEM is used to investigate the morphology transformation of the $\alpha\text{-MnO}_2$ nanorods after cycling. It also assisted in confirming the morphology of the electrodeposited MnO_2 . Furthermore, it was used to investigate the amorphous region found in the cycled MnO_2 and to observe the interlayer spacing directly. The results serve as important components in supporting the reaction mechanism proposed.

2.2.3 Energy-Dispersive X-ray Spectroscopy

Energy-dispersive X-ray spectroscopy (EDX) is an analytical method used to characterize and estimate the elemental composition and distribution of a sample. EDX is often part of an electron microscope, it evaluate the characteristic X-ray given off by the samples after they are stroked by the electron beam. The X-ray emission occurs when the electron beams eject some ground/low energy inner shell electrons of the samples and allows higher energy outer shell electrons to occupy those lower energy states by giving off some of its energy through photon emission. Since the energy level of each electron orbital is quantized and each element has its own unique set of orbital energy, each

element must also have its own unique set of characteristic X-ray. Hence, by measuring the number and energy of the emitted X-ray, the identity and composition of the samples can be identified and approximated.

For this work, EDX and elemental mapping are used to characterize the MnO₂ electrode before and after cycling. The amount and distribution of the five elements K, Zn, Mn, C and O were measured and adapted to explain the transformation of the MnO₂ nanorod. The EDX analyses of the electrodeposited MnO_x species are also important for supporting the proposed capacity growth and fading process in the RMAZM batteries.

2.2.4 X-Ray Diffraction Analysis

X-Ray Diffraction (XRD) analysis is a rapid and non-destructive characterization technique that analyzes the crystal structures of given samples. It is often used to identify samples by comparison with known JCPDS reference, and it can also provide useful information such as grain sizes, strain and thermal expansion. The working principle of XRD is based on the phenomenon of light interference, in which, the crystal lattice of the samples act as diffraction grating for the incident light. In a typical scan, a monochromatic light beam is directed to the sample in varying incident angles, and the diffracted beam is measured. The Bragg's Law (**Equation 2.1**) is the principle which describes this process. In this equation, λ is the wavelength of the incident beam, θ is the beam incident angle and d is the distance of the interplanar spacing. When θ takes a value such that n becomes a positive whole integer, the diffracted rays will interfere constructively, leading to resonance of the light wave and hence generate a peak in the XRD spectrum. On a side note, the values of λ and d need to be in similar order of magnitude for optimal diffraction, hence X-ray is often chosen as the beam source to measure the interlayer spacing in the angstrom range.

$$n\lambda = 2d\sin\theta \quad (2.1)$$

XRD measurements in this thesis were collected with Rigaku Miniflex 600 X-ray Diffractometer equipped with a graphite monochromator and a Cu K α radiation source ($\lambda=1.5406\text{\AA}$). The XRD scans were collected from 5 ° to 80 ° with a scan rate of 1 °min⁻¹. XRD was performed to investigate the crystal structure transformation of the α -MnO₂ and undesired electrodeposited MnO_x species. The observation of the (001) diffraction peak

of layered manganese oxides from cycled cathode electrode was the starting point in formulating the newly proposed capacity fading mechanism. Furthermore, the shifting of the α -MnO₂ intrinsic peaks discovered by the XRD analysis was also important for explaining the activation process of the α -MnO₂ in the early cycles.

2.2.5 X-Ray Photoelectron Spectroscopy

X-Ray Photoelectron Spectroscopy (XPS), also known as Electron Spectroscopy for Chemical Analysis (ESCA), is a quantitative technique which analyzes the surface chemistry of samples. Its functionalities include identification of elements, measurement of elemental composition, as well as determination of chemical and electronic states of the elements. XPS is built on the principle of photoelectric effect which describes the phenomenon of electron emission from a solid medium by light radiation and introduces the idea of Wave-particle duality. Using the principle, the measured kinetic energy of the ejected electrons can be correlated to their binding energy in the atomic orbitals. Since each element has a characteristic set of binding energies, the elements in a material can be identified by simply comparing the measured spectrum to the known reference. Furthermore, since binding energies may vary due to formation of chemical bonds or change in oxidation states, shifting of the characteristic peaks can also provide useful information of chemical and electronic states of the elements.

In this thesis, XPS analyses were conducted with a K-Alpha X-ray Photoelectron Spectrometer System. The result was used to confirm the presence of Zn in the cathode electrode, which is meaningful to explain the Zn-intercalation mechanism. Ex-situ 2p_{1/2}, 2p_{3/2} and 3s adsorption peaks of manganese during different stages of cycling were also studied for better understanding of the charge/discharge mechanism and the disproportion reaction previously reported.

2.2.6 Raman Spectroscopy

Raman spectroscopy is one of the many spectroscopic techniques that use matter and light interaction to probe structural and bonding information of molecules. Specifically, it measures inelastic scattering of light by molecules, in which the interaction between the light wave and the molecules changes the energy of the scatter

light. Raman and infrared (IR) spectroscopies are often collected as complementary to each other, they both use IR radiation that excite molecules to higher vibrational or rotational states. IR and Raman adsorption are mutually exclusive in molecules that have center of inversion. For a vibration to be Raman active, the vibration must cause a change in polarizability of the molecules when it occurs; to be IR active, the vibration must changes the dipole of the molecules.

In this thesis, Raman spectra of the samples were collected with a Bruker Sentterra System using an excitation line with wavelength of 532 nm. Since α -MnO₂ has multiple Raman adsorptions near 640cm⁻¹, 572cm⁻¹, 385cm⁻¹ and 183cm⁻¹, each representation a specific vibration of the MnO₂ crystal ladder, Raman spectrum of α -MnO₂ can provide additional informational about the bonding state of the active material. Furthermore, the I_D and I_G peaks of the expanded graphite were measured using Raman spectroscopy to confirm their graphitization during the thermal shock treatment.

2.2.7 Inductively Coupled Plasma Atomic Emission Spectroscopy

Inductively coupled plasma atomic emission spectroscopy (ICP-AES) is an analytic technique that is capable of detecting and precisely measuring trace level of elements. ICP-AES generally utilizes argon plasma generated by induction heating to thermally excite electrons in an atom at a temperature around 7000 to 10000 K. The intensity measurement of the characteristic radiation emitted by the excited atoms during their relaxation process would then be used to determine the identity and concentration of elements presence in the samples.

In this work, ICP-AES is performed with a Perkin Elmer Ltd. It was specifically used to measure changes of manganese ion concentration in the electrolyte of a carbon|ZnSO₄+MnSO₄|zinc wet cell. This experimental result was used to demonstrate the correlation between the consumption of manganese ion and capacity growth of RMAZM batteries.

2.3 Electrochemical Characterization

2.3.1 Galvanostatic Discharge/Cycling

Galvanostatic discharge test is an electrochemical performance examination method that provides key information of batteries. In this test, the Galvanostat applies a constant current through the electrolytic cells until a cut-off voltage is reached while measuring the cell potential. It identifies the voltages of the discharge plateaus as well as the practical capacity of the batteries. Upon completion of the discharge process, the direction of the current can be reverse to charge the batteries. For battery analysis, the values of the current are usually set based on the theoretical capacity of the targeted material. They are often represented in C-rate, which is inversely proportional to the time in hours the current takes to completely drain the theoretical capacity of the material. For example, MnO_2 has a theoretical capacity of 308 mAh g^{-1} , so currents of 308 mA and 1640 mA would be 1C and 5C for 1g of MnO_2 , respectively.

The life cycles and durability of batteries can be determined by prolong cycling of Galvanostatic charge and discharge. Other important battery properties such as columbic efficiency, specific capacity, energy efficiency, operating voltage can also be monitor in these tests. Furthermore, testing criterions such as C-rates, number of cycles, charge/discharge/resting periods, and cut-off voltage can also be varied to stimulate and evaluate the performance of the batteries in specific conditions.

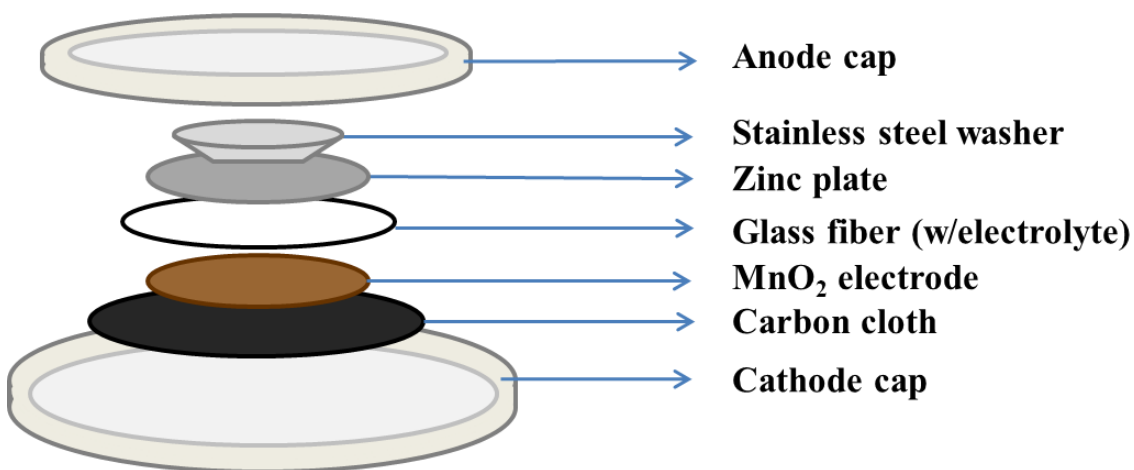


Figure 2.1 Sample illustration of the general coin cell assembly.

In this thesis, the Galvanostatic discharge and cycling were conducted on a LAND-CT2001A battery tester. The electrode materials were assembled into batteries using CR-2032 stainless steel coin cells in ambient condition and an example of the coin cell assembly is demonstrated in **Figure 2.1**. The MnO₂ electrodes are prepared by either the standard doctor blade method or a filtration method, more details of process will be provided in later chapters. The 2M ZnSO₄ and 0.1M MnSO₄ electrolyte was precisely controlled to be 50μL and the zinc plate has thickness of approximately 0.1 cm. The circular carbon cloth has a radius of 0.9 cm, and it was added to reduce contacts and side reactions between the electrolytes and the caps. Upon complete construction of the coin cells, they were sealed with a coin cell punch machine. The electrochemical performance of the MnO₂ electrode were evaluate in the voltage range of 1.0 to 1.8V vs Zn/Zn²⁺. The cycling durability of the MnO₂ electrodes was evaluated at cycling rates of 1C and 5C. The rate capability of the MnO₂ electrodes was tested at 1C, 2C, 4C, 6C, 8C, and 10C consecutively; 5 cycles of charge and discharge are performed at each C-rate.

2.3.2 Cyclic Voltammetry

Cyclic voltammetry (CV) is an electrochemical analysis technique which can be used to study the characteristics of electrolytic cells. In a general CV experiments, the potential between the working and reference electrode is sweep linearly within a predetermine voltage window, and the current produce at the working electrode is measured during the process. A cyclic voltammogram can be generated by plotting the current versus the potential, which allows direct investigation on the redox reactions of the system. Continuous sweeping of the potential can also be used to inspect the change of the system as well as the durability of the materials.

The CV scans in this thesis were collected using a Gamry Interface 5000E potentiostat. The MnO₂ was assembled into coin cells as previously describe and the CV scans were collected in a two electrode system at a CV scan rate of 0.1 mV s⁻¹. The CV results mainly serve as complementary information to the data obtained from Galvanostat discharge and cycling, providing extra information about changes of the reaction mechanism during the activation process.

3 Investigation of Manganese Dioxide Electrodeposition in Rechargeable Mildly Acidic Zn-MnO₂ Batteries

3.1 Introduction

As discussed in Chapter 1, the electrochemical reactions within RMAZM batteries are a complex system that has multiple levels of variabilities. Although the batteries have already demonstrated outstanding cyclability when cycled at high current density, knowledge about their reaction mechanisms and possible side reactions are still limited. Currently, there are the two reaction mechanisms that have received the most recognition by the scientific communities. First is the zinc intercalation reaction, in which Zn²⁺ ions inserted into the crystal lattice of MnO₂ to form ZnMn₂O₄. During this reaction, the MnO₂ may or may not undergo phase transformation depending on its initial crystal structures; α -, β -, δ - and λ - MnO₂ have all been reported to undergo this reaction mechanisms to some extent.^{31,32,109,113} The second mechanism is the conversion reaction of MnO₂ to MnOOH. This reaction path for MnO₂ in mildly acidic condition is first proposed by Pan *et al.*,²¹ and is also a well-known transformation of MnO₂ in alkaline conditions.²³ However, both mechanisms alone cannot explain the discharge behaviors of the batteries, which is later resolved by Sun *et al.* who proposed a mechanism in which zinc intercalation and MnO₂ conversion occur consecutively.¹¹²

Nevertheless, the current knowledge about the RMAZM batteries system is not complete and there are still many questions about the left to be answered. For example, although the capacity growing phenomenon has been reported, its negative impact and reaction mechanism is still unknown. Performance degradation and long term transformation of the cathode materials with Mn²⁺ additive presence in the electrolyte has yet to be investigated. Finally, examining the activation process of the MnO₂ may also lead to identification of properties previously unknown. The answers to these questions will improve basic understanding of the system that would eventually serve as the foundation for further optimization of the batteries. As such, in this chapter, different scientific/technical perspectives of the battery systems including MnO₂ crystal structure, surface morphology, electronic states and electrochemical performance are systematically

studied. At the end, the results of these investigations are correlated and incorporated with findings in previous publications to form a more refined and mature description of the system.

3.2 Experimental Methods

3.2.1 Synthesis of α -Manganese Dioxide

The α -MnO₂ nanorods were synthesized using a procedure demonstrated by Pan *et al.* with minor modifications²¹. First, 0.003 M MnSO₄•H₂O and 120 μ L of H₂SO₄ were added to 40 mL of deionized distilled water (DDI) and magnetic stirred at 500 rpm for 10 mins. Then 0.2218 g of KMnO₄ was dissolved in another 30 mL of DDI to form a dark purple solution. The KMnO₄ solution was then slowly added to the MnSO₄ solution under stirring at 500 rpm. Upon addition of the KMnO₄ solution, minimal amount of brown precipitate will appear and the mixture was stirred in room temperature for another 2 hrs. The solution was then sealed within a Teflon lined hydrothermal synthesis autoclave reactor and heated at 120 °C for 12 hrs. The solvent would turn colorless and transparent when the reaction is completed. The brown powder product was collected by filtration and was washed by DDI and ethanol (EtOH). Lastly, they were dried in a vacuum oven at 80 °C for another 12 hrs before characterization and electrochemical testing.

3.2.2 Preparation of Manganese Dioxide Electrode

First, α -MnO₂ nanorods, Super P carbon and Polyvinylidene fluoride (PVDF) were added to a glass vial in a weight ratio of 70:20:10 with N-Methyl-2-pyrrolidone (NMP) as solvent. The weight ratio of the solvent and the solid material is 10:1. The mixture is magnetically stirred at 500 rpm for 5 mins, and then at 300rpm overnight (>12hrs) to obtain a homogeneous slurry. The slurry was then doctor blade coated onto a carbon fiber paper to form the MnO₂ electrode. The electrode was left to dry in ambient air for over 2 hrs and then dried in a vacuum oven at 80 °C overnight (>12hrs).

3.2.3 Preparation of Polymer-free/Self-standing Manganese Dioxide electrode

15 mg α -MnO₂ nanorods and 5 mg carboxylate activated carbon nanotubes (CNT) were first mixed in 40mL of EtOH. The dispersion is then sonicated for over 3 hrs in a seal beaker. After sonication, the dispersion was filter onto a glass fiber (VWR, Glass Microfibre Filter 691, 4.5cm diameter) to form the polymer-free electrode. The thin film electrode was dried in ambient condition overnight (>12hrs) and weighted before use. The active material loading is approximately 1.5mg cm⁻². To prepare the self-standing electrode, the dispersion was filter onto polyethersulfone filter papers (Pall Corporations, Supor[®] membrane), and then peeled off after the electrode was dried. Pure CNT films of similar mass were prepared as reference using the exact same procedure, but without any of the MnO₂.

3.3 Results and Discussions

3.3.1 Characterization and Electrochemical Analysis of α -MnO₂

The as-prepared MnO₂ brown powders were first characterized by XRD, Raman spectroscopy, SEM and TEM. As shown in the XRD result (**Figure 3.1a**), the MnO₂ powder exhibit major diffraction peaks at 12.8 °, 18.1 °, 28.8 °, 37.5 °, 42.0 °, 49.9 °, 56.4 °, 60.3 °, 69.7 ° and 78.6 °, corresponding to the (110), (200), (310), (211), (301), (411), (600), (521), (541) and (332) diffraction, respectively. The result aligns entirely with the peaks of α -MnO₂ reference (JCPDS: 44-0141), confirming the crystal phase of the sample. The adsorption peaks at 183, 383, 576 and 640 cm⁻¹ measured in the Raman spectroscopy (**Figure 3.1b**) resemble the ones that have been previously reported. They were assigned to the external vibration of the MnO₆ translation motion, Mn-O bending mode and the latter two peaks are proposed to be originated from the lattice breathing vibration^{120,121}. SEM image of the α -MnO₂ (**Figure 3.1c**) shows that they have a nanotube-like morphology, with widths ranging between 20 to 100 nm and lengths between of 1 to 5 μ m. TEM image of the α -MnO₂ nanorods (**Figure 3.1d**) also displays similar findings on the material dimensionality. Additionally, it shows that some of the nanorods may have a hollow interior. The observed morphology of the α -MnO₂ also matches well with previously reported results.²¹

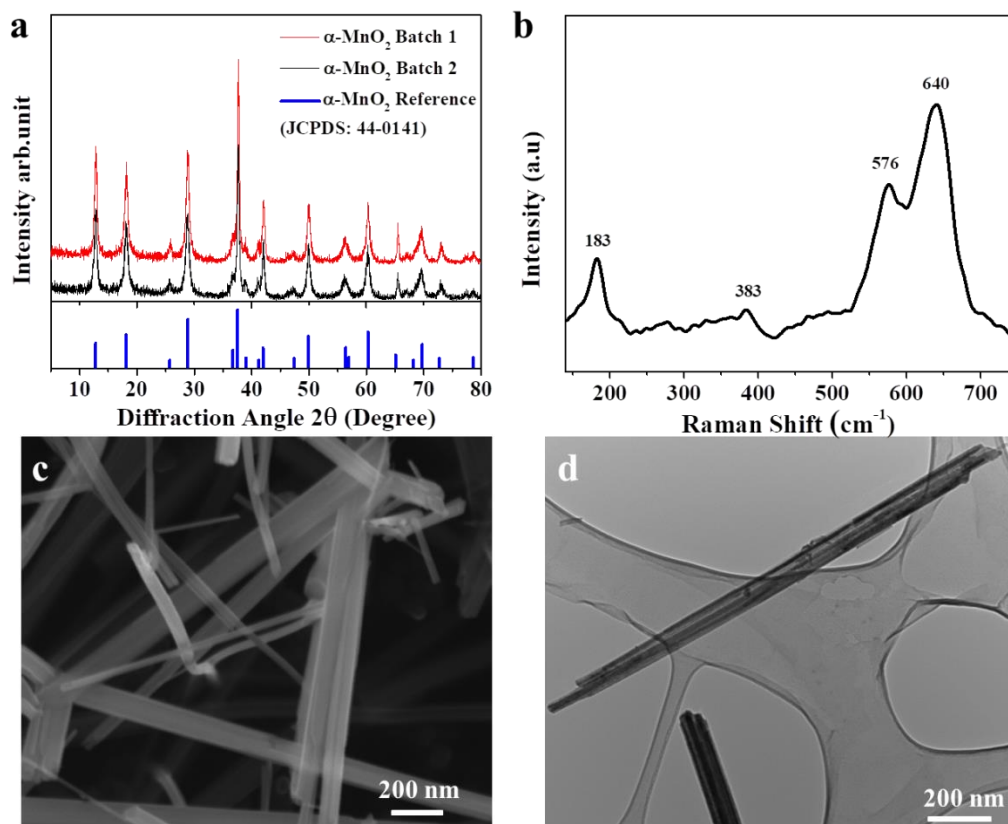


Figure 3.1 a) XRD analysis b) Raman spectrum, c) SEM image and d) TEM image of α - MnO_2 nanotubes.

After confirming the identity of the α - MnO_2 nanotubes, they were prepared into a standard electrode by doctor blade coating and were assembled into coin cells with a zinc plate anode using 2 M ZnSO_4 electrolyte with or without 0.1 M MnSO_4 additive. The open circuit voltage (OCV) of these batteries ranges between 1.40-1.45 V and often lowers to near 1.38 V after prolong periods of resting. **Figure 3.2a** is the first two charge and discharge curves of the two batteries under 1 C drain. Aside for minor differences in the total specific capacity, there are very little differences between the discharge curves of the two batteries. In the first discharge sequence, the voltages of both batteries would first quickly fall from OCV to 1.20V-1.25 V and remain relatively constant until near the end of the discharge process, when the voltage will fall sharply to 1.0 V. In the second cycle, the discharge curve changes into one with two plateaus locating at 1.45 V and 1.35 V, which have been assigned to the conversion reaction and Zn-intercalation reactions, respectively.¹¹² Though, the reasons for the change between the first and second cycle remains unresolved. As for the charging curves, two plateaus can be found

at 1.5 V and 1.6 V. The major differences between the first and second charge curves are the reduced overall capacity as well as the shift in the contribution of the two plateaus.

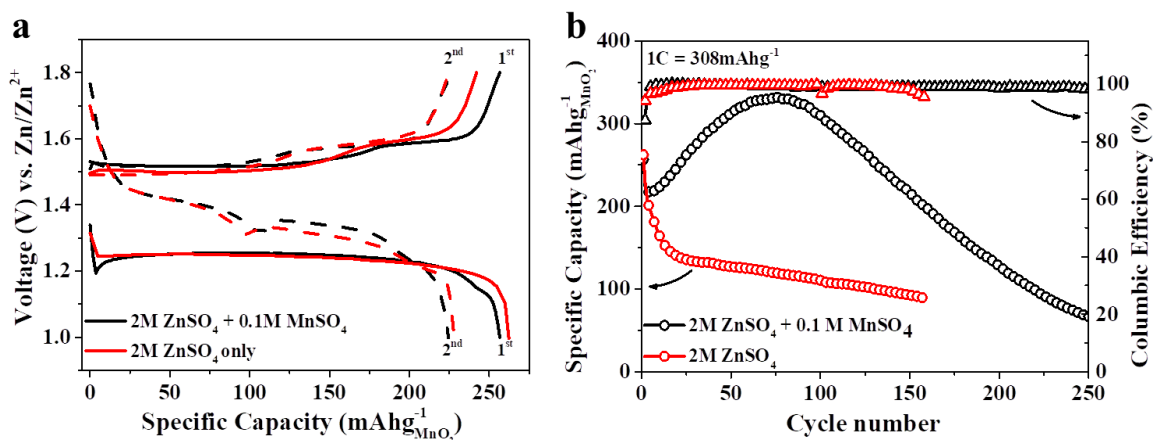


Figure 3.2 a) Galvanostatic charge and discharge curves in the first two cycles and b) specific capacity profile at 1C of the Zn/ α -MnO₂ batteries with and without 0.1 M MnSO₄.

Figure 3.2b is the specific capacity profiles of the two batteries cycled at 1C. Both batteries maintain columbic efficiencies of over 99% for majority of their life span. The battery without the Mn additive shows fast capacity fade in the first 20 cycles which continued but with slower rate in latter cycles. This result is in agreement with results in previous publications.^{21,113} Surprisingly, batteries which used the MnSO₄ additives not only have reduced capacity fade, but demonstrated long periods of capacity growth for over 75 cycles. During which, there are no significant changes in voltages of the discharge plateaus. The capacity peaks at values near 320-330 mAhg⁻¹ which is beyond the one electron theoretical capacity of MnO₂, hence, the capacity growth cannot be caused by the slow activation of the material.

Moreover, pre and post cycling SEM images of the electrode surface (**Figure 3.3a and 3.3b**) and SEM and EDX analysis of the electrode cross section (**Figure 3.4a, 3.4b and 3.4c**) discovered a brand new layer of porous MnO_x nanosheets covering the initial α -MnO₂ nanorods and the carbon nanoparticles. As shown by the EDX mapping, this layer has significantly less carbon content compare to the originally coated layer, indicative of the fact that they are grown on upon cycling. Base on the above result, a possible hypothesis for the capacity growing result is that additional MnO_x are slowly being generated during the cycling process by in-situ electrodeposition of the pre-added Mn²⁺ ions and contributed extra capacity. According to standard potential calculations

(Appendix 6.1), the Mn electrodeposition reaction becomes thermodynamic favorable when a voltage above 1.53V vs. Zn/Zn^{2+} is applied. This voltage is well within the operating voltage range (1.0 - 1.8V vs. Zn/Zn^{2+}) of the RMAZM batteries and will constantly occur unless forbidden by other factors.

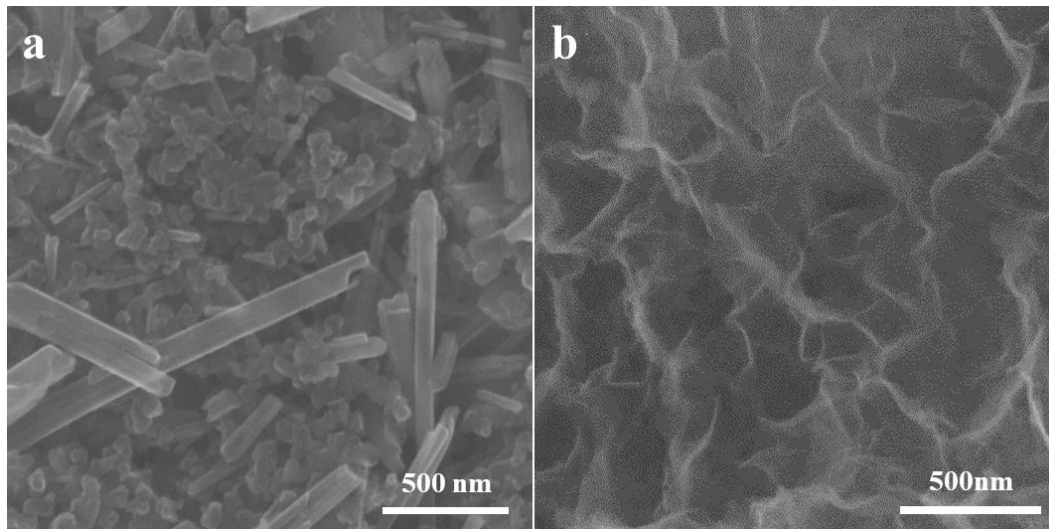


Figure 3.3 a) SEM images of standard $\alpha\text{-MnO}_2$ electrode before and b) after cycling.

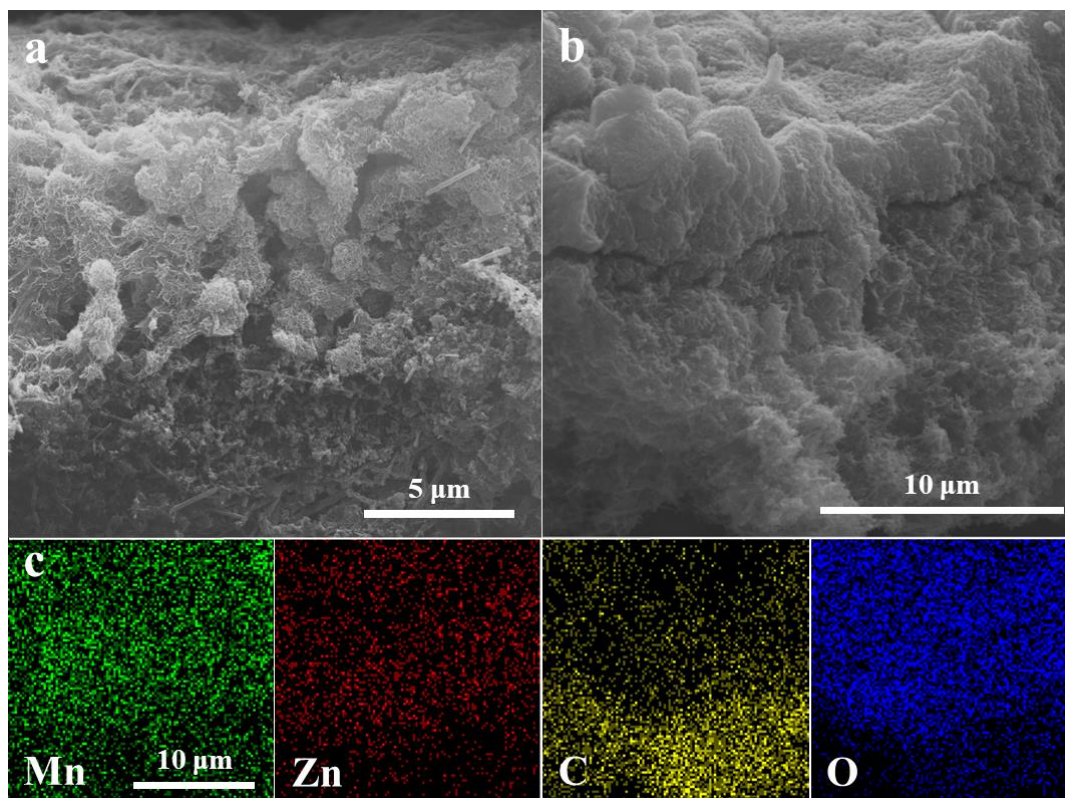


Figure 3.4 a) SEM cross section image of the cycled $\alpha\text{-MnO}_2$ electrode and b, c) corresponding SEM and EDX analysis of an area in the cross section of the cycled $\alpha\text{-MnO}_2$ electrode.

The above hypothesis regarding the occurrence of in-situ Mn^{2+} electrodeposition aligns with findings in few recent studies, but investigations of the phenomenon have focused only on the benefits it provide such as extra capacity and extra electrode protection.^{31,108} Yet, possible consequences and factors which influence or control the phenomenon were hardly mentioned nor studied. For example, a rarely discussed but key observation about the phenomenon is that upon peaking, the battery capacity is not maintained, instead it would begin to experience fading at a fast rate. The battery would lose more than half of its peak capacity in the next 100 cycles, and the reduction will slow down only when the capacity falls below 50 mAh g^{-1} or 25% of the initial battery capacity, at which the battery have very little practical value.

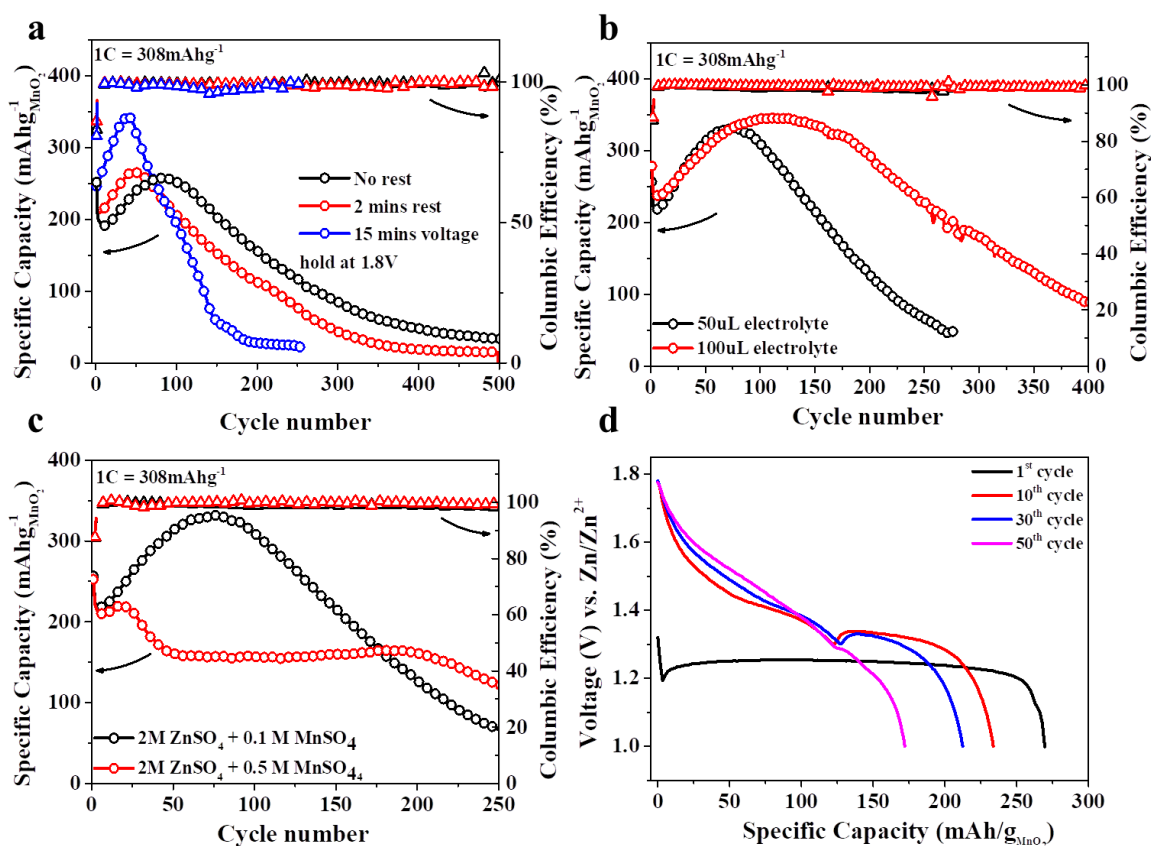


Figure 3.5 a) Specific capacity profiles of the RMAZM batteries with different cycling protocols, b) different amount of electrolyte and c) different MnSO_4 concentration. d) Galvanostatic discharge curves of RMAZM batteries using 0.5M MnSO_4 additives at different cycles.

To learn more about the phenomenon, RAMZM batteries were prepared with different specification and further examined under different cycling conditions. First, the batteries were tested with three cycling protocols, one with standard cycling in which the

batteries are charge and discharge consecutively at 1C; the next protocol adds a two minute resting interval between every charge and discharge sequence; the final protocol adds an additional 15 mins of constant voltage hold at 1.8V after every charging process.

Figure 3.5a is the cycling performance of the batteries collected with the three testing conditions. It shows that both the resting period and the 15 mins constant voltage hold accelerated the rate of capacity growth. The later result is not surprising, since longer charging time provide more time for Mn^{2+} electrodeposition. The surprising finding is the connection between resting period and capacity growth; it suggest the kinetics of the electrodeposition in the batteries is likely dependent on the adsorption of Mn^{2+} ions to the electrode surface, which provides an alternative options in resolving/suppressing the issues. Another observation about these batteries with accelerated growth is their earlier plateaus and degradation. The link between accelerated growth and earlier peak/degradation hints the presence of a limiting factor for the capacity gain, and logical reasoning would point to the amount of available Mn^{2+} ions in being this factor.

Base on the above observations and reasoning, a direct method to extend the battery life span would be increasing the available Mn^{2+} ions either in the form of increasing electrolyte amount or increasing MnSO_4 concentration. **Figure 3.5b** shows the standard 1C cycling performance of RMAZM batteries with 50 μL and 100 μL of 2M $\text{ZnSO}_4 + 0.1\text{M MnSO}_4$ electrolyte. The extra electrolyte (or extra Mn^{2+} ions) extended the capacity growing and peaking period, but the battery capacity do eventually decays after the plateau. At first glance, the method succeeded, but it has little practical value as excessive amount of electrolyte would render the overall battery energy density. **Figure 3.5c** displays the effect of increasing MnSO_4 concentration to RMAZM batteries. Unfortunately, it is ineffective in resolving the issue as well. In fact, the battery with 0.5M MnSO_4 additive lost more than a quarter of its capacity within the first 50 cycles. While the capacity do stabilized afterward, it is at values ($\sim 160 \text{ mAh g}^{-1}$) which are no longer competitive and the decay would still occur after 200 cycles. **Figure 3.5d** displays the discharges curves of the battery using 0.5M MnSO_4 at the 1st, 10th, 30th and 50th cycles. It shows that the main capacity degradation during this period occurs in the 1.35V plateau, while the capacity of the 1.45V plateau saw little decay. Previous studies have

reported that adding excessive amount of MnSO_4 will cause adverse effects to the re-oxidation of manganese oxide, but the exact concentration limit fluctuate with systems and the specific mechanism is not well understood.^{21,112}

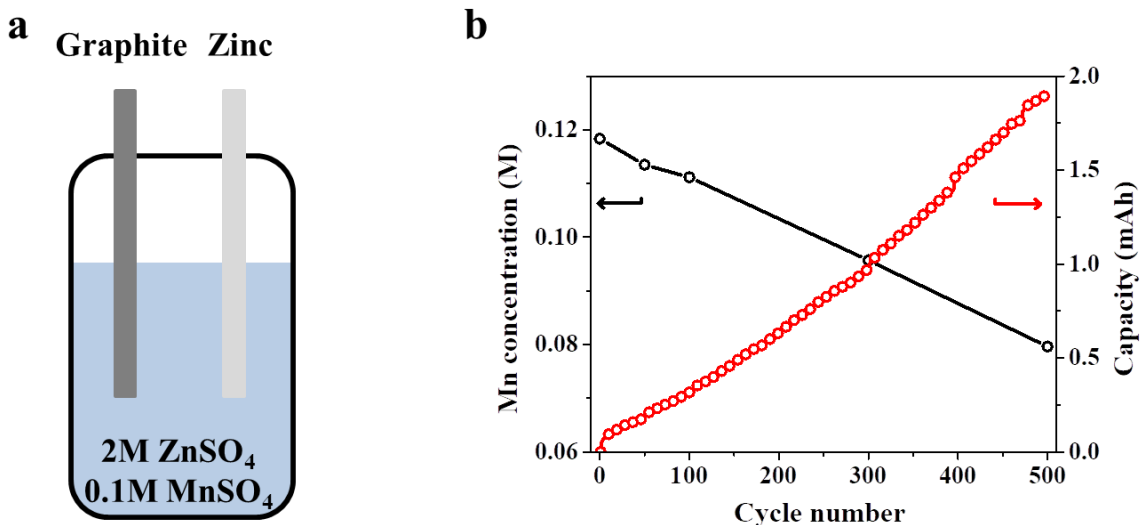


Figure 3.6 a) Diagram illustration of the graphite/Zn wet cell b) capacity and Mn concentration vs. cycle number graph of the graphite/Zn wet cell

To further confirm the correlation between capacity growth, Mn^{2+} electrodeposition and Mn^{2+} ion concentration, a wet cell consisting of graphite cathode, zinc anode and excessive amount of 2M ZnSO_4 + 0.1M MnSO_4 electrolyte (10mL) were prepared and cycled with additional resting periods and constant voltage holds (**Figure 3.6a**). As demonstrated in **Figure 3.6b**, the wet cell had near zero capacity in its first discharge which grew as the cycling process continues. Small amount of the wet cell electrolyte were collected at the 0th (initial), 50th, 100th, 300th and 500th cycles and their Mn concentrations were measured with ICP-AES. From the result, it is clear that Mn ions in the electrolyte are constantly being consumed. Given enough time, the Mn concentration will fall to levels that would no longer be capable of preventing the capacity degradation.

Based on the obtained results so far, one can state with confident that MnO_x electrodeposition does occur within RMAZM batteries and it is consuming Mn ions which would eventually lead to detrimental issues that degrade longevity of the batteries. Simple experiments on various electrolyte factors indicate that there is no easy fix to the issues. Therefore, it is necessary to study the phenomenon and obtain information that are

necessary to minimize the issue and further optimize the system toward better electrochemical performance.

3.3.2 Investigation of In-situ Manganese Oxide Electrodeposition

For more explicit and convenient investigations on the Mn^{2+} electrodeposition phenomenon, polymer and current collector free electrodes were prepared by direct filtration of the cathode material ($\alpha\text{-MnO}_2$ and CNTs) onto glass fiber separators. **Figures 3.7a** and **3.7b** are photos of the CNT only and the $\alpha\text{-MnO}_2$ and CNT (MC) thin film electrodes. The separator-cathode assemblies were measured to have a thickness of around 0.4 mm (~ 0.2 mm filter + ~ 0.2 mm electrode material). The electrode can also be prepared in a self-standing manner, with higher CNT content, which shows degree of flexibility that may be applied to flexible electronics (**Figure 3.7c** and **3.7d**).

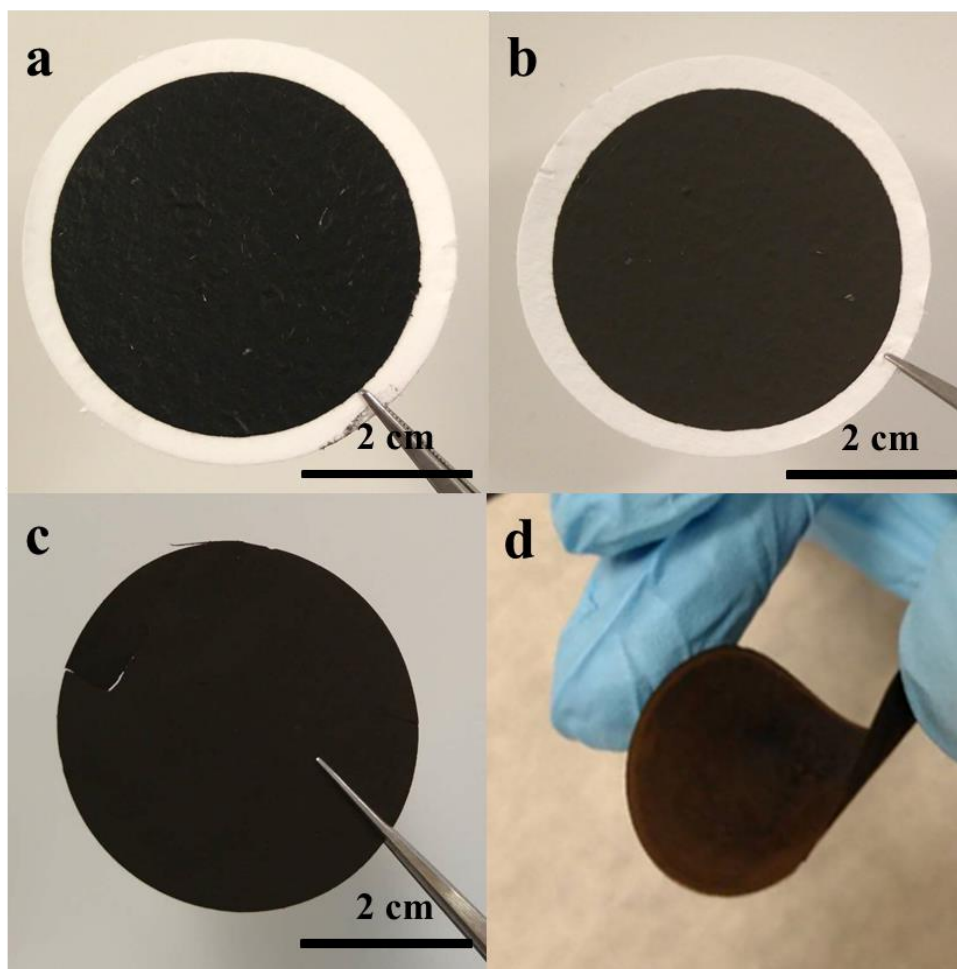


Figure 3.7 a) Photo of the CNT and b) MC thin film separator-assemblies. c) d) Photos of the self-standing MC electrode.

Examinations of the CNT and MC electrodes using the protocol containing the resting period and constant voltage hold steps show that both electrodes experience capacity growth and subsequent decay analogous to that of the standard electrodes (**Figure 3.8a**). As expected, the CNT electrode with insignificant amount of active material demonstrates near zero capacity initially and gains capacity as the cycling process continues. When MnSO_4 is not added to the electrolyte, the capacity growing phenomenon cease to occur, further confirms that extra capacity are being contributed by species generated through Mn^{2+} electrodeposition. **Figure 3.8b** shows the discharge curves of both MC and CNT electrodes at their 1st, 2nd, and 50th cycles. The MC electrode has discharge curves very similar to that of the standard electrodes, demonstrating a flat discharge plateau at 1.23V in the first discharge, which splits into two plateaus at 1.44 V and 1.35 V in later cycles. The capacity growth did not significantly change the plateaus voltage, and merely increase the length of the plateau. The CNT electrode on the other hand demonstrates no discharge plateau in the 1st cycle and a small sloping discharge curve in the 2nd cycle. By the 50th cycle though, two distinct discharge plateaus at 1.4V and 1.3V can be found, which are very similar to ones display by the MC electrode. The resemblance suggests a high likelihood of the deposited MnO_x participating in similar electrochemical reactions as the original active materials.

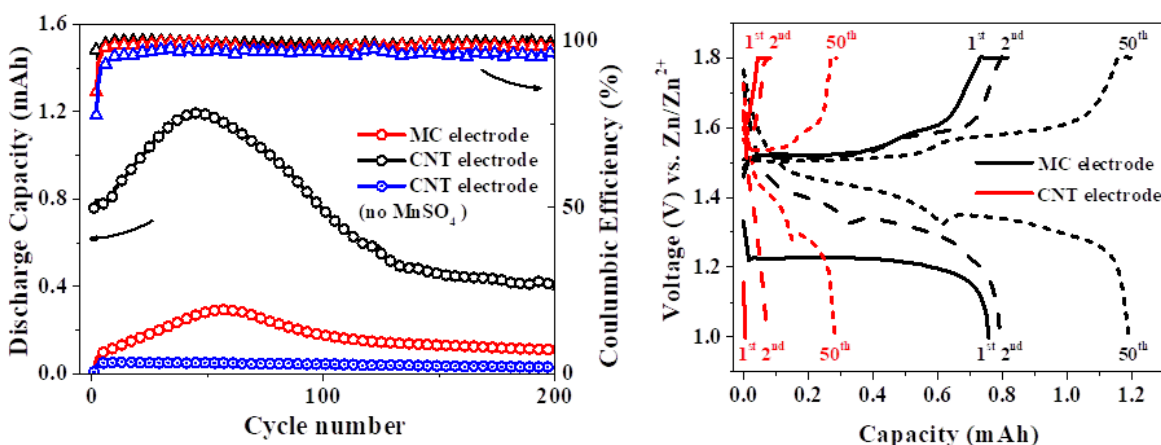


Figure 3.8 a) Discharge capacity profiles and b) Galvanostatic charge/discharge curves at 1st, 2nd and 50th cycles of MC and CNT electrodes.

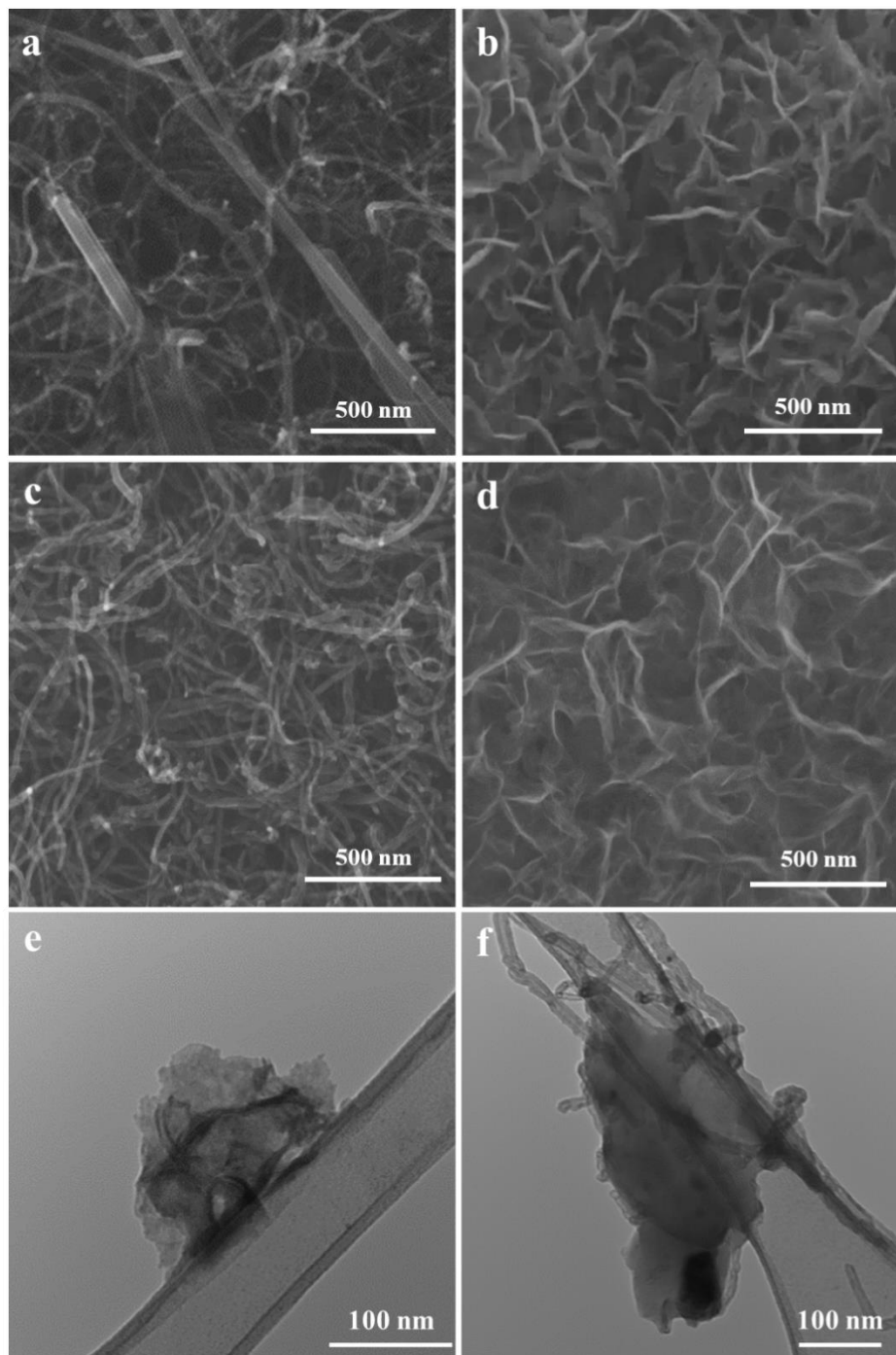


Figure 3.9 a) SEM image of the surface of the MC electrode before and b) after cycling, c) SEM image of the surface of the MC electrode before and d) after cycling, e) TEM images of MnO_x nanosheets from MC and f) CNT electrodes.

Figure 3.9a, 3.9b are SEM images of the as-prepared and cycled MC electrode surface, and the SEM images of the CNT electrode surface before and after cycles of charge and discharge are displayed in **Figure 3.9c** and **3.9d**. In the images of the as

prepared electrodes, the thin and curved strings are CNT, while the wider and straight rods are the α -MnO₂ nanorods. Just like the observation with standard electrodes, these two materials can no longer be observed on the electrode surface after cycling and are replaced by layers of MnO_x nanosheets. The dimensions of the nanosheets are further confirmed by TEM analyses to be around 100-200 nm (**Figure 3.9e** and **3.9f**). The consistent observations of the nanosheets across all three electrodes confirm the reproducibility of the Mn²⁺ electrodeposition phenomenon and suggest the electrodeposition is an independent reaction which will occur in the system regardless of the cathode material.

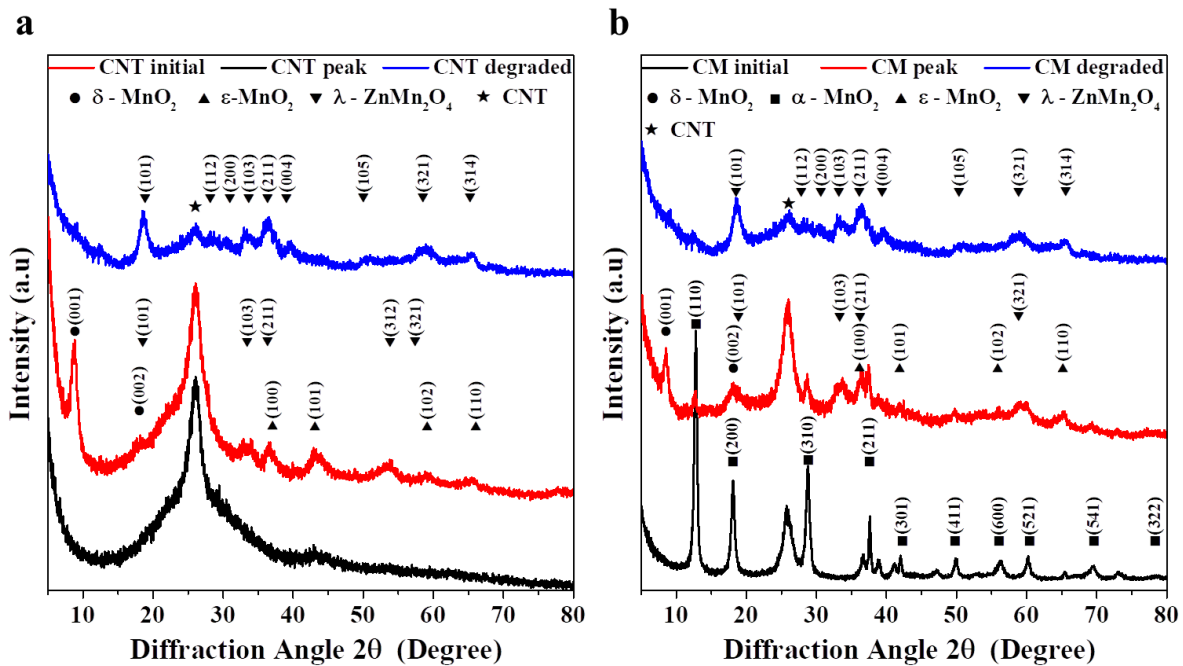


Figure 3.10 a) XRD spectra of CNT electrode and b) MC electrode at their initial, peak capacity and degraded states.

The XRD spectra of CNT and MC electrode at their initial, peak capacity and degraded states were also measured and the results are shown in **Figure 3.10**. As shown (**Figure 3.10a**), the CNT electrode initially only demonstrated the intrinsic carbon peak at 27°; but upon cycling to their peak capacity state, a complex polymorph system containing diffraction peaks associated with multiple MnO₂ crystalline phases were found. The system contains a strong peak of layered birnessite-MnO₂ (δ -MnO₂) (JCPDS 80-1098) found at 9°(001), weak diffractions of ϵ -MnO₂ (JCPDS 30-0820) at 37°(100), 42°(101), 56°(102) and 66°(110), and small peaks at 18°(101), 33°(103), 36°(211), 54°

(312) and 58° (321) that are often attributed to spinel ZnMn_2O_4 (λ - ZnMnO_2) (JCPDS 18-1484/77-0470). These MnO_2 crystalline phases have all been reported to participate in typical redox reaction of RMAZM batteries, confirming them as the cause of the capacity growth phenomenon.^{31,109,112} However, based on the result thus far, origin of each crystalline phases still cannot be stated with certainty, and further analyses of their transformation mechanism will be discussed in later chapter.

As the CNT electrodes are cycled to their degraded states, most of the above mentioned MnO_2 peaks can no longer be found; even the most distinct (001) diffraction of δ - MnO_2 at 9° is barely identifiable. The only remaining crystal phase is the λ - ZnMn_2O_4 with diffraction peaks at 18° (101), 28° (112), 33° (103), 36° (211), 38° (004), 51° (105), 58° (321) and 64° (314) that has been linked to performance degradation.¹¹⁰ λ - ZnMn_2O_4 is also known to be electrochemically inactive in alkaline condition and is a major contributor to capacity degradation in RAM batteries.⁹⁰⁻⁹² Its presence in a degraded CNT electrode would therefore be completely logical and provides a specific target for optimization plans following the investigation. It is noted that some studies did attempt to modify these spinel Mn species with defect engineering to boost their performance as cathode material in mildly acidic system, but their capacities are simply uncompetitive compare to other MnO_2 crystal phases.^{108,109}

In the XRD analysis of the MC electrode, similar results about the system were found (**Figure 3.10b**). Initially, the MC electrode clearly demonstrates the intrinsic diffraction peaks of α - MnO_2 and CNT. Upon cycling to its peak capacity, many of the weaker α - MnO_2 diffractions are erased; the stronger peaks such as (110), (200), (310) and (211) do remain, but experience significant intensity decline and widening. The diffraction of ε - MnO_2 , δ - MnO_2 and λ - ZnMn_2O_4 were found once again in the cycled cathode electrode and their location resemble with the ones found in the CNT electrode, evidencing their formation being an intrinsic trait of the RMAZM battery system. Finally, when the battery electrode is cycled to its end state, the diffractions of ε - MnO_2 and δ - MnO_2 disappeared and λ - ZnMn_2O_4 is again the only remnant found in the electrodes. The XRD spectra of the end-state MC and CNT electrode are strikingly similar, further confirming the negative influence of λ - ZnMn_2O_4 has on the battery performance. Given that MnSO_4 additive was used in the electrolyte, these results point to a fact that despite

successful suppression of the well-known Mn^{2+} dissolution issue, high rechargeability of the battery is still not guaranteed. Additional preventative measure should also be put in place to prevent the formation of electrochemically inactive side products.

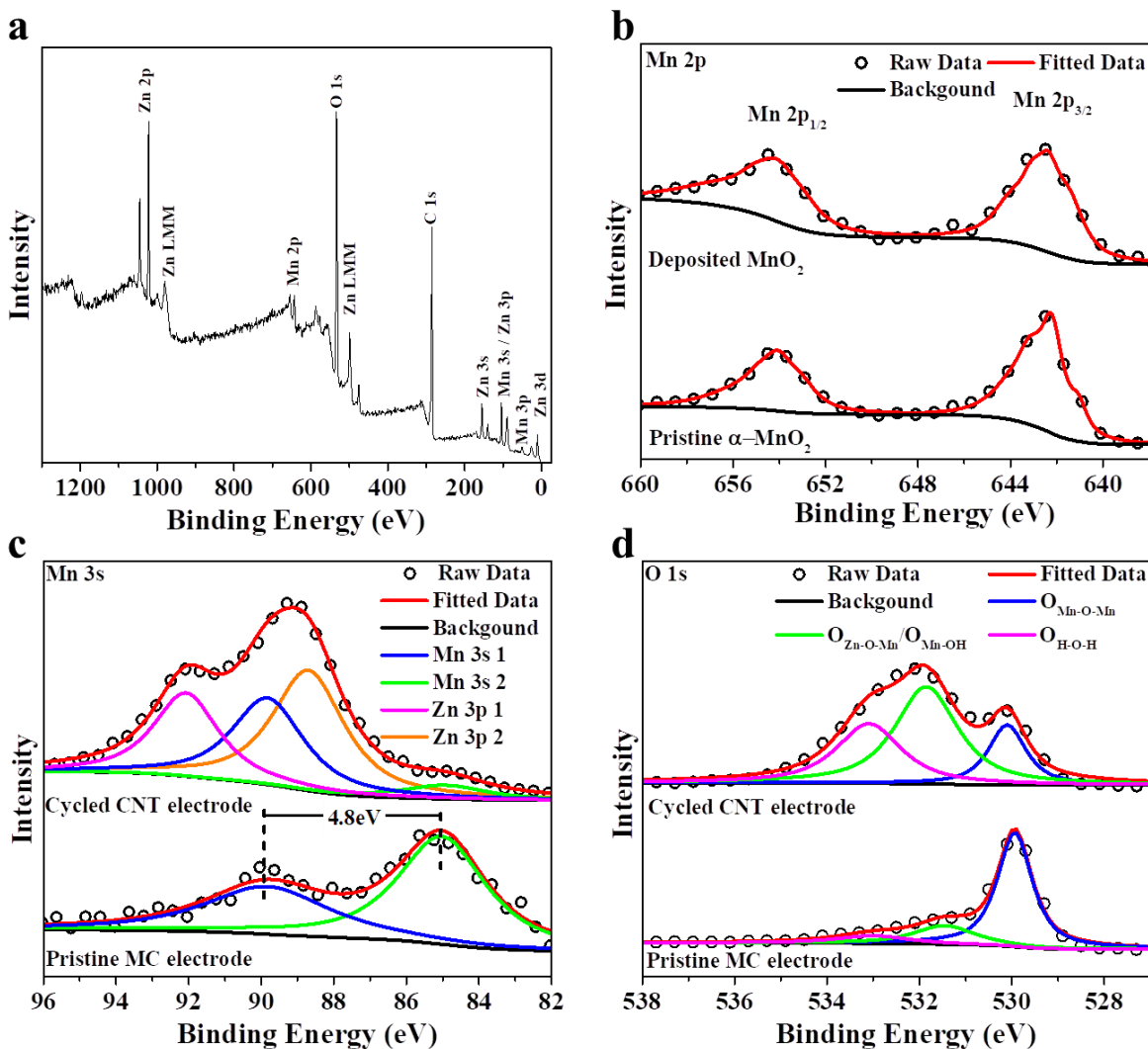


Figure 3.11 a) XPS scan survey of the cyclized CNT electrode b) Mn 2p c) Mn 3s and d) O1s spectra of the cyclized CNT and pristine MC electrode.

XPS analysis comparison of the electrodeposited MnO_2 and pristine $\alpha\text{-MnO}_2$ can also provide insights of the similarities and differences of the two crystal phases. **Figure 3.11a** is the XPS survey spectrum of the cyclized CNT electrode containing the electrodeposited MnO_2 at its charged state; signals from the elements of Zn, Mn, C and O can clearly be found in the spectrum. The presence of Zn adsorptions indicate the incomplete extraction of Zn from the MnO_2 crystal lattice during the charging process,

which can be link to the formation of the undesired λ - ZnMn_2O_4 ; it would also serves as another strong proof which would support that the MnO_2 do undergo Zn intercalation reaction. **Figure 3.11b** compares the Mn 2p of the electrodeposited MnO_2 with pristine α - MnO_2 , overall the location of the Mn 2p_{1/2} and Mn 2p_{3/2} are similar, but slight peak shape differences can be observed. The 2p adsorption of Mn is known for its complexity caused by multiple oxidation states having multiplet splitting that overlap,¹²² which often leads to misinterpretation and false assumption, thus no further data analysis is performed on these spectra.

Instead, the Mn 3s adsorptions (**Figure 3.11c**) are used to identify the oxidation states of the MnO_2 . In the Mn 3s spectra of pristine α - MnO_2 nanotubes, the two fitted peaks are separated by an energy interval of precisely 4.8eV, which indicates an oxidation state of 4+ and the chemical formula of MnO_2 .¹²³ For the electrodeposited MnO_2 , the Mn 3s spectra overlapped with the much more intense Zn 3p adsorption covered large portion of the target area, however, through data fittings, oxidation states of the Mn within the electrodeposited MnO_2 can still be identified to be within the range of 3+ to 4+. More information about the MnO_2 crystal structure can also be obtained from the O 1s spectra of the two cathode electrodes (**Figure 3.11d**). In the α - MnO_2 , lattice oxygen ($\text{O}_{\text{Mn-O-Mn}}$) is the large majorities of the adsorption, and only small amount of oxygen from oxyhydroxide defect ($\text{O}_{\text{Mn-OH}}$) and adsorbed/lattice water ($\text{O}_{\text{H}_2\text{O}}$) can be observed. In contrast, the O 1s spectra of the CNT with electrodeposited MnO_2 demonstrate a much higher $\text{O}_{\text{Mn-OH}}$ to $\text{O}_{\text{Mn-O-Mn}}$ ratio, suggesting high amount of oxygen defects in the crystal structure. High $\text{O}_{\text{H}_2\text{O}}$ content is also observed and these oxygens are likely from the lattice water that locates between the MnO_2 layers within δ - MnO_2 .

In this section, the capacity growing phenomenon observed in RMAZM batteries was confirmed to be a result of new active material generation from electrodeposition of the Mn^{2+} ion additives. The electrodeposited nanosheets layers found on the cycled CNT and MC electrodes were identified to be a Mn polymorph with high oxygen defect contents that consist of three types of MnO_2 , ϵ - MnO_2 , δ - MnO_2 and λ - ZnMn_2O_4 ; λ - ZnMn_2O_4 specifically is found to be the only remaining species in the end state electrodes, linking it tightly with performance degradation. Importantly, it was discovered that the crystal structure of α - MnO_2 is barely maintained over long period of low C-rate cycling

and the polymorph eventually becomes the major content in the cathode electrode. To resolve the performance degradation issue, one must then identify key mechanistic steps that may be of use to inhibit the undesired side reactions, and understand the origin and properties of each of the three MnO_2 species. In the following section, the crystal transformation of the pristine and electrodeposited Mn species will be investigated, compared and linked to explain the above observation; these will then serve as the foundation for drafting a degradation mechanism of MnO_2 in RMAZM batteries.

3.3.3 Transformation Mechanism of Pristine and Electrodeposited MnO_2

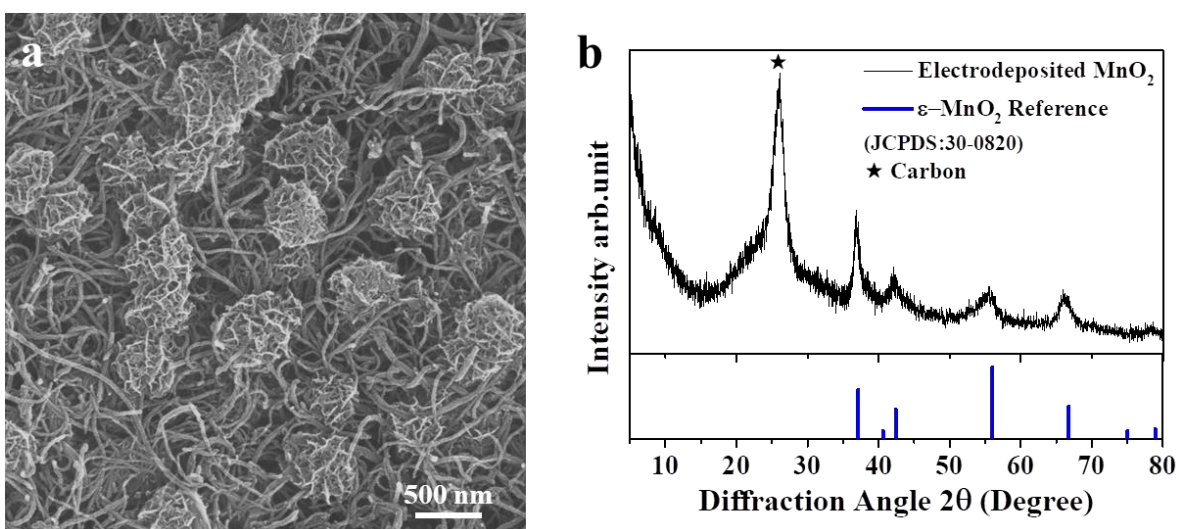


Figure 3.12 a) SEM image and b) XRD spectrum of MnO_2 electrodeposited onto the CNT electrode surface by 48 hrs of 1.8V constant voltage hold

To begin the analysis of the mechanistic investigation, a specific experiment, in which CNT electrodes were charged with a constant voltage hold at 1.8V for 48hrs, was performed to identify the initial crystal phase of the MnO_x that is electrodeposited onto the cathode electrode. **Figure 3.12a** is the SEM image of the pre-charged CNT electrode surface that shows agglomerated MnO_2 nanosheets grown onto the CNT surface. In its XRD spectrum (**Figure 3.12b**), four distinct diffraction patterns belonging to $\epsilon\text{-MnO}_2$ can be clearly observed, and the additional peak at 27° peak that is assigned to the CNT. These results suggest that $\epsilon\text{-MnO}_2$, a tunnel type MnO_2 that is the defected derivatives $\gamma\text{-MnO}_2$ with high degree of disorder, is the only crystal phase of MnO_2 that is in-situ electrodeposited in the specific environment during the cycling process within RMAZM batteries.¹¹²

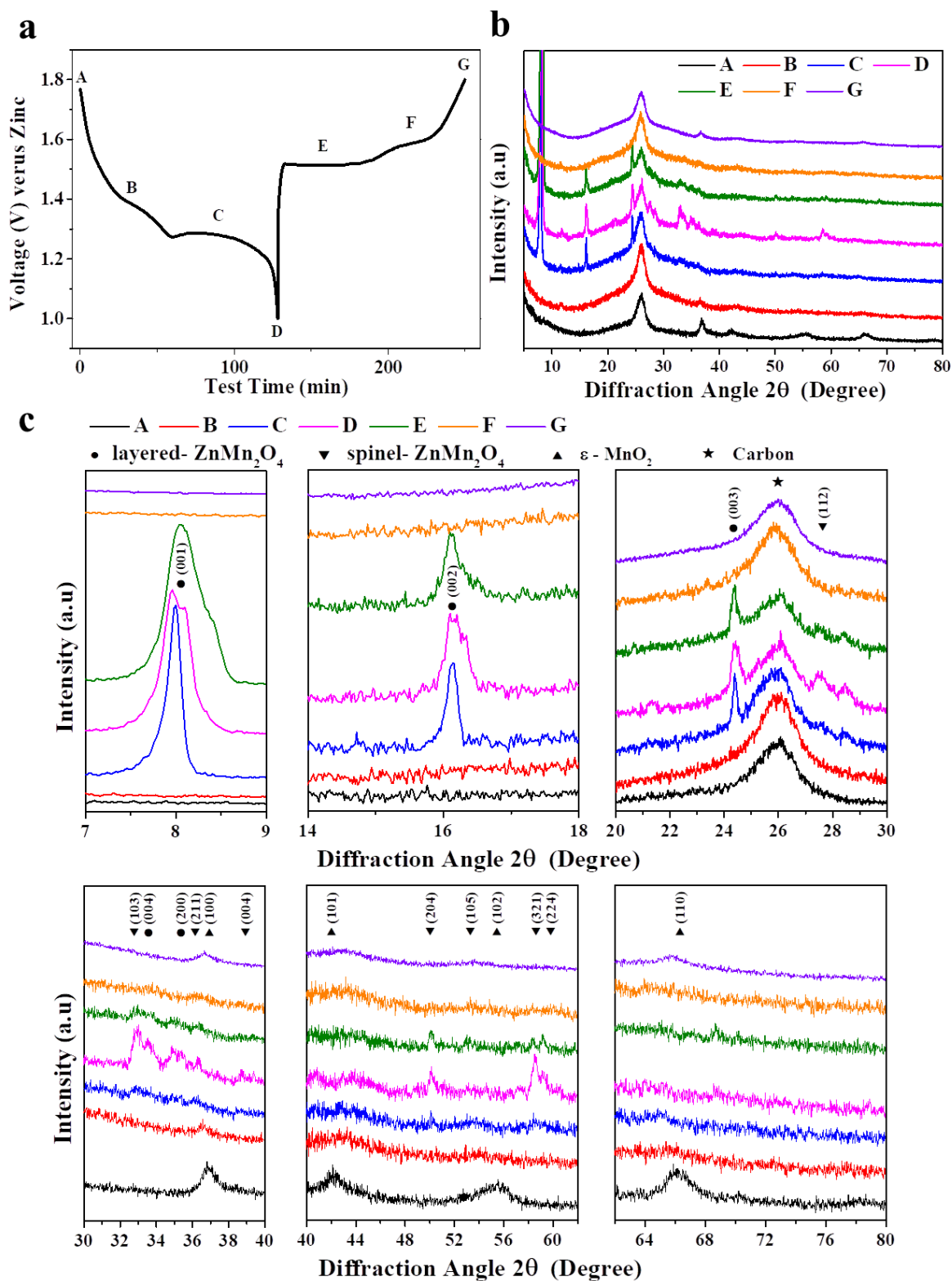


Figure 3.13 a) Galvanostatic charge/discharge voltage vs time curves and b, c) corresponding XRD patterns of the CNT electrode with electrodeposited $\epsilon\text{-MnO}_2$ at different state of charge and discharge.

After confirming the initial crystal state of the electrodeposited MnO_2 , further analyses on the CNT and MC electrode were performed to compare the short term transformation mechanism of the different MnO_2 . **Figure 3.13a** and **3.13b** are the voltage vs time curve of CNT electrode deposited with $\epsilon\text{-MnO}_2$ under Galvanostatic cycling and the corresponding ex-situ XRD spectra of the electrode at different electronic states. The XRD spectra are further divided into magnified sub-sections (**Figure 3.13c**) to allow thorough extraction of the results. As shown, in state A (as deposited), is the only type of MnO_2 that is present; the peak intensity was weakened in state B (discharged to 1.4V) but the overall crystal structure remains the same. At state C (discharged to 1.3V), three major peaks at 8.0° , 16.1° and 24.3° corresponding to the (001), (002) and (003) diffraction of birnessite- ZnMn_2O_4 ($\delta\text{-ZnMn}_2\text{O}_4$) (JCPDS 80-1098) emerge, evidencing the formation of the new species. In the meantime, signals that are assigned to the $\epsilon\text{-MnO}_2$ became barely detectable, suggesting the disappearance of the original crystal phase. Upon entering state D (discharged to 1.0V), on top of the consolidation of the $\delta\text{-ZnMn}_2\text{O}_4$ signals, diffractions related to $\lambda\text{-ZnMn}_2\text{O}_4$ such as the (112), (103), (211), (004), (204), (105), (321) and (224) found at 27.5° , 33.0° , 36.3° , 38.4° , 50.1° , 53.1° , 58.5° , and 59.3° have also appeared. The observation of the ZnMn_2O_4 species are not surprising as $\delta\text{-ZnMn}_2\text{O}_4$ is often regarded as the main discharged product of tunnel type MnO_2 ,^{31,111,124} whereas $\lambda\text{-ZnMn}_2\text{O}_4$ is also reported previously as discharge product of $\gamma\text{-MnO}_2$ and layered- MnO_2 and has been linked to irreversibility.^{110,125}

The crystal structure transformation is more or less reversed when the battery is charged. In state E (recharged to 1.5V), when the cathode electrode is recharged to 10-20% of its capacity, the intensity of peaks associated with $\lambda\text{-ZnMn}_2\text{O}_4$ is significantly weakened, signaling their slow disappearance through extraction of Zn ions from the crystal lattice. In the meantime, there are no major changes to the intensity of the $\delta\text{-ZnMn}_2\text{O}_4$ peaks, but significant shifts toward higher diffraction angle are observed, which indicates the narrowing of crystal interlayer spacing caused by Zn ion extraction. Upon charging to state F (recharged to 1.6V), majority of the aforementioned $\text{MnO}_2/\text{ZnMn}_2\text{O}_4$ peaks are barely identifiable, and at state G (recharged to 1.8V), weakened signals of $\epsilon\text{-MnO}_2$ re-emerge with unparalleled intensity, as the peaks at 37° and 66° show relatively stronger intensity, which would indicate the formation of

amorphous MnO_2 . The results likely suggest weak structural integrity of the electrodeposited $\epsilon\text{-MnO}_2$ as one cycle of charge and discharge significantly change its XRD spectrum, which would influence its reversibility in long term cycling.

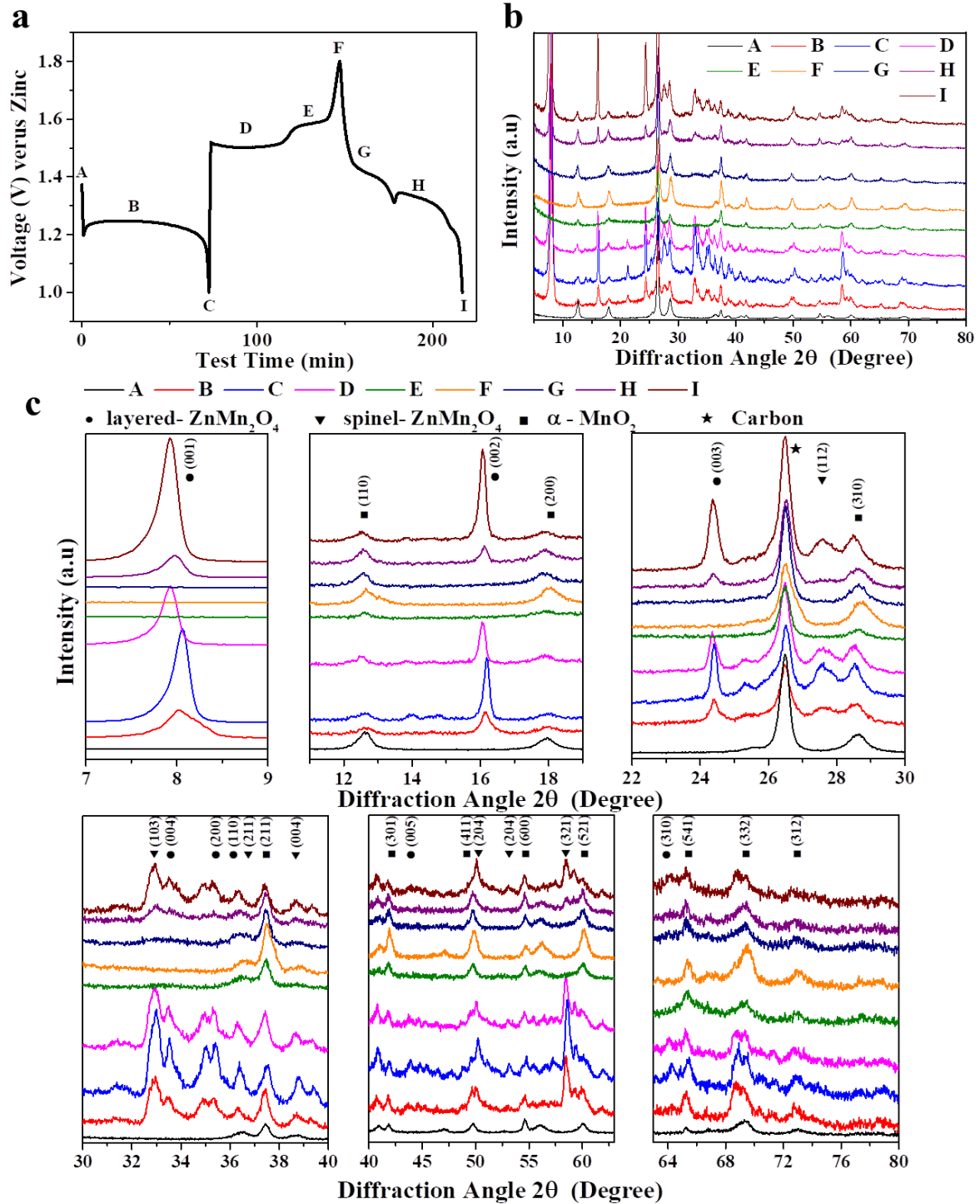


Figure 3.14 a) Galvanostatic charge/discharge voltage vs time curves and b, c) corresponding XRD patterns of the $\alpha\text{-MnO}_2$ MC electrode at different state of charge and discharge.

MC electrodes prepared with α -MnO₂ were also examined by ex-situ XRD in a similar manner (**Figure 3.14a, 3.14b** and **3.14c**) for comparison purposes, and some important information about the system was obtained. Starting from the first discharge, diffractions associated with δ -ZnMn₂O₄ and λ -ZnMn₂O₄ were found early in the process at state B (discharged to ~90% capacity) and further strengthen in state C (discharged to 1.0V). Unlike the scenario with electrodeposited ε -MnO₂ though, there is no distinct variation between their intervals of appearance. Also during this period, the peaks of α -MnO₂ were significantly weakened, but never completely removed, which likely indicates the introduction of defects within their crystal lattice. When the battery is recharged through state D (recharged to 1.5V), state E (recharged to 1.6V) and state F (recharged to 1.8V), the intensity of these α -MnO₂ peaks was largely recovered to its original status, evidencing a high reversibility of the crystal lattice toward discharge and charge. Though, shifts toward higher angles were observed with these peaks, which reflects the narrowing of interlayer spacing and crystal tunnel sizes caused by the extraction of K⁺ ions originally reside within the tunnels. In the meantime, while diffractions of δ -ZnMn₂O₄ and λ -ZnMn₂O₄ are still detectable at state D, they can no longer be observed in state E and F, confirming their complete disappearance from the system when the battery is recharged either by returning to α -MnO₂ or through formation of amorphous MnO₂.

In the second discharge, multiple differences are found in the transformation process of the MnO₂ crystals accompany by a different discharge curve. To start, through the interval of state F to state G (discharged to 1.5V) and Stage H (discharged to 1.3V), aside from the intensity reduction, the α -MnO₂ diffraction also experience shift toward lower angle. This behavior can be explained by either zinc intercalation that expands the crystal tunnel/interlayer spacing or conversion (or H⁺ intercalation) reaction that convert proportion of the oxide to oxyhydroxide without changing the overall crystal structure. Given that a previous study has reported fast kinetic and independency on Zn ions of the discharge plateau between 1.8V to 1.3V,¹¹² there is a higher possibility for the latter of the two reaction to be the correct answer. The occurrence of the α -MnO₂ peak shifting toward lower angle would end in state H, in which the diffractions of δ -ZnMn₂O₄ and λ -ZnMn₂O₄ begin to re-emerge, and strengthen as the battery reaches state I (discharged to 1.0V). Comparing to the first discharge, the appearance of these two ZnMn₂O₄ phases in

the second discharge are significantly delayed and only occurred in the latter half of the process, which implies a change in the discharge reaction. This claim is also supported by the distinct time segregation between the occurrence of the α - MnO_2 peak shifting and the re-emergence of the two ZnMn_2O_4 . It is worth to mention that the effects of pre-charging the RMAZM battery to 1.8V prior to the first discharge was also investigate, and the results show that it does not cause meaningful variation aside from adding a highly sloped discharge curve with very small amount of capacity between 1.8V to 1.25V. This would further confirm that the new plateau at 1.35V-1.45V in the second discharge is a direct result of the crystal lattice modification the α - MnO_2 experience during the first discharge.

The above analysis on the short term transformation of the ε - MnO_2 and α - MnO_2 also provided extra details and answers to some of the questions left on the XRD spectra of the electrodes after long term cycling (Figure 3.10). First, of the three Mn species within the MnO_2 polymorphs found on the CNT electrode at their peak capacity state, only ε - MnO_2 is directly electrodeposited. Its limited reversibility when cycled to δ - ZnMn_2O_4 or λ - ZnMn_2O_4 during discharge and charge would explain their slow conversion to the layer type δ - MnO_2 and spinel type λ - ZnMn_2O_4 . Moreover, of the two ZnMn_2O_4 crystal phases, δ - ZnMn_2O_4 is likely the initial discharge product given their earlier occurrence, but it can be converted to λ - ZnMn_2O_4 when further discharge; the reversibility of this step should also be limited as well, given the observation of λ - ZnMn_2O_4 as the sole remaining crystal in the end state electrode. The long term transformation mechanism of the ε - MnO_2 would then be, first to δ - MnO_2 and then eventually to λ - ZnMn_2O_4 that is electrochemically passive.

As for the MC electrode, while δ - ZnMn_2O_4 and λ - ZnMn_2O_4 are found to be unavoidable species that will form when α - MnO_2 is discharged, it was also discovered that they are return to their original form when charged. The δ - MnO_2 and λ - ZnMn_2O_4 observed in the cycled MC electrode would therefore more likely be resultants of the ε - MnO_2 after it is electrodeposited and underwent the cycling process. As previously mentioned, the MnO_2 electrodeposition process consumes the limited Mn^{2+} ions within the electrolyte; the eventual depletion of the Mn^{2+} ions would mean the alleviation of their protection that prevents the dissolution and consequently performance degradation

of the main active cathode material. Overtime, all of the original α -MnO₂ would slowly deteriorate through dissolution and then re-deposited in the form of ε -MnO₂, follow by transform to δ -MnO₂, and eventually to λ -ZnMn₂O₄.

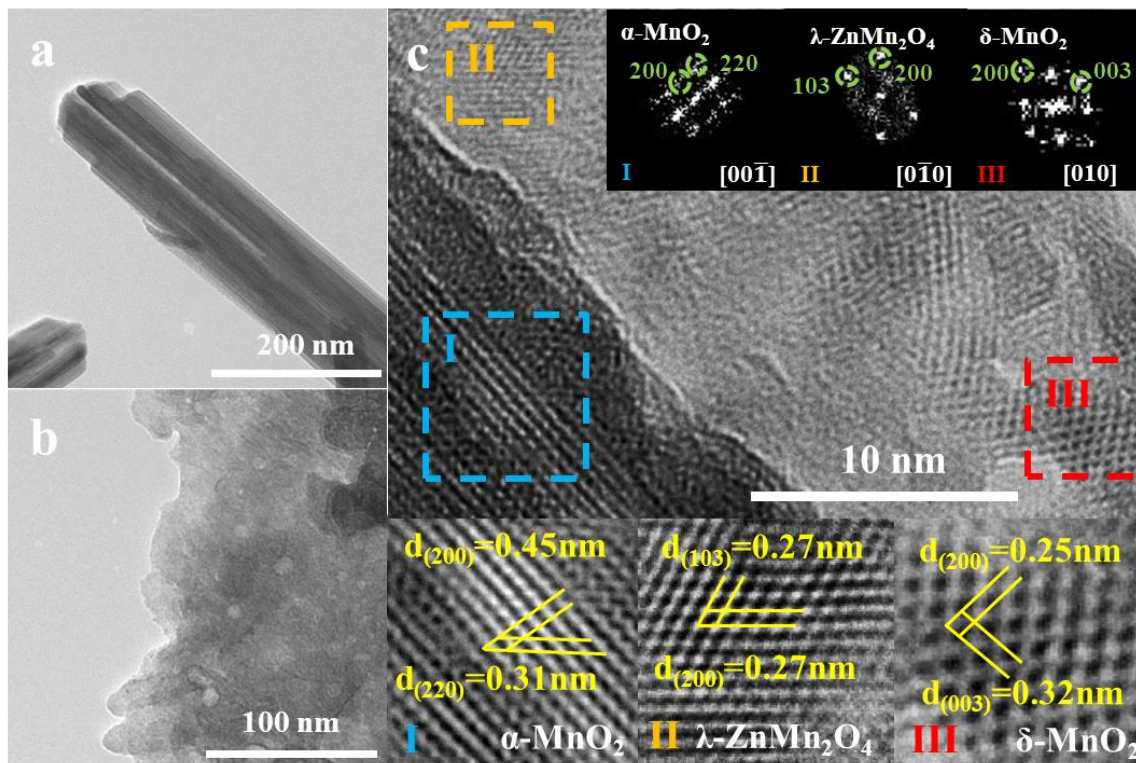


Figure 3.15 The HRTEM images of a) α -MnO₂ nanorod, b) electrodeposited MnO₂ nanosheets and c) intersection of a nanorod and nearby nanosheets. The inset images are the FFT and Inverse FFT of the selected areas.

The above claim about the transformation process is further supported by high resolution TEM (HRTEM) images of MC electrodes at their charged state that undergone around 50 cycles of Galvanostatic discharge and charge (Figure 3.15). Figure 3.15a and Figure 3.15b are HRTEM images of the α -MnO₂ nanorod and the MnO₂ polymorph nanosheets. As shown, the α -MnO₂ nanorod demonstrate long range periodic ordering that span over its entire structure, whereas the nanosheets are divided into areas that either have amorphous properties or contain small area of crystal fringes that are isolated, further confirming the disordered structure of these materials. Figure 3.15c shows the HRTEM image of an intersection of a nanorod and nearby nanosheets in a cycled MC electrode. Three areas of distinctly different crystal structure can be found. Enclosed within Area I is the crystal fringes of the cycled α -MnO₂ nanorod, fast Fourier transform

(FFT) pattern of this area can be indexed to the [001] zone axis of a typical tetragonal species and the inverse FFT (IFFT) image also clearly shows the typical α -MnO₂ [200] and [220] lattice fringes with d-spacing of 0.45 nm and 0.31 nm, respectively, reassuring that the crystal structure of the α -MnO₂ nanorod is still maintained after 50 cycles Galvanostatic cycling. Area II and Area III are two separated regions of the cycled electrodeposited MnO₂ polymorphs that demonstrate distinctly different FFT patterns which could be indexed to the [010] zone axis of tetragonal λ -ZnMn₂O₄ and [010] zone axis of monoclinic δ -MnO₂, respectively. IFFT image of area II shows two sets of crystal lattice fringes, each with interlayer d-spacing of \sim 0.27 nm, that form a \sim 60° angle, and they can be attributed to the [103] and [200] facets of λ -ZnMn₂O₄. In comparison, the intersecting lattice fringes found in the IFFT image of area III demonstrate interlayer d-spacing of 0.25 nm and 0.32 nm, forming an angle of \sim 79 degrees. They can be assigned to the [200] and [003] diffractions of δ -MnO₂. Overall, the HRTEM analysis of the cycled electrodes further confirm the hypothesis that undesired consumption of Mn²⁺ ions by ϵ -MnO₂ electrodeposition and eventual formation of electrochemically inactive λ -ZnMn₂O₄ through such transformation route is the main cause of performance degradation in RMAZM batteries that used Mn ion additives.

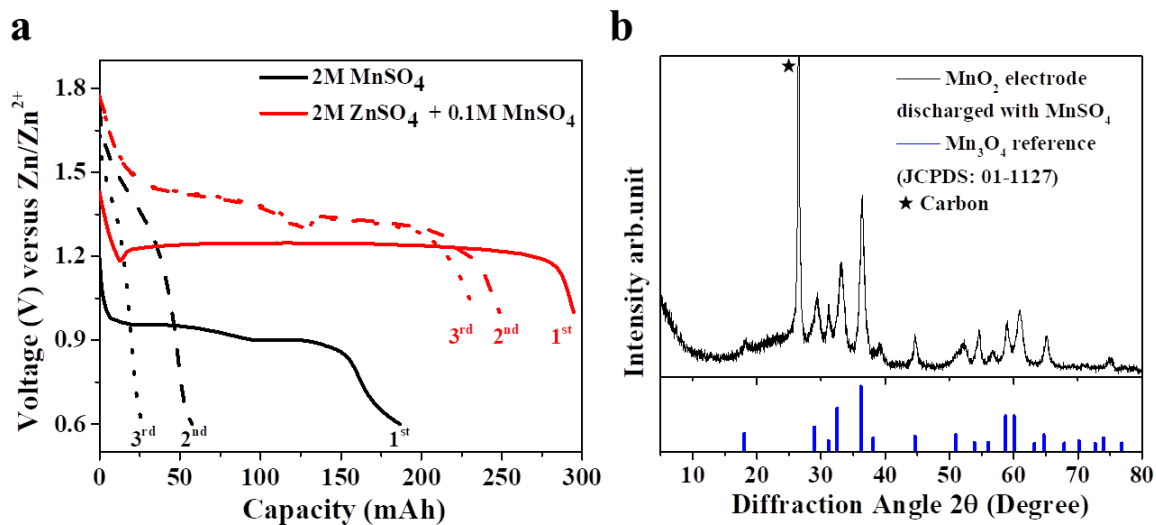


Figure 3.16 a) 1st, 2nd and 3rd Galvanostatic discharge curves of RMAZM batteries using 2M MnSO₄ or 2M ZnSO₄ + 0.1M MnSO₄ electrolyte. b) XRD diffraction patterns of MC electrode in RMAZM batteries discharged to 1.0V with 2M MnSO₄

For curiosity purposes, an additional experiment was conducted to probe the electrochemical reaction of α -MnO₂ without Zn ions by changing the electrolyte from 2M

ZnSO₄ + 0.1M MnSO₄ to 2M MnSO₄. Interestingly, the battery discharge curves changed completely (**Figure 3.16a**), in which the first discharge curve shows a plateau that span over 0.90V to 0.95V; discharge curves of the following cycles are all sharply sloped and the capacity would quickly fade below 20% of the starting values. This result contradict entirely with a previously publish study about the behavior of electrodeposited ε-MnO₂, whose discharge plateau with 1M MnSO₄ electrolyte is largely equivalent to the 1.4V plateau assigned to the conversion reaction observed in RMAZM batteries using 2M ZnSO₄ + 0.1M MnSO₄.¹¹² Post discharged XRD analysis of the MC electrode indicates that spinel Mn₃O₄ (JCPDS: 01-1127) and carbon are the only remaining species. This difference in behavior may be explained by the absence of defects in the highly crystalline α-MnO₂ that would occur much more frequently in as-deposited ε-MnO₂. The result would also suggest that Zn intercalation must be the only reaction in the first discharge, the defect installed to the crystal structure during this process must then be what allows the conversion reaction to occur.

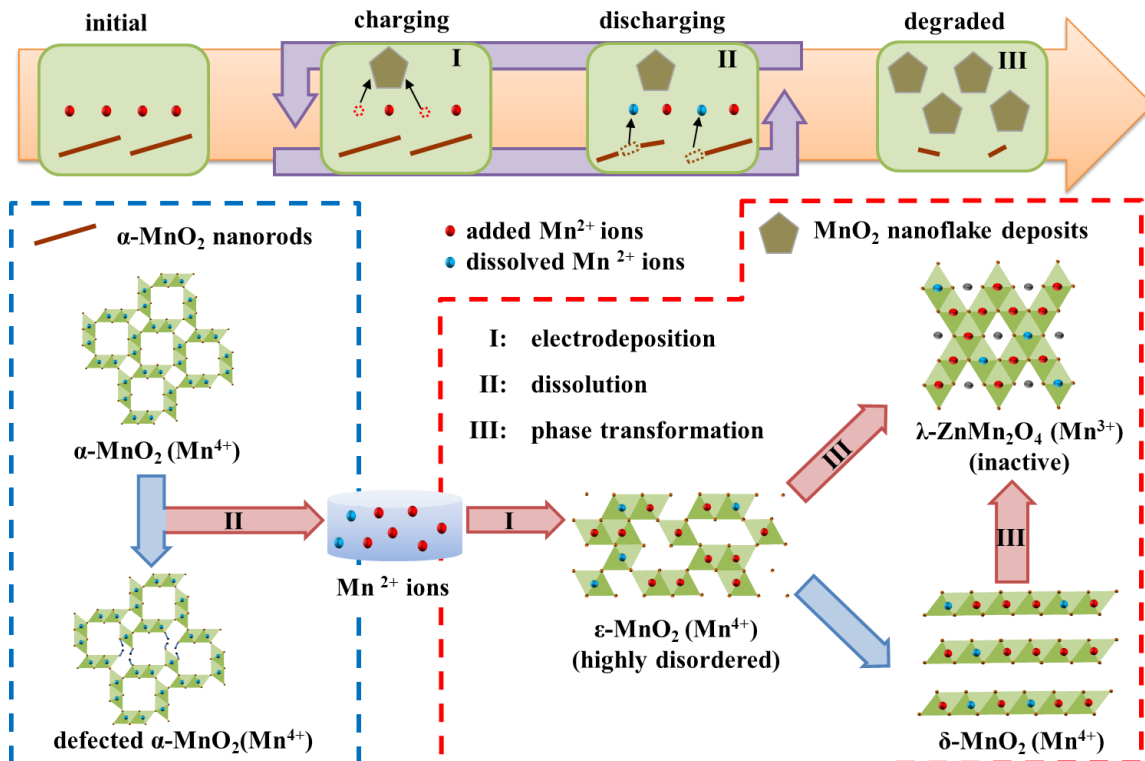


Figure 3.17 Schematic illustration of the long term crystal transformation of α-MnO₂ within RMAZM batteries that adapted Mn ion additives.

Summing all of the mechanism investigation results, a long term transformation process of MnO₂ species within RMAZM batteries is summarized and demonstrated in **Figure 3.17**. As illustrated, the main reason of performance degradation in these batteries is the eventual conversion of all Mn species (α -MnO₂ and Mn²⁺ additives) to the electrochemical passive λ -ZnMn₂O₄. The conversion path consist of three major individual steps, which include I) uncontrolled MnO₂ electrodeposition that slowly consumes the Mn additives in the electrolyte, II) dissolution/disproportion reaction of the primary cathode material (α -MnO₂) following the depletion of Mn additives and III) the transformation of the electrodeposited Mn species to λ -ZnMn₂O₄. It is worth noting that the formation of δ -MnO₂ is not considered a problem due to its moderate capability as an intercalation-type cathode material.³¹ However, their transformation to λ -ZnMn₂O₄ reported by previous study and confirmed by the experimental results would still be problematic.¹¹⁰

Of the three steps above, the MnO₂ electrodeposition (Step I) is the main trigger of the entire degradation process, it is the main driving force that pushes steps II and III to occurs and the deterioration to proceed. Although previous studies did associated some benefits to this phenomenon in lab scale batteries,^{31,108} these advantages are likely not feasible in commercial products as standard batteries generally minimize electrolyte amount to increase battery energy density. More importantly, its effects in causing imbalance in the electrolyte system and formation of electrochemically inactive species are far too disruptive for the battery rechargeability. With this in mind, the non-stop electrodeposition of Mn²⁺ ion should be re-identified as a major gateway that opens up a path for performance degradation, and its inhibition or partial suppression should be relabelled as a priority when optimizing different components of RMAZM batteries.

4 Suppressing Manganese Dioxide Deposition with Expanded Graphite for High Performance Zn-MnO₂ Batteries

4.1 Introduction

In the last chapter, the reaction transformation mechanism of MnO₂ and the issues arising from the in-situ MnO₂ deposition phenomenon are systematically investigated and discussed. It was discovered that although the electrodeposited MnO₂ do provide temporary extra capacity, it also adds a reaction path for generation of undesired species that are threats to the RMAZM batteries long term stability. Previous studies have focused heavily on the effect of Mn additive in ensuring the integrity of the active cathode material, but rarely considered the longevity of the Mn additives themselves. As a result, the low C-rate stability of RMAZM batteries is often inferior comparing to their high C-rate performance, in which MnO₂ electrodeposition is hindered kinetically.

In this chapter, the focus would be to adapt the obtained findings into designing a MnO₂ cathode electrode that is capable of suppressing by-product formation while maintaining the excellent high C-rate performance. Specifically, kinetics of the MnO₂ electrodeposition reaction is explored and manipulated to achieve the desired result. Expanded graphite (EG) prepared from thermal shock expansion of sulfuric acid intercalated graphite (expandable graphite) is discovered as a substrate material that is capable of suppressing the MnO₂ electrodeposition rate without negatively impacting the electrochemical performance. The resulting optimized cathode electrode demonstrate a much improved cycle life in low C-rate cycling, maintaining a capacity of over 250 mAh g⁻¹ after 300 cycles of Galvanostatic charge and discharge at 1C. At the same time, the electrodes also demonstrated good stability when cycled at 5C, achieving 1500 cycles of discharge with capacity near 200 mAh g⁻¹. Finally, due to the absence of polymer binder from the electrode, the design strategy also improved the rate performance of the MnO₂ electrode, allowing it to be among the best performing MnO₂ based electrodes reported in research publications.

4.2 Experiment Procedures

4.2.1 Preparation of Expanded Graphite

Two approaches have been attempted to prepared expanded graphite, the first method is the microwave irradiation in a conventional microwave oven and the other is through thermal shock in a furnace tube oven. In the microwave irradiation method, 0.1 g of expandable graphite purchased from Sigma Aldrich was microwaved in a Danby microwave at 800 mW for three separate periods of 10 seconds. During this process, the expandable graphite would slowly heat up until a threshold is reach when it rapidly increases in volume. The rapid expansion generally occurs within a period of 2 to 3 seconds and it is accompanied by generation of sparks. Upon the rapid volume expansion, the expanded graphite would continue to spark until the microwaving process is completed. The final EG has a worm-like structure and a black color. The length of the expanded graphite may vary from 0.3 cm to 0.7 cm. The microwave apparatus was located within a fume hood to ensure no undesired gas is release into the laboratory. After each microwave period, the beaker was rested for 30 s to 1 min to dissipate accumulated heat.

For the thermal shock expansion method, 0.1 g of expandable graphite was first placed within a quartz glass tube that has one end sealed. Then they were transfer into a long furnace tube, which was then fill with argon gas and preheated to 900 °C within 45 minutes. During this process the quartz tube holding the expandable graphite was kept outside of the furnace at room temperature. When the programmed temperature of 900 °C is reached, the quart tube was slide into the center of the furnace to experience the thermal shock. The expandable graphite was kept in the furnace for 1, 10, 30 or 60 mins, and was moved back out to cool in room temperature when the time is reached. Within the first minute of the treatment, the graphite would be expanded and the small amount of white smoke is observed. The thermal shock expanded graphite does not exhibit any noticeable appearance difference in comparison to the samples prepared by microwave.

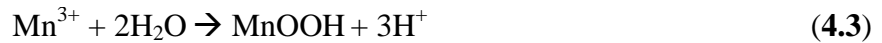
4.2.2 Preparation of Polymer-free Manganese Dioxide/Expanded Graphite/Carbon Nanotube Electrode

First, α -MnO₂ nanorods, EG and Carboxylate activated carbon nanotubes were mixed in 40 mL of EtOH with a weight ratio of 75:20:5. The dispersion is then sonicated for at least 3 hrs in a seal beaker. After the sonication, the dispersion is filter onto a glass fiber (VWR, Glass Microfibre Filter 691). After the filtration is completed, the electrode was left to dry on the filter under vacuum to ensure compactness of the materials. The radius of the filtered cathode electrode can either be 0.8 cm² or 1.75 cm² and the MnO₂ loading is around 1.5gcm⁻². Prior to installation into the battery, the electrodes were pressurized within a sealed syringe to a pressure of approximately 5 atm to ensure proper contact between each component.

4.3 Results and Discussions

4.3.1 Adaptation of Expanded Graphite and Optimization of Cathode Electrode for High Performance Zn-MnO₂ Batteries

The electrodeposition of MnO₂ from Mn²⁺ ion electrolysis is a well understood reaction that are widely adapted in the industrial and academic community.⁴¹ Under standard condition, the reaction would occurred at a potential of 1.9858V versus Zn/Zn²⁺, but in the slightly acidic environment (pH = ~4) within 2M ZnSO₄ electrolyte, the potential will be lowered to 1.53V versus Zn/Zn²⁺ (**Appendix 6.1**), a level that is well within the operation window of RMAZM batteries.



The MnO₂ electrodeposition reaction in mildly acidic condition has four elementary steps, starting with the adsorption of dissolved Mn²⁺ ions on to the electrode surface (**Equation 4.1**). Then the adsorbed Mn²⁺ ions are oxidized to Mn³⁺ (**Equation 4.2**), which quickly react with neighboring water molecules to form manganese oxyhydroxide (MnOOH) anchored on the electrode surface (**Equation 4.3**). Finally, the

MnOOH would be further hydrolyzed to form amorphous or defected crystalline MnO₂ (Equation 4.4).⁴¹ Among the four steps, Mn adsorption to the electrode surface is the rate determining step of the entire process, any restrictions placed on this bottleneck step will effectively hinder the overall reaction; it is therefore a specific target that one would aim at to inhibit the undesired electrodeposition of MnO₂.

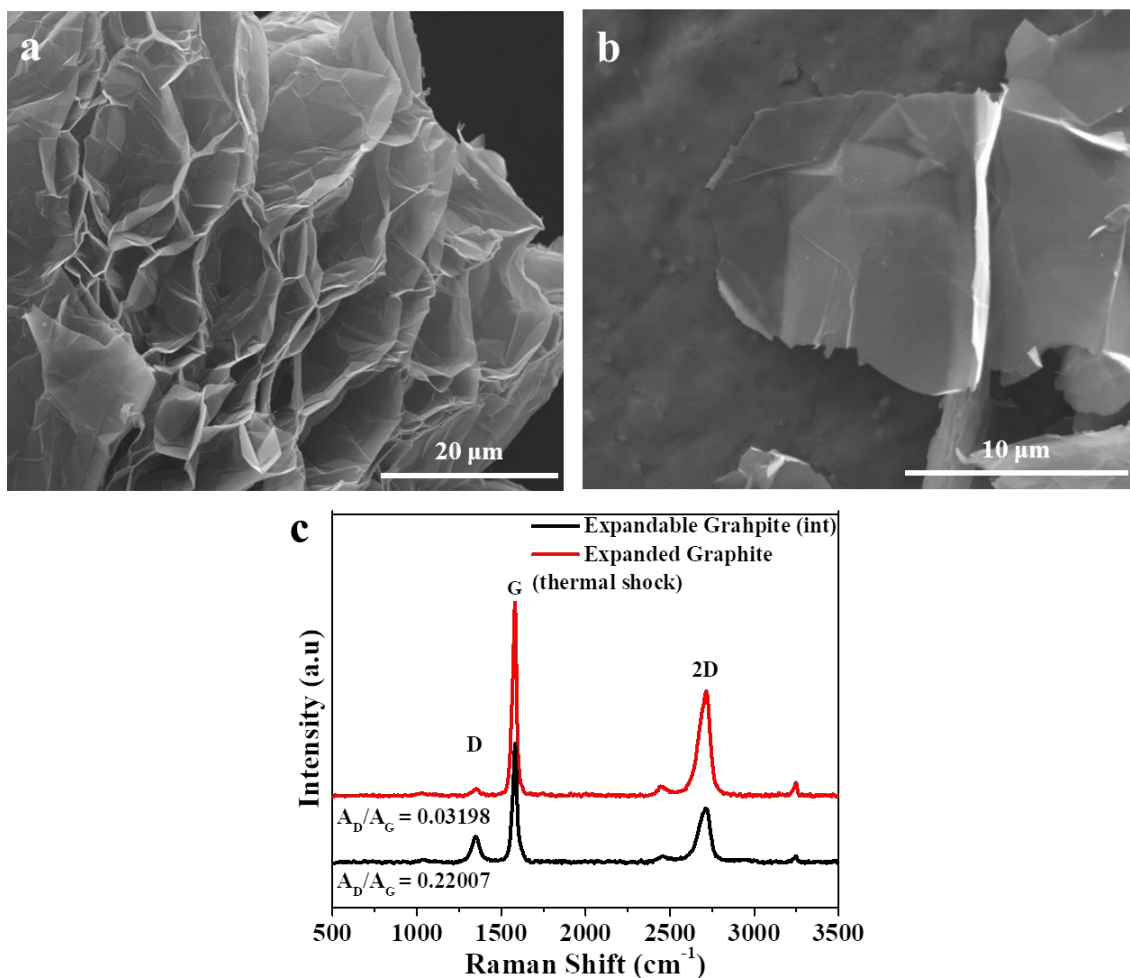


Figure 4.1 SEM images of the a) as-prepared and b) sonicated thermal shock expanded graphite. c) Raman spectra of the expandable graphite and thermal shock expanded graphite.

To this end, expanded graphite (EG), a type of carbon-based material prepared from abundant graphite flakes is discovered to demonstrate properties that may aid the aforementioned target of preventing Mn adsorption. They are hydrophobic, highly electrically conductive, relatively durable in mildly acidic environment, capable of forming thin film without binders and have sufficiently high surface area,¹²⁶⁻¹²⁸ making them an ideal cathode electrode substrate material for hosting α -MnO₂ nanorods. A

typical method of preparing EG is by first mixing the graphite flakes with an intercalation agent, and then subjected the dried graphite flakes to a thermal shock either in the form of microwave heating or short periods of high temperature furnace heating. During the thermal shock, the intercalated agent within the carbon layers would experience fast vaporization, generating large air pressure that exfoliates the carbon layers apart, drastically expanding the volume of the graphite flakes by 200 to 400 folds to form EG with a worm like structure.¹²⁶⁻¹²⁸

Figure 4.1a is the SEM image of the as-prepared EG which shows the exfoliated layer structure; the volume between each layer varies from 0.5 to 10 μm and the layers are still partially attached to each other. Each of the graphite layers in EG can be further broken apart through sonication in ethanol, and the resulting graphite micro platelet is shown in **Figure 4.1b** with dimensions of approximately 10 μm x 10 μm . **Figure 4.1c** is the Raman spectra of the expandable graphite before and after thermal shock treatment. While intrinsic D, G and 2D adsorption of carbon observed in both samples, the A_D/A_G ratio of EG (0.032) is significantly lower in comparison to that of the intercalated graphite flakes ($A_D/A_G = 0.220$), indicating the reduced amount of defects within the carbon structure that would generally be associated with high hydrophobicity of the material.¹²⁸

The effect of EG in suppressing MnO_2 electrodeposition was first observed when it was mixed with $\alpha\text{-MnO}_2$ to form a polymer-free thin film electrode (ME electrode). As shown in **Figure 4.2a**, the addition of EG did not substantially influence the Galvanostatic charge and discharge curve of the $\alpha\text{-MnO}_2$, which exhibit the same plateaus as cathode electrodes demonstrated previously. Though, noteworthy changes can be observed in their cycling results (**Figure 4.2b**), for one, the electrode experience fast capacity decay within the first 30 cycles likely caused by detachment of active materials. More importantly, the specific capacity would then be maintained at values near 150 mAh g^{-1} for over 100 cycles without significant growth nor decay. This different behavior is attributed to the high hydrophobicity of the EG substrate which forms an inhibiting layer that reduce Mn^{2+} ion adsorption and thus suppress the capacity growing phenomenon. Their smooth surface may also be another factor, as it provides lesser anchoring point for the deposits. The above hypothesis was further confirmed with the

galvanostatic cycling of a pure EG electrode, which displayed a capacity growing rate that is only one eighth of the one of the pure CNT electrode (**Figure 4.2c**).

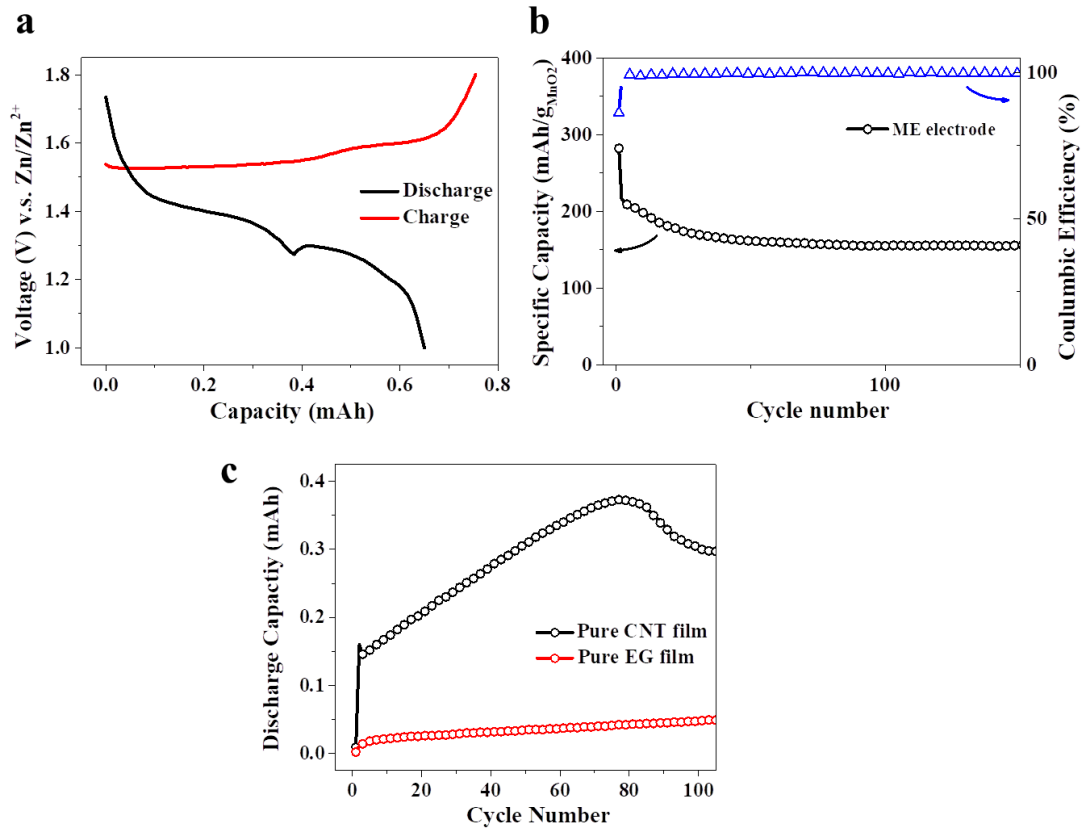


Figure 4.2 a) Standard Galvanostatic charge and discharge curves and b) specific capacity profile of ME electrode. c) Discharge capacity profiles of pure CNT and EG electrodes

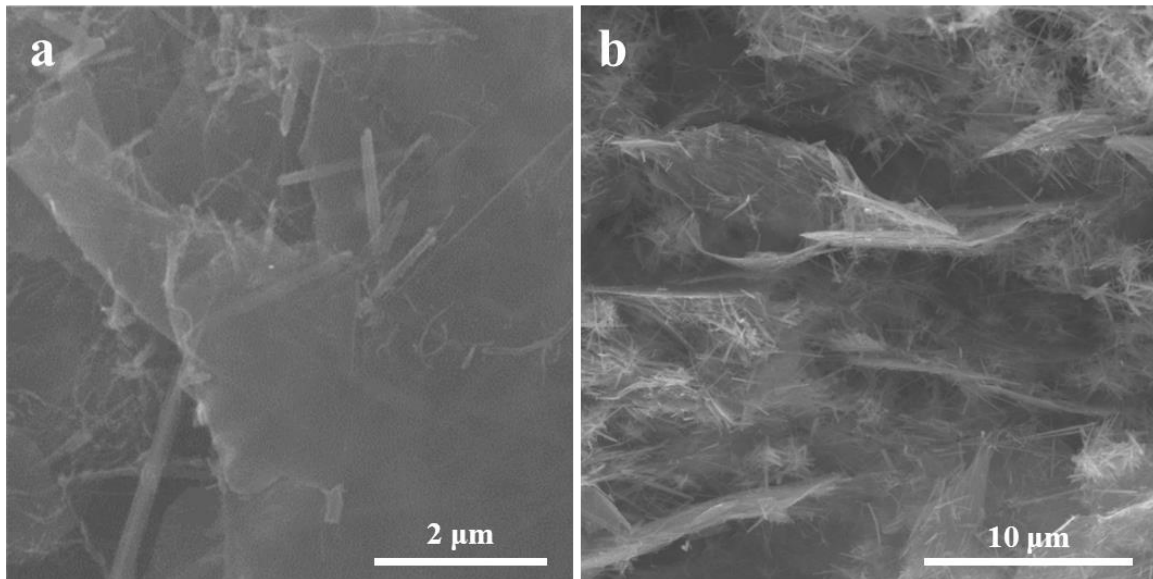


Figure 4.3 a) Surface and b) cross section SEM images of the MEC electrode

To avoid the active material detachment issue and further optimize the electrode design, CNT is added as a conductive pseudo-binder additive that would serve to anchor the α -MnO₂ nanorods onto the EG surfaces by providing additional binding site to both components. The weight composition of the final electrodes was chosen to be 75% α -MnO₂, 20 wt % EG and 5 wt % CNT; these electrodes will be referred as the MEC electrodes in the following discussion. **Figure 4.3a** is the SEM image of the MEC electrode surface and all three of the electrode components can easily be observed; the thin sheets being the EG, the straight rods with lengths between 0.5-5 μ m are the α -MnO₂ and the curled short strings with length less than 1 μ m are the CNT. The image clearly shows that some of the α -MnO₂ and CNT are positioned between the EG layer and that they are entangled with each other. SEM cross-section image of the MEC electrode displayed in **Figure 4.3b** would further confirm the components placement, as it evidently shows the intertwined α -MnO₂ and CNT siting within stacking layers of EG. Such positional orientation is important to allow proper functioning of the EG as the conductive network and inhibitor of MnO₂ electrodeposition.

Figure 4.4a is the CV scan of the RMAZM batteries assembled using the MEC electrode. It contains a reductive peak at 1.15V in the first cycles and two peaks at 1.29 V and 1.37 V in subsequent cycles. The oxidations peaks on the other hands were located at 1.57V and 1.62V all time. The result aligns well with all previous finding which confirm the proper functioning of the batteries with the new electrode design. The major advantage of the MEC electrodes though, is fully showcased in the 1C cycling performance comparison between the standard and MEC electrodes displayed in **Figure 4.4b**. In which, the active material within the MEC electrode maintained a specific capacity level of around 240 to 260 mAh g⁻¹ for 300 cycles of charge and discharge, and evidently, successfully contained the capacity growth phenomenon that would lead to eventual performance decay in the standard electrode. Indeed, standard electrode would possess higher capacity within the first hundred cycles due to the extra capacity contributed by the electrodeposited MnO₂, but it is important to remember that these extra capacities are not practically meaningful. Typical batteries that are feasible industrially would require the active material (cathode and anode) content to be maximized and minimizing contents that do not provide energy density. In such scenario,

the extra capacity contributed by Mn^{2+} ions from the limited amount of electrolyte would not be relevant, and that inhibiting MnO_2 electrodeposition would bring far more benefits than harm.

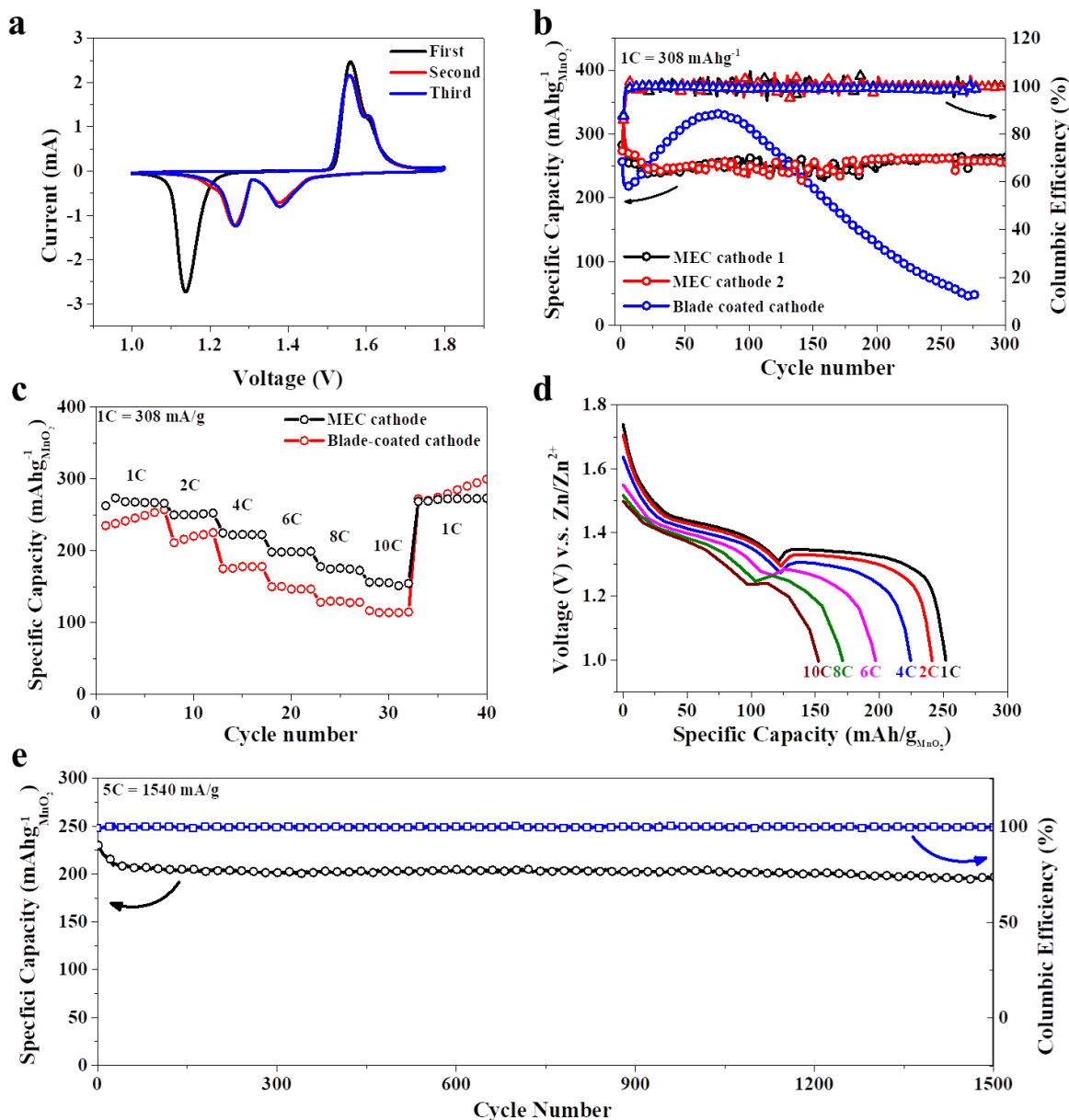


Figure 4.4 a) CV scans, b) 1C Galvanostatic cycling performance, c & d) rate performance, and e) 5C Galvanostatic cycling performance of RMAZM batteries prepared with MEC electrode.

Aside for its much improve stability in low C-rate cycling, the rate performance of the cathode electrode is also improved with the proposed electrode design. As shown in **Figure 4.4c**, the specific capacities of MEC electrode at C-rates of 1C, 2C, 4C, 6C, 8C and 10C are 267 $mAhg^{-1}$, 251 $mAhg^{-1}$, 222 $mAhg^{-1}$, 200 $mAhg^{-1}$, 174 $mAhg^{-1}$ and 152

mAhg^{-1} , outperforming the standard electrode in every C rate, and matching the rate performance of the best performing MnO_2 electrode in recent publications.¹¹⁹ The improvement is most significant in C rates that are equal or above 4C, in which the specific capacities of the MEC electrodes exceed the ones of the standard electrodes by more than 25%. The integrity of the MEC electrodes against high C-rate cycling is also confirmed as the 1C specific capacities return to the original values. **Figure 4.4d** shows the discharge curves of the MEC electrode at different C-rates. Clearly, the 1.3V plateau was influenced more heavily by the increasing C-rate, as it begins to lower and shorten as soon as the C-rate is increased to 2, and continues to decrease through the entire increment process. In contrast, the 1.4V plateau experiences very little change prior to the 6C discharge and lost less than 25% of its capacity going from 1C to 10C. These results suggest different kinetics of the two plateaus, further confirming the presence of two individual reactions in RMAZM batteries.¹¹² Finally, the long term high C-rate cycle stability of the MEC electrode was examined and its performance at 5C is demonstrated in **Figure 4.4e**. The electrode first demonstrated a capacity of $\sim 220 \text{ mAh g}^{-1}$ that stabilized to 205 mAh g^{-1} within the first hundred cycles, which was largely maintained for 1500 cycles; the electrode ended the cycling test with a specific capacity of 197 mAh g^{-1} , recording a capacity loss of less than 4% that are comparable to RMAZM batteries demonstrated in previous publications.^{21,31,119}

Post cycling analyses on the MEC electrodes were conducted to confirm the connections between the high cycling stability and the inhibition of the electrodeposition reaction. **Figure 4.5a** and **4.5b** are SEM images of the electrode surface after long period of cycling; it can be clearly observed that the EG surface is free of electrodeposited MnO_2 nanosheets, while the $\alpha\text{-MnO}_2$ nanorods are broken into smaller and shorter particles that intertwine with CNT and reside between the EG layers. The EG surface observed under SEM (**Figure 4.5c**) after 48 hrs of 1.8V constant voltage hold is also found to be clean and smooth, without any signs of MnO_2 deposits. The MnO_2 electrodeposition did still occur though, but in a much smaller scale on top of the $\alpha\text{-MnO}_2$ nanorods (**Figure 4.5d**) comparing to ones observed on the standard electrode (Figure 3.4). These results confirm that MnO_2 electrodeposition is much less likely to

occur after the implementation of EG, but the phenomenon itself is not completely forbidden given their thermodynamic favourability.

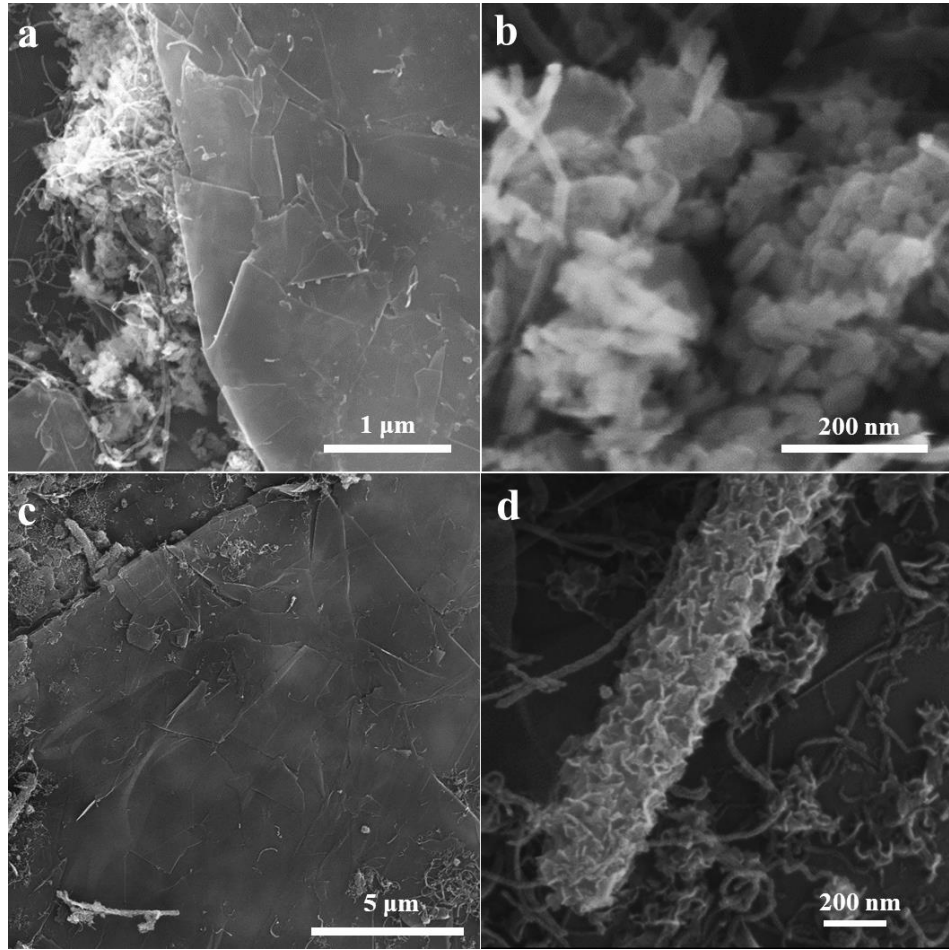


Figure 4.5 a, b) SEM surface image of the MEC electrode after Galvanostatic cycling, c, d) SEM surface image of the MEC electrode after 48hrs of 1.8V constant voltage hold.

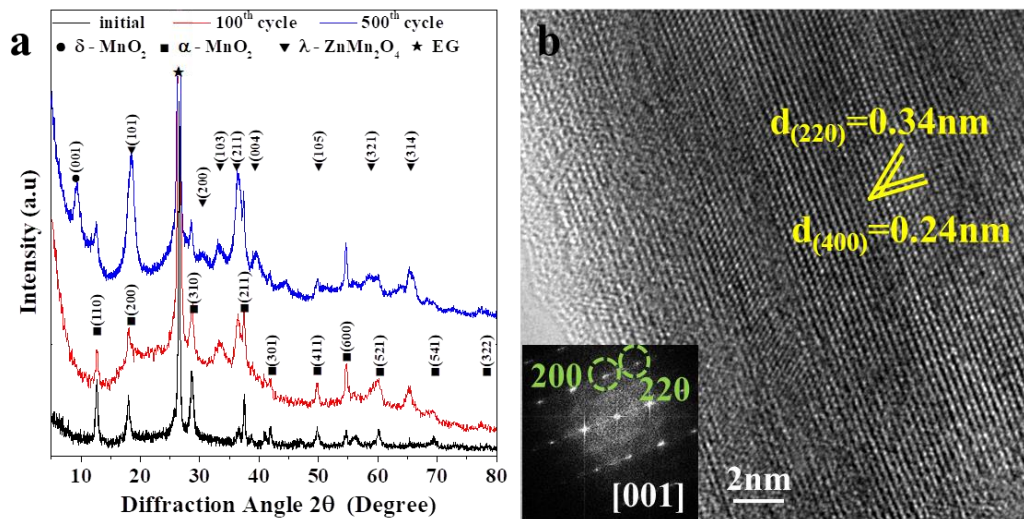


Figure 4.6 a) XRD spectra of the MEC electrodes and b) HRTEM image of the MEC electrode after 500 cycles of Galvanostatic charge and discharge.

XRD analyses of the MEC electrodes at their initial state, 100th cycle and 500th cycle are also compared in **Figure 4.6a**. As shown, the crystal diffractions of the α -MnO₂ are well maintained in the 100th cycle and easily detectable in the 500th cycle, suggesting the preservation of the original crystal phase in the MEC electrodes. In the 100th cycle, diffractions of δ -MnO₂ and ϵ -MnO₂ are nowhere to be found, but some peaks associated with λ -ZnMn₂O₄ are detectable. In the 500th cycles, diffractions of δ -MnO₂ and λ -ZnMn₂O₄ become more prominent, confirming their eventual appearance within the MEC electrode. Though, it has also been observed in the HRTEM image of the α -MnO₂ nanorods in the same MEC electrode that their crystal structure is well maintained (**Figure 4.6b**); the [400] and [220] lattice fringes of α -MnO₂ with d-spacing of 0.24 nm and 0.34 nm are clearly observed and the FFT pattern of this area can be indexed to the [001] zone axis. This ensures that δ -MnO₂ and λ -ZnMn₂O₄ are only converted from the electrodeposited MnO₂ polymorph instead of the original active material.

In this chapter, the adaptation of EG into MnO₂ cathode electrodes is explored as an attempt to inhibit the undesired reactions previously identified to be a battery stability issue. The results were promising as the MEC electrode demonstrated extended low C-rate cycle life and improved rate performance while maintaining the high C-rate stability showcased by previous publications. Though, the electrode design is not perfect and the electrodeposition phenomenon does still occur due to its thermodynamic favourability. Despite so, the end results still validated the approach of extending the Zn-MnO₂ batteries life span through inhibiting MnO₂ electrodeposition and the design strategy established a new path for further optimization and development of the system.

5 Conclusions and Suggestions

In this thesis, the MnO₂ cathode electrodes in the recently emerging mildly acidic Zn-MnO₂ batteries system are thoroughly investigated and new knowledge about the system is developed. Precisely, the in-situ Mn²⁺ electrodeposition phenomenon, short and long term crystal phase transformation mechanism of manganese species were studied and linked to the battery performances. In contrast to previous studies, the investigation results identified MnO₂ electrodeposition as an undesired reaction that opens up a path toward performance degradation, and the new found recognitions were adapted in the formulation of a novel cathode electrode design approach. The resulting EG incorporated polymer-free MnO₂ electrode demonstrated much improved low C-rate stability and rate performance without sacrificing its high C-rate longevity, which therefore further raised the overall performance RMAZM batteries. It is recognized though that the proposed electrode design is not perfect and there are still rooms for growth to further expand the commercial feasibility of the system.

There are still many questions about RMAZM batteries left to be answer that could possibility served as the catalysts to further improve the system performance. For one, understanding the Mn, O and Zn bonding condition within the defected α -MnO₂ crystal phases would be of great interest for targeted element substitution. Amorphous MnO₂, an important part of the system that was not investigated in this thesis due to instrument limitation could be studied with characterization techniques such as X-ray absorption spectroscopy to identify hidden keys for modification. The results obtained from such investigations may lead to strategies that completely forbid the undesirable MnO₂ electrodeposition phenomenon or new Mn based material that undergoes reaction processes that are fundamentally more reversible. Lastly, the electrode design could be further optimized toward higher active material loading or revitalized for incorporation to the cylindrical Zn-MnO₂ batteries.

6 Reference

- (1) Winter, M.; Brodd, R. J. *Chemical Reviews* **2004**, *104*, 4245.
- (2) *World Energy Resources 2016 Executive Summary* World Energy Council 2016.
- (3) Ball, J. Germany's High-Priced Energy Revolution. <http://fortune.com/2017/03/14/germany-renewable-clean-energy-solar/> (accessed April 18 2018).
- (4) Nordensv ärd, J.; Urban, F. *Energy Policy* **2015**, *82*, 156.
- (5) Reed, S. Germany's Shift to Green Power Stalls, Depiste Huge Investment. <https://www.nytimes.com/2017/10/07/business/energy-environment/german-renewable-energy.html> (accessed April 18 2018).
- (6) Quitzow, L.; Canzler, W.; Grundmann, P.; Leibenath, M.; Moss, T.; Rave, T. *Utilities Policy* **2016**, *41*, 163.
- (7) Paul, F. C. *Geoforum* **2018**, *91*, 1.
- (8) Dunn, B.; Kamath, H.; Tarascon, J.-M. *Science* **2011**, *334*, 928.
- (9) Mauger, A.; Julien, C. *Ionics* **2017**, *23*, 1933.
- (10) Lebedeva, N. P.; Boon-Brett, L. *Journal of The Electrochemical Society* **2016**, *163*, A821.
- (11) Nitta, N.; Wu, F.; Lee, J. T.; Yushin, G. *Materials today* **2015**, *18*, 252.
- (12) Hodge, A.; Crowley, B.; Bairstrow, H.; Ljubisavljevic, S.; Hamilton, C.; Morton, P.; Kejrival, D.; May, C.; Diyachikina, P.; South, F.; Thong, D.; Katayama, T.; Park, A.; Shin, S.; Lewis, J.; Lin, Z. Global Lithium Report. <https://newagemetals.com/wp-content/uploads/MacquarieGlobalLithiumReport310516e245188.pdf> (accessed July 2018).
- (13) Kesler, S. E.; Gruber, P. W.; Medina, P. A.; Keoleian, G. A.; Everson, M. P.; Wallington, T. J. *Ore Geology Reviews* **2012**, *48*, 55.
- (14) 5 Year Cobalt Prices and Price Charts. <http://www.infomine.com/investment/metal-prices/cobalt/5-year/> (accessed May 01 2018).
- (15) Jacobs, J. Benchmark: What Drove Lithium Prices in December? <https://www.globalxfunds.com/benchmark-what-drove-lithium-prices-in-december/> (accessed May 1 2018).
- (16) Tisserant, A.; Pauliuk, S. *Journal of Economic Structures* **2016**, *5*, 4.
- (17) Gruber, P. W.; Medina, P. A.; Keoleian, G. A.; Kesler, S. E.; Everson, M. P.; Wallington, T. J. *Journal of Industrial Ecology* **2011**, *15*, 760.
- (18) Hwang, J.-Y.; Myung, S.-T.; Sun, Y.-K. *Chemical Society Reviews* **2017**, *46*, 3529.
- (19) Fu, J.; Cano, Z. P.; Park, M. G.; Yu, A.; Fowler, M.; Chen, Z. *Advanced Materials* **2017**, *29*.
- (20) Cano, Z. P.; Banham, D.; Ye, S.; Hintennach, A.; Lu, J.; Fowler, M.; Chen, Z. *Nature Energy* **2018**, *3*, 279.
- (21) Pan, H.; Shao, Y.; Yan, P.; Cheng, Y.; Han, K. S.; Nie, Z.; Wang, C.; Yang, J.; Li, X.; Bhattacharya, P. *Nature Energy* **2016**, *1*, 16039.

- (22) Parker, J. F.; Chervin, C. N.; Pala, I. R.; Machler, M.; Burz, M. F.; Long, J. W.; Rolison, D. R. *Science* **2017**, *356*, 415.
- (23) Reddy, T. *Linden's Handbook of Batteries, 4th Edition*; McGraw-Hill Education, 2010.
- (24) McLarnon, F. R.; Cairns, E. J. *Journal of the Electrochemical Society* **1991**, *138*, 645.
- (25) Zinc facts. <http://www.nrcan.gc.ca/mining-materials/facts/zinc/20534> (accessed April 26 2018).
- (26) Ebin, B.; Petranikova, M.; Steenari, B.-M.; Ekberg, C. *Waste Management* **2016**, *51*, 157.
- (27) Chen, W.-S.; Liao, C.-T.; Lin, K.-Y.
- (28) Biswas, R. K.; Karmakar, A. K.; Kumar, S. L. *Waste Management* **2016**, *51*, 174.
- (29) Kundu, D.; Adams, B. D.; Duffort, V.; Vajargah, S. H.; Nazar, L. F. *Nat. Energy* **2016**, *1*, 16119.
- (30) Zhao, Q.; Huang, W.; Luo, Z.; Liu, L.; Lu, Y.; Li, Y.; Li, L.; Hu, J.; Ma, H.; Chen, J. *Science Advances* **2018**, *4*.
- (31) Zhang, N.; Cheng, F.; Liu, J.; Wang, L.; Long, X.; Liu, X.; Li, F.; Chen, J. *Nature communications* **2017**, *8*, 405.
- (32) Xu, C.; Li, B.; Du, H.; Kang, F. *Angewandte Chemie International Edition* **2012**, *51*, 933.
- (33) Xiaowei, W.; Faxing, W.; Liying, W.; Minxia, L.; Yanfang, W.; Bingwei, C.; Yusong, Z.; Lijun, F.; Liusheng, Z.; Lixin, Z.; Yuping, W.; Wei, H. *Advanced Materials* **2016**, *28*, 4904.
- (34) Liu, W.; Hao, J.; Xu, C.; Mou, J.; Dong, L.; Jiang, F.; Kang, Z.; Wu, J.; Jiang, B.; Kang, F. *Chemical Communications* **2017**, *53*, 6872.
- (35) Kaveevivitchai, W.; Manthiram, A. *Journal of Materials Chemistry A* **2016**, *4*, 18737.
- (36) Pan, H.; Mengyu, Y.; Guobin, Z.; Ruimin, S.; Lineng, C.; Qinyou, A.; Liqiang, M. *Advanced Energy Materials* **2017**, *7*, 1601920.
- (37) Cheng, Y.; Luo, L.; Zhong, L.; Chen, J.; Li, B.; Wang, W.; Mao, S. X.; Wang, C.; Sprenkle, V. L.; Li, G.; Liu, J. *ACS Applied Materials & Interfaces* **2016**, *8*, 13673.
- (38) Leyuan, Z.; Liang, C.; Xufeng, Z.; Zhaoping, L. *Advanced Energy Materials* **2015**, *5*, 1400930.
- (39) Rafael, T.; Fabio, L. M. *ChemSusChem* **2015**, *8*, 481.
- (40) Gupta, T.; Kim, A.; Phadke, S.; Biswas, S.; Luong, T.; Hertzberg, B. J.; Chamoun, M.; Evans-Lutterodt, K.; Steingart, D. A. *Journal of Power Sources* **2016**, *305*, 22.
- (41) Biswal, A.; Tripathy, B. C.; Sanjay, K.; Subbaiah, T.; Minakshi, M. *RSC Advances* **2015**, *5*, 58255.
- (42) Manganese Statistics and Information. <https://minerals.usgs.gov/minerals/pubs/commodity/manganese/#pubs> (accessed May 20 2018).

- (43) 5 Year Manganese Prices and Price Charts.
<http://www.infomine.com/investment/metal-prices/manganese/5-year/> (accessed May 20 2018).
- (44) Besenhard, J. O. *Handbook of battery materials*; John Wiley & Sons, 2008.
- (45) Bystrom, A. *Acta Chemica Scandinavica* **1949**, 3, 163.
- (46) DeWolff, P.; Visser, J.; Giovanoli, R.; Brutsch, R. *Chimia* **1978**, 32, 257.
- (47) De Wolff, P. *Acta Crystallographica* **1959**, 12, 341.
- (48) Charenton, J. C.; Strobel, P. *Journal of Solid State Chemistry* **1988**, 77, 33.
- (49) Jouanneau, S.; Sarciaux, S.; La Salle, A. L. G.; Guyomard, D. *Solid State Ionics* **2001**, 140, 223.
- (50) Jouanneau, S.; La Salle, A. L. G.; Guyomard, D. *Electrochimica acta* **2002**, 48, 11.
- (51) Thackeray, M. M. *Progress in Solid State Chemistry* **1997**, 25, 1.
- (52) Chabre, Y.; Pannetier, J. *Progress in Solid State Chemistry* **1995**, 23, 1.
- (53) Poyraz, A. S.; Huang, J.; Cheng, S.; Wu, L.; Tong, X.; Zhu, Y.; Marschilok, A. C.; Takeuchi, K. J.; Takeuchi, E. S. *Journal of The Electrochemical Society* **2017**, 164, A1983.
- (54) Poyraz, A. S.; Huang, J.; Pelliccione, C. J.; Tong, X.; Cheng, S.; Wu, L.; Zhu, Y.; Marschilok, A. C.; Takeuchi, K. J.; Takeuchi, E. S. *Journal of Materials Chemistry A* **2017**, 5, 16914.
- (55) Huang, J.; Poyraz, A. S.; Takeuchi, K. J.; Takeuchi, E. S.; Marschilok, A. C. *Chemical communications* **2016**, 52, 4088.
- (56) Tompsett, D. A.; Islam, M. S. *Chemistry of Materials* **2013**, 25, 2515.
- (57) Johnson, C. S. *Journal of Power Sources* **2007**, 165, 559.
- (58) Zhang, C.; Feng, C.; Zhang, P.; Guo, Z.; Chen, Z.; Li, S.; Liu, H. *RSC Advances* **2012**, 2, 1643.
- (59) Huang, J.; Poyraz, A. S.; Lee, S.-Y.; Wu, L.; Zhu, Y.; Marschilok, A. C.; Takeuchi, K. J.; Takeuchi, E. S. *ACS applied materials & interfaces* **2016**, 9, 4333.
- (60) Xu, F.; Wu, L.; Meng, Q.; Kaltak, M.; Huang, J.; Durham, J. L.; Fernandez-Serra, M.; Sun, L.; Marschilok, A. C.; Takeuchi, E. S. *Nature Communications* **2017**, 8, 15400.
- (61) Zhang, R.; Yu, X.; Nam, K.-W.; Ling, C.; Arthur, T. S.; Song, W.; Knapp, A. M.; Ehrlich, S. N.; Yang, X.-Q.; Matsui, M. *Electrochemistry Communications* **2012**, 23, 110.
- (62) Brousse, T.; Toupin, M.; Dugas, R.; Athouël, L.; Crosnier, O.; Bédaride, D. *Journal of the Electrochemical Society* **2006**, 153, A2171.
- (63) Chen, K.; Sun, C.; Xue, D. *Physical Chemistry Chemical Physics* **2015**, 17, 732.
- (64) Ma, Z.; Shao, G.; Fan, Y.; Wang, G.; Song, J.; Shen, D. *ACS applied materials & interfaces* **2016**, 8, 9050.
- (65) Wei, W.; Cui, X.; Chen, W.; Ivey, D. G. *Chemical society reviews* **2011**, 40, 1697.
- (66) Lehtimäki, M.; Hoffmannová, H.; Boytsova, O.; Bastl, Z.; Busch, M.; Halck, N. B.; Rossmeisl, J.; Krtil, P. *Electrochimica Acta* **2016**, 191, 452.
- (67) Lee, J.; Ju, J. B.; Cho, W. I.; Cho, B. W.; Oh, S. H. *Electrochimica Acta* **2013**, 112, 138.

- (68) Post, J. E.; Veblen, D. R. *American Mineralogist* **1990**, *75*, 477.
- (69) Alfaruqi, M. H.; Gim, J.; Kim, S.; Song, J.; Pham, D. T.; Jo, J.; Xiu, Z.; Mathew, V.; Kim, J. *Electrochemistry Communications* **2015**, *60*, 121.
- (70) Kim, S. H.; Kim, S. J.; Oh, S. M. *Chemistry of Materials* **1999**, *11*, 557.
- (71) Thapa, A. K.; Pandit, B.; Thapa, R.; Luitel, T.; Paudel, H. S.; Sumanasekera, G.; Sunkara, M. K.; Gunawardhana, N.; Ishihara, T.; Yoshio, M. *Electrochimica Acta* **2014**, *116*, 188.
- (72) Zhao, J.; Xu, L.; Xie, C. *Chinese Journal of Geochemistry* **2013**, *32*, 380.
- (73) Jiangang, F.; Zhangxing, H.; Hui, W.; LIANG, W.; Chao, G. *Mining Science and Technology (China)* **2010**, *20*, 877.
- (74) Musil, M.; Choi, B.; Tsutsumi, A. *Journal of The Electrochemical Society* **2015**, *162*, A2058.
- (75) Marsal, P. A.; Karl, K.; Urry, L. F.; Google Patents: 1960.
- (76) Dirkse, T.; Vander Lugt, L.; Hampson, N. *Journal of The Electrochemical Society* **1971**, *118*, 1606.
- (77) Johansen, J. F., Queensland University of Technology, 2007.
- (78) Cahoon, N.; Korver, M. *Journal of The Electrochemical Society* **1959**, *106*, 745.
- (79) Bell, G.; Huber, R. *Journal of The Electrochemical Society* **1964**, *111*, 1.
- (80) Kozawa, A.; Powers, R. *Journal of The Electrochemical Society* **1966**, *113*, 870.
- (81) Technical Bulletins - Alkaline-Manganese Dioxide Batteries. <https://www.duracell.com/en-ca/techlibrary/technical-bulletins> (accessed May 05 2018).
- (82) Division, U. C. C. C. P. "Eveready" battery applications and engineering data; Unitech Division, Associated Educational Services Corp., 1968.
- (83) Xia, X.; Li, H.; Chen, Z. H. *Journal of The Electrochemical Society* **1989**, *136*, 266.
- (84) Baugh, L.; Cook, J.; Lee, J. *Journal of Applied Electrochemistry* **1978**, *8*, 253.
- (85) Agency, U. S. E. P., Ed.; 104th U.S. Congress: 1996.
- (86) Yoshizawa, H.; Miura, A.; Nitta, Y.; Sugihara, S.; Google Patents: 1992.
- (87) Kato, F.; Nunome, J.; Shimamura, H.; Google Patents: 2010.
- (88) Kordesch, K.; Gsellmann, J.; Tomantschger, K.; Google Patents: 1991.
- (89) Josef Daniel-Ivad; Karl Kordesch. Rechargeable Alkaline Manganese Technology: Past-Present-Future <https://www.electrochem.org/dl/ma/201/pdfs/0257.pdf> (accessed May 17 2018).
- (90) Ingale, N. D.; Gallaway, J. W.; Nyce, M.; Couzis, A.; Banerjee, S. *Journal of Power Sources* **2015**, *276*, 7.
- (91) Mondoloni, C.; Laborde, M.; Rioux, J.; Andoni, E.; Lévy - Clément, C. *Journal of The Electrochemical Society* **1992**, *139*, 954.
- (92) Kannan, A.; Bhavaraju, S.; Prado, F.; Raja, M. M.; Manthiram, A. *Journal of The Electrochemical Society* **2002**, *149*, A483.
- (93) Gallaway, J. W.; Hertzberg, B. J.; Zhong, Z.; Croft, M.; Turney, D. E.; Yadav, G. G.; Steingart, D. A.; Erdonmez, C. K.; Banerjee, S. *Journal of Power Sources* **2016**, *321*, 135.

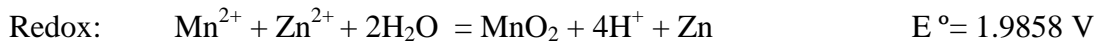
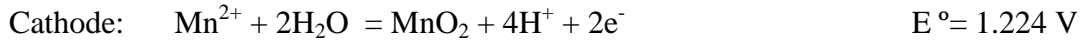
- (94) Hertzberg, B. J.; Huang, A.; Hsieh, A.; Chamoun, M.; Davies, G.; Seo, J. K.; Zhong, Z.; Croft, M.; Erdonmez, C.; Meng, Y. S. *Chemistry of Materials* **2016**, *28*, 4536.
- (95) Nartey, V. K.; Binder, L.; Huber, A. *Journal of Power Sources* **2000**, *87*, 205.
- (96) Li, X.; Li, Z.; Xia, T.; Dong, H.; Song, Y.; Wang, L. *Journal of Physics and Chemistry of Solids* **2012**, *73*, 1229.
- (97) Im, D.; Manthiram, A.; Coffey, B. *Journal of The Electrochemical Society* **2003**, *150*, A1651.
- (98) Yadav, G. G.; Gallaway, J. W.; Turney, D. E.; Nyce, M.; Huang, J.; Wei, X.; Banerjee, S. *Nature Communications* **2017**, *8*, 14424.
- (99) Sun, K. E.; Hoang, T. K.; Doan, T. N. L.; Yu, Y.; Zhu, X.; Tian, Y.; Chen, P. *ACS applied materials & interfaces* **2017**, *9*, 9681.
- (100) Turney, D. E.; Gallaway, J. W.; Yadav, G. G.; Ramirez, R.; Nyce, M.; Banerjee, S.; Chen-Wiegart, Y.-c. K.; Wang, J.; D'Ambrose, M. J.; Kolhekar, S. *Chemistry of Materials* **2017**, *29*, 4819.
- (101) Zhou, H.; Huang, Q.; Liang, M.; Lv, D.; Xu, M.; Li, H.; Li, W. *Materials chemistry and Physics* **2011**, *128*, 214.
- (102) Shoji, T.; Hishinuma, M.; Yamamoto, T. *Journal of applied electrochemistry* **1988**, *18*, 521.
- (103) Shoji, T.; Yamamoto, T. *Journal of Electroanalytical Chemistry* **1993**, *362*, 153.
- (104) Askar, M.; Abbas, H.; Afifi, S. *Journal of power sources* **1994**, *48*, 303.
- (105) Hoang, T. K.; Sun, K. E. K.; Chen, P. *RSC Advances* **2015**, *5*, 41677.
- (106) Boytsova, O.; Shekunova, T.; Baranchikov, A. *Nanocrystalline Manganese Dioxide Synthesis by Microwave-Hydrothermal Treatment*, 2015; Vol. 60.
- (107) Al-Hinai, A. T.; Al-Hinai, M. H.; Dutta, J. *Materials Research Bulletin* **2014**, *49*, 645.
- (108) Wu, X.; Xiang, Y.; Peng, Q.; Wu, X.; Li, Y.; Tang, F.; Song, R.; Liu, Z.; He, Z.; Wu, X. *Journal of Materials Chemistry A* **2017**, *5*, 17990.
- (109) Zhang, N.; Cheng, F.; Liu, Y.; Zhao, Q.; Lei, K.; Chen, C.; Liu, X.; Chen, J. *Journal of the American Chemical Society* **2016**, *138*, 12894.
- (110) Alfaruqi, M. H.; Islam, S.; Putro, D. Y.; Mathew, V.; Kim, S.; Jo, J.; Kim, S.; Sun, Y.-K.; Kim, K.; Kim, J. *Electrochimica Acta* **2018**, *276*, 1.
- (111) Lee, B.; Lee, H. R.; Kim, H.; Chung, K. Y.; Cho, B. W.; Oh, S. H. *Chemical communications* **2015**, *51*, 9265.
- (112) Sun, W.; Wang, F.; Hou, S.; Yang, C.; Fan, X.; Ma, Z.; Gao, T.; Han, F.; Hu, R.; Zhu, M. *Journal of the American Chemical Society* **2017**, *139*, 9775.
- (113) Lee, B.; Yoon, C. S.; Lee, H. R.; Chung, K. Y.; Cho, B. W.; Oh, S. H. *Scientific reports* **2014**, *4*, 6066.
- (114) Kobayashi, S.; Kottegoda, I. R.; Uchimoto, Y.; Wakihara, M. *Journal of Materials Chemistry* **2004**, *14*, 1843.
- (115) Thackeray, M. M.; Shao - Horn, Y.; Kahaian, A. J.; Kepler, K. D.; Skinner, E.; Vaughey, J. T.; Hackney, S. A. *Electrochemical and Solid-State Letters* **1998**, *1*, 7.
- (116) Benedek, R. *The Journal of Physical Chemistry C* **2017**, *121*, 22049.

- (117) Kim, S. H.; Oh, S. M. *Journal of power sources* **1998**, 72, 150.
- (118) Li, H.; Han, C.; Huang, Y.; Huang, Y.; Zhu, M.; Pei, Z.; Xue, Q.; Wang, Z.; Liu, Z.; Tang, Z. *Energy & Environmental Science* **2018**.
- (119) Wu, B.; Zhang, G.; Yan, M.; Xiong, T.; He, P.; He, L.; Xu, X.; Mai, L. *Small* **2018**, 14, 1703850.
- (120) Gao, T.; Glerup, M.; Krumeich, F.; Nesper, R.; Fjellvåg, H.; Norby, P. *The Journal of Physical Chemistry C* **2008**, 112, 13134.
- (121) Gao, T.; Fjellvåg, H.; Norby, P. *Analytica chimica acta* **2009**, 648, 235.
- (122) Ilton, E. S.; Post, J. E.; Heaney, P. J.; Ling, F. T.; Kerisit, S. N. *Applied Surface Science* **2016**, 366, 475.
- (123) Manganese-Transition Metal.
<https://xpssimplified.com/elements/manganese.php> (accessed Sept 09 2018).
- (124) Lee, B.; Yoon, C. S.; Lee, H. R.; Chung, K. Y.; Cho, B. W.; Oh, S. H. *Scientific reports* **2014**, 4.
- (125) Alfaruqi, M. H.; Mathew, V.; Gim, J.; Kim, S.; Song, J.; Baboo, J. P.; Choi, S. H.; Kim, J. *Chemistry of Materials* **2015**, 27, 3609.
- (126) Cai, M.; Thorpe, D.; Adamson, D. H.; Schniepp, H. C. *Journal of Materials Chemistry* **2012**, 22, 24992.
- (127) Chung, D. *Journal of materials science* **2016**, 51, 554.
- (128) SIGRAFLEX® Expanded Natural Graphite.
http://www.sglgroup.com/cms/international/company/business-units/graphite-materials-and-systems/expanded-graphite/index.html?_locale=en (accessed Sept 18 2018).

7 Appendix

7.1 Appendix A: Calculation of Manganese Ion Oxidation Potential

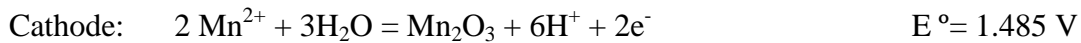
A:



$$E = E^\circ - \frac{RT}{nF} \times \ln \frac{[\text{Zn}^{2+}][\text{Mn}^{2+}]}{[\text{H}_3\text{O}^+]^4}$$

$$E = 1.9858 - \frac{8.314 \times 298}{2 \times 96500} \times \ln \frac{2 \times 0.1}{0.0001^4} = 1.534 \text{ V}$$

B:



$$E = E^\circ - \frac{RT}{nF} \times \ln \frac{[\text{Zn}^{2+}][\text{Mn}^{2+}]}{[\text{H}_3\text{O}^+]^4}$$

$$E = 2.2468 - \frac{8.314 \times 298}{2 \times 96500} \times \ln \frac{2 \times 0.1}{0.0001^6} = 1.558 \text{ V}$$